

Copyright Warning & Restrictions

The copyright law of the United States (Title 17, United States Code) governs the making of photocopies or other reproductions of copyrighted material.

Under certain conditions specified in the law, libraries and archives are authorized to furnish a photocopy or other reproduction. One of these specified conditions is that the photocopy or reproduction is not to be “used for any purpose other than private study, scholarship, or research.” If a user makes a request for, or later uses, a photocopy or reproduction for purposes in excess of “fair use” that user may be liable for copyright infringement,

This institution reserves the right to refuse to accept a copying order if, in its judgment, fulfillment of the order would involve violation of copyright law.

Please Note: The author retains the copyright while the New Jersey Institute of Technology reserves the right to distribute this thesis or dissertation

Printing note: If you do not wish to print this page, then select “Pages from: first page # to: last page #” on the print dialog screen

The Van Houten library has removed some of the personal information and all signatures from the approval page and biographical sketches of theses and dissertations in order to protect the identity of NJIT graduates and faculty.

ABSTRACT

HYDRODYNAMIC INVESTIGATION OF THE DISCHARGE OF COMPLEX FLUIDS FROM DISPENSING BOTTLES USING EXPERIMENTAL AND COMPUTATIONAL APPROACHES

by
Baran Teoman

The discharge of non-Newtonian, complex fluids through orifices of industrial tanks, pipes, dispensers, or packaging containers is a ubiquitous but often problematic process because of the complex rheology of such fluids and the geometry of the containers. This, in turn, reduces the discharge rate and results in residual fluid left in the container, often referred to as heel. Heel formation is undesired in general, since it causes loss of valuable material, container fouling, and cross-contamination between batches. Heel may be of significant concern not only in industrial vessels but also in consumer packaging. Despite its relevance, the research in this area is significantly limited.

Previous research conducted in simpler systems, such as orifices of pipes and vessels, has already shown that the discharge of fluids through orifices is significantly affected by the geometric parameters and the fluid rheology. More specifically, the geometric properties of the orifice such as the diameter ratio, aspect ratio, and orifice shape, and the rheological properties of the fluid played a critical role on the discharge of complex fluids through orifices of vessels and pipes. However, how these parameters affect the discharge of complex fluids flow from more complicated systems such as consumer dispensing bottles operating with a hand pump has remained uninvestigated.

Therefore, the overall objectives of this work are to quantify the discharge hydrodynamics in dispensing bottles and the resulting heel for a wide range of geometries, operational parameters, and fluid rheology through the use of experimental and

computational approaches. Particle Image Velocimetry (PIV) is the main experimental tool used in this work. A novel experimental methodology is also developed and utilized to optimize the transparency of the highly complex fluids such as pastes, for their optical hydrodynamic investigations using PIV. In addition, Computational Fluid Dynamics (CFD) is also utilized to predict the hydrodynamics and the residual heel volume. The simulation predictions are validated against the experimental data.

It is found that the heel volume and profile after the discharge is strongly related to the flow during the discharge, and both static and dynamic aspects of the discharge process can be determined using PIV, and predicted using CFD. Finally, correlations to predict the heel volume based on the rheological and geometric parameters are presented. It is expected that this work will be of significant academic and industrial interest, especially for product developers and packaging engineers to optimize the shape of dispensing bottles so that the discharge process from such containers is facilitated, and the heel volume is minimized.

**HYDRODYNAMIC INVESTIGATION OF THE DISCHARGE OF COMPLEX
FLUIDS FROM DISPENSING BOTTLES USING EXPERIMENTAL AND
COMPUTATIONAL APPROACHES**

**by
Baran Teoman**

**A Dissertation
Submitted to the Faculty of
New Jersey Institute of Technology
in Partial Fulfillment of the Requirements for the Degree of
Doctor of Philosophy in Chemical Engineering**

**Otto H. York Department of
Chemical and Materials Engineering**

December 2022

Copyright © 2022 by Baran Teoman

ALL RIGHTS RESERVED

APPROVAL PAGE

**HYDRODYNAMIC INVESTIGATION OF THE DISCHARGE OF COMPLEX
FLUIDS FROM DISPENSING BOTTLES USING EXPERIMENTAL AND
COMPUTATIONAL APPROACHES**

Baran Teoman

Dr. Piero M. Armenante, Dissertation Advisor Date
Distinguished Professor of Chemical and Materials Engineering, NJIT

Dr. Ecevit Bilgili, Committee Member Date
Professor of Chemical and Materials Engineering, NJIT

Dr. Murat Guvendiren, Committee Member Date
Associate Professor of Chemical and Materials Engineering, NJIT

Dr. Roman S. Voronov, Committee Member Date
Assistant Professor of Chemical and Materials Engineering, NJIT

Dr. Andrei Potanin, Committee Member Date
Associate Director, Colgate-Palmolive, Piscataway, NJ

BIOGRAPHICAL SKETCH

Author: Baran Teoman
Degree: Doctor of Philosophy
Date: December 2022

Undergraduate and Graduate Education:

- Doctor of Philosophy in Chemical Engineering
New Jersey Institute of Technology, Newark, NJ, 2022
- Master of Science in Pharmaceutical Engineering
New Jersey Institute of Technology, Newark, NJ, 2019
- Bachelor of Science in Chemical Engineering
Yeditepe University, Istanbul, Turkey, 2018

Major: Chemical Engineering

Presentations and Publications:

Peer-reviewed Journals:

- B. Teoman, A. Potanin, P.M. Armenante, *Optimization of optical transparency of personal care products using the refractive index matching method*, Colloids and Surfaces A: Physicochemical and Engineering Aspects 610 (2021) 125595.
- B. Teoman, S. Shastry, S. Abdelhamid, P.M. Armenante, *Imaging method for the determination of the minimum agitation speed, N_{js} , for solids suspension in stirred vessels and reactors*, Chemical Engineering Science 231 (2021) 116263.
- B. Teoman, C. Sirasitthichoke, A. Potanin, P.M. Armenante, *Determination of the just-suspended speed, N_{js} , in stirred tanks using electrical resistance tomography (ERT)*, American Institute of Chemical Engineers (AIChE) Journal 67 (10) (2021) e17354.
- B. Teoman, G. Marron, A. Potanin, *Rheological characterization of flow inception of thixotropic yield stress fluids using vane and T-bar geometries*, Rheologica Acta 60 (9) (2021) 531-542.

- B. Teoman, Z. Muneeswaran, G. Verma, D. Chen, T.V. Brinzari, A. Almeda-Ahmadi, J. Norambuena, S. Xu, S. Ma, J.M. Boyd, P.M. Armenante, A. Potanin, L. Pan, T. Asefa, V. Dubovoy, *Cetylpyridinium Trichlorostannate: Synthesis, antimicrobial properties, and controlled-release properties via electrical resistance tomography*, American Chemical Society (ACS) Omega 6 (51) (2021) 35433-35441.
- C. Sirasitthichoke, B. Teoman, J. Thomas, P.M. Armenante, *Computational prediction of the just-suspended speed, N_{js} , in stirred vessels using the Lattice Boltzmann method (LBM)*, Chemical Engineering Science 251 (2022) 117411.
- B. Teoman, A. Potanin, P.M. Armenante, *The discharge of complex fluids through an orifice: A review*, Chemical Engineering Research and Design 179 (2022) 346-364.
- B. Teoman, A. Potanin, P.M. Armenante, *Residual heel volume during the pressure-driven discharge of complex fluids from consumer dispensing bottles*, Journal of Non-Newtonian Fluid Mechanics, 309 (2022) 104917.
- B. Teoman, A. Potanin, P.M. Armenante, *Effect of rheology and operational parameters on the discharge hydrodynamics of consumer dispensing bottles*, Journal of Non-Newtonian Fluid Mechanics (*submitted*).
- B. Teoman, A. Potanin, P.M. Armenante, *Effect of orifice shape and the dip tube clearance on discharge hydrodynamics and residual heel volume in a dispensing bottle*, Chemical Engineering Research and Design (*submitted*).

Conference Paper:

- B. Teoman, C. Sirasitthichoke, A. Potanin, P.M. Armenante, *Determination of the Just-Suspended Speed, N_{js} , in Stirred Tanks Using Electrical Resistance Tomography (ERT)*, North American Mixing Forum (NAMF) (Part of American Institute of Chemical Engineers (AIChE) Annual Meeting), June 2022.

Conference Presentations:

- B. Teoman, C. Sirasitthichoke, A. Potanin, P.M. Armenante, *Determination of the Just-Suspended Speed, N_{js} , in Stirred Tanks Using Electrical Resistance Tomography (ERT)*, Presented at North American Mixing Forum (NAMF) (Part of American Institute of Chemical Engineers (AIChE) Annual Meeting) Mixing XXVII, June 2022.
- B. Teoman, C. Sirasitthichoke, A. Potanin, P.M. Armenante, *Application of electrical resistance tomography (ERT) to solid-liquid mixtures in stirred vessels for the determination of the just-suspended speed, N_{js}* . Presented at American Institute of Chemical Engineers (AIChE) Annual Meeting, Boston, MA, November 2021.

B. Teoman, P.M. Armenante, *A novel approach to the experimental determination of N_{js} using electrical resistance tomography*. Presented at American Institute of Chemical Engineers (AIChE) Annual Meeting, Orlando, FL, November 2019.

To my family:

Seyhan Teoman (Father), Yeşim Teoman (Mother), and Derin Teoman (Sister)
Thank you for your unconditional love and always support on this journey.

“And those who were seen dancing were thought to be insane
by those who could not hear the music.”

Friedrich Nietzsche

ACKNOWLEDGMENT

I have always been told that pursuing a Ph.D. degree in engineering while working in industry would be quite tough and that for some people it would be impossible. While I have always liked to challenge myself, I have to admit that this was the biggest challenge I have faced thus far, not to mention the financial and personal issues that came with it.

Firstly, I would like to thank my grandfather, Şenol Sezel, who was my sponsor during my master's studies at NJIT, for which he and my grandmother, Nezahat Sezel, had to make many compromises. My grandfather is the main reason I was able to obtain a master's degree, and continue for a Ph.D. degree. Secondly, I want to thank deeply my family members, Seyhan Teoman (father), Yeşim Teoman (mother), and Derin Teoman (sister) for their unconditional love, support, and patience for me. My father, especially, has played a critical role in my Ph.D. life, as I was close to giving up on my Ph.D. a couple of times, especially during the coronavirus pandemic, but he gave me the strength to continue my Ph.D.

I would like to express my heartiest gratitude and thank my research advisor, Dr. Piero M. Armenante. I worked in his lab for about 5 years, and I matured as a leader and as an engineer. I have learned many valuable skills and lessons from him, such as scientific and writing skills, that I will carry throughout my life. He is the one who admitted me to the master's program and opened the doors of an extensive industrial experience at Colgate-Palmolive while pursuing a Ph.D. degree in his lab. He spent quite a lot of time and effort for this to happen, I am truly grateful for everything he has done for me so far.

I would like to acknowledge Dr. Ecevit Bilgili, Dr. Murat Guvendiren, Dr. Roman S. Voronov and Dr. Andrei Potanin for participating in my research as members

of the dissertation committee and giving me advices to increase the value of my research.

There are no words that can express my gratitude to Colgate-Palmolive Company for providing funding for this research, and, especially for my supervisor, Dr. Andrei Potanin with whom I worked for more than three years. Dr. Potanin is my true idol as he is the one who significantly shaped me to be the researcher who I am now during these three years, not only with his extensive knowledge in science, but also by teaching me how to think differently than other people that led the way for this work to happen. I will always be grateful to him.

I also want to thank Dr. Long Pan, the director of our Cross Category Research & Innovation team at Colgate-Palmolive, for being a mentor for me during all this time, supporting my research, and always creating opportunities for me to grow in my career. Special thanks to the members of our team, Dr. Jonghun Lee, Dr. Kristina Fabijanic, Dr. Hongwei Shen, Dr. Zhigang Hao, Dr. Shijian Wu, and Gregory Marron, for their continuous support and appreciation of my academic and industrial efforts.

I want to thank my close friends, Alp Gulel, Mert Iz, and Ella Ivanova, for being with me during all this time, and for their continuous emotional support. It was also a great pleasure working with my colleagues at NJIT, Dr. Chadakarn Sirasitthichoke, Sara Abdelhamid, and Justin Pace. I appreciate their suggestions and assistance with my research. They are all incredible people and made my life more enjoyable when we spend time together in the lab. Without the unlimited support from all these incredible people, this work would not be possible.

TABLE OF CONTENTS

Chapter	Page
1 INTRODUCTION	1
1.1 Background and Significance	1
1.1.1 Factors Affecting the Discharge of Complex Fluids through Orifices ..	7
1.1.2 Rheological Characterization of Complex Fluids	11
1.1.3 Experimental and Computational Tools Used for Flow Monitoring	13
1.2 Overall Research Objectives of This Dissertation Work	16
1.3 Organization of the Dissertation	18
2 IMPROVING THE OPTICAL CHARACTERISTICS OF HIGHLY COMPLEX FLUIDS FOR OPTICAL INVESTIGATIONS USING THE REFRACTIVE INDEX MATCHING METHOD	20
2.1 Abstract	20
2.2 Introduction	21
2.3 Experimental Equipment, Materials, and Methods	23
2.3.1 Equipment	23
2.3.2 Materials	26
2.3.3 Methods	30
2.4 Results	31
2.4.1 Results of Refractive Index Matching Experiments	31
2.4.2 Results of Visual Inspection of Formulations	39
2.5 Discussion	40
2.6 Conclusions	42

TABLE OF CONTENTS
(Continued)

Chapter	Page
3 RESIDUAL HEEL VOLUME DURING THE PRESSURE-DRIVEN DISCHARGE OF COMPLEX FLUIDS FROM DISPENSING BOTTLES	43
3.1 Abstract	43
3.2 Introduction	44
3.3 Experimental Equipment, Materials, and Methods	46
3.3.1 Experimental Equipment	46
3.3.2 Materials	51
3.3.3 Methods	54
3.4 Results	66
3.5 Discussion	73
3.6 Conclusions	78
4 EFFECT OF RHEOLOGY AND OPERATIONAL PARAMETERS ON THE DISCHARGE HYDRODYNAMICS OF CONSUMER DISPENSING BOTTLES	79
4.1 Abstract	79
4.2 Introduction	80
4.3 Experimental Equipment, Materials, and Methods	83
4.3.1 Experimental Equipment	83
4.3.2 Materials	86
4.3.3 Methods	87
4.4 Results	94
4.4.1 Effect of Fluid Rheology on the Discharge Process and Heel Volume	94

TABLE OF CONTENTS
(Continued)

Chapter	Page
4.4.2 Effect of Tube Diameter Ratio (d/D) at Constant Suction Pressure (ΔP) on the Discharge and Heel Volume	100
4.4.3 Effect of Suction Pressure (ΔP) at Constant Tube Diameter Ratio (d/D) on the Discharge and Heel Volume	104
4.4 Overall Correlations for ROI and ΔV_H	107
4.5 Heel Prediction from PIV Experiments and Rheological Data	108
4.6 Computational Results and Comparison with PIV	111
4.7 Discussion	114
4.8 Conclusions	119
5 EFFECT OF DIP TUBE ORIFICE SHAPE AND CLEARANCE ON DISCHARGE HYDRODYNAMICS AND RESIDUAL HEEL VOLUME IN DISPENSING BOTTLES USING PIV.....	120
5.1 Abstract	120
5.2 Introduction	121
5.3 Experimental Equipment, Materials, and Methods	123
5.3.1 Experimental Equipment	123
5.3.2 Materials	124
5.3.3 Methods	124
5.4 Results and Discussion	127
5.5 Conclusions	134
6 OVERALL CONCLUSIONS	135
REFERENCES	140

LIST OF TABLES

Table	Page
2.1 Compositions of the Gels Used in This Work	29
2.2 Composition of the Formulations Used in This Work	29
2.3 The Effective Refractive Index of Silica Particles	42
3.1 Composition of the Fluids Experimentally and Computationally Studied in This Work	53
3.2 Average Velocities on the Horizontal Cross-section 10 mm Above the Orifice of the Tube, as Determined with PIV	58
3.3 Rheological Parameters for the Humectants, Gels and Pastes Experimentally and Computationally Studied in This Work	68
3.4 Rheological Parameters for the Imaginary Model Fluids Computationally Studied in This Work	68
4.1 Composition of the Fluids Studied in This Work	87
4.2 Rheological Parameters of the Complex Fluids Studied in This Work	88
4.3 Operational Parameters	109
4.4 Prob-t Values for the Effects in Equation (4.5)	111

LIST OF FIGURES

Figure	Page
1.1 Examples of complex fluids: paint (left panel) and toothpaste (right panel).	2
1.2 Shear stress-shear rate dependence for common fluids in a simple shear.	3
1.3 Examples of most common commercial complex fluids in various packaging: (a) bottles of different geometries with hand pumps for hand sanitizers, dishwashing liquids, lotions, and gels; (b) a squeezable tube having toothpaste product.	4
1.4 Diagram showing the increased complexity of the fluids frequently used in the oral care product industry.	6
1.5 Conceptual framework of the research.	17
2.1 Whip Mix WPM2 Mixer.	24
2.2 Portable equipment used in this work: (a) Sper Scientific Laboratory 300033 refractometer and (b) Hach-2100Q turbidimeter.	25
2.3 Light transmittance analysis technique used in this work: (a) Turbiscan™ LAB stability analyzer and (b) illustration showing the transmission and backscattering of light for the cases of diluted (or the cases in which the refractive index of the particles are identical to the liquid) and concentrated (or the cases in which the refractive index of the particles are different from that of the liquid) solutions, respectively.	25
2.4 Microphotographs of the silica particles dispersed in water/glycerin mixture at 0.03 wt. %: (a) Silica 1; (b) Silica 3.	28
2.5 Number distribution of the Silica 1 and Silica 3 particles.	28
2.6 Transmittance (top panel) and turbidity (bottom panel) of <i>Formulation 1</i> as a function of the humectant fraction in the corresponding gel (<i>Gel 1</i>).	33
2.7 Transmittance (top panel) and turbidity (bottom panel) of <i>Formulation 1</i> as a function of the refractive index of different versions of the corresponding gel (<i>Gel 1</i>) for different humectant fractions.	34

LIST OF FIGURES
(Continued)

Figure	Page
2.8 Transmittance (top panel) and turbidity (bottom panel) of <i>Formulation 2</i> as a function of the humectant fraction in the corresponding gel (<i>Gel 2</i>).	35
2.9 Transmittance (top panel) and turbidity (bottom panel) of <i>Formulation 2</i> as a function of the refractive index of different versions of the corresponding gel (<i>Gel 2</i>) for different humectant fractions.	36
2.10 Transmittance (top panel) and turbidity (bottom panel) of <i>Formulation 3</i> as a function of the humectant (glycerin) fraction in their corresponding gel (<i>Gel 2</i>).	37
2.11 Transmittance (top panel) and turbidity (bottom panel) of <i>Formulation 3</i> as a function of the refractive index of different versions of their corresponding gel (<i>Gel 2</i>) with different humectant (glycerin) fractions.	38
2.12 Visual results for <i>Formulation 2</i> with different glycerin fractions: (a) Vials with glycerin fractions equal to 79.8%, 74.9%, and 69.2%, from left to right, respectively; (b) lines of text onto which the same formulations were applied, from top to bottom, respectively.	39
3.1 Rheological apparatuses used in this work: (a) DHR-3 rheometer (TA instruments, Delaware, USA); (b) vane-in-cup geometry; (c) concentric cylinder (DIN) geometry.	48
3.2 PIV experimental system.	49
3.3 Diagram of PIV experimental system.	49
3.4 Typical commercial lotion bottle: (a) original bottle with hand pump; (b) bottle actually used in this work with the modified hand pump mechanism removed for continuous discharging of its content.	51
3.5 Typical PIV output: Velocity distributions for 0.5 Xan while being sucked out from the bottle. The white line shows the horizontal plane 10 mm above the orifice, as described in the text.	58
3.6 CFD geometry and mesh showing both computational zones (shown in green color): (a) “dip tube” zone; (b) “bottle” zone.	60

LIST OF FIGURES
(Continued)

Figure	Page
3.7 Dependence of the computationally predicted heel volume in the “bottle” zone on the air fraction in the “dip tube” zone for rheologically different fluids. Connecting lines were added to visualize the trends.	62
3.8 The three steps used in the experimental imaging method: (a) Image of the bottom of the bottle taken by a phone camera; (b) Raw image of the right-hand size of the bottle bottom obtained with the PIV camera after the discharge was completed; (c) Background subtracted-PIV image, as processed by ImageJ, used here to quantify the heel volume as described in the text.	65
3.9 Experimental flow curves (symbols) and the curves fitted using the Carreau equation (lines). The former is a combination of three tests performed with various tools (vane-in-cup and DIN) as described in the text: low-shear creep tests (filled diamonds), low-shear rate sweeps (empty squares), and high-shear rate sweeps (filled squares).	67
3.10 Flow curves for the eight additional imaginary “model” fluids used to verify correlations between CFD calculations of the heel to the rheological parameters. Two curves of the fluids tested experimentally from Figure 3.9 are also shown for comparison.	69
3.11 Heel volume profiles obtained by PIV (left panels; shown in grayscale, where the darker gray color corresponds to the liquid phase) and CFD (right panels; shown in yellow and red colors, corresponding to the air and liquid phases, respectively). Only the right-hand side of the bottle (red insert in Figure 3.8a) is shown in the panels.	71
3.12 Shear rate contour plots in the bottle zone for selected complex fluids during their discharge at $t=5$ s: (a) 0.5 Xan; (b) 1.5 Xan; (c) 16 Silica Paste.	72
3.13 Overall comparison of $V_{H-Weight}$, V_{H-PIV} , and V_{H-CFD} for all the fluids studied in this work. Error bars represent 95% confidence intervals, obtained by three repetitions of each experiment.	72
3.14 Dependence of reduced heel volume ΔV_H on the rheological parameters of the fluids: (a) effective yield stress, σ_0 ; (b) low shear viscosity limit, η_0	76
3.15 Parity plot of the ΔV_H values predicted with Equation (3.6) ($\Delta V_{H-Predicted}$) vs. those obtained through CFD simulations (ΔV_{H-CFD}).	77

LIST OF FIGURES
(Continued)

Figure	Page
4.1 Diagram of the experimental system (not drawn to scale) including the PIV system.	84
4.2 Commercial dispensing bottle: (a) original dispenser; (b) modified dispenser. .	86
4.3 Rheology curves of the complex fluids studied in this work.	89
4.4 PIV analysis: (a) picture of the bottom of the bottle up to a 20 mm height showing the region analyzed here (dashed black lines) and the radial plane on the bottom (equal to the internal diameter of the bottle, shown as a white arrow) on which the ROI analysis was made; (b) example of an experimental velocity contour map as described in the text, and the region on the bottom (shown as black arrows) that is significantly affected by the flow.	90
4.5 Velocity magnitude contour maps for the discharge of the Newtonian fluids studied in this work ($\Delta P = -0.14$ bar, $C = 1.75$ mm, $d/D = 0.119$): (a) water; (b) sorbitol; (c) glycerin.	95
4.6 Velocity magnitude contour maps for the discharge of non-Newtonian fluids studied in this work ($\Delta P = -0.14$ bar, $C = 1.75$ mm, $d/D = 0.119$): (a) 1.0 Xan; (b) 1.5 Xan; (c) 2.5 Xan; (d) 8 Silica Paste; (e) 11 Silica Paste; (f) 13 Silica Paste, (g) 16 Silica Paste (this panel has a different velocity scale than the other panels).	98
4.7 (a) Velocity magnitudes on the horizontal plane where the ROI was calculated as a function of the non-dimensional radial position (r/R) for all complex fluids studied in this work ($\Delta P = -0.14$ bar, $C = 1.75$ mm, $d/D = 0.119$). Horizontal dotted line shows the velocity value at which the ROI was calculated ($\bar{v} = 0.001$ m/s); (b) Dependence of the reduced heel, ΔV_H , on fluid rheology for all the complex fluids studied in this work.	99
4.8 Dependence of ROI on the reduced heel, ΔV_H , on the fluid rheology: (a) reduced heel results for all the complex fluids; (b) dependence of ΔV_H on the effective yield stress, σ_0 , of the same fluids. The dashed line shows Equation (3.6), which was derived in our previous work (see Chapter 3) based on a much wider range of fluids using CFD results.	99
4.9 Velocity magnitude contour maps for selected complex fluids discharged with different d/D ratios ($\Delta P = -0.14$ bar, $C = 1.75$ mm): (a) 1.0 Xan fluid; (b) 1.5 Xan fluid; (c) 2.5 Xan fluid.	102

LIST OF FIGURES
(Continued)

Figure	Page
4.10 Velocity magnitudes on the plane where the ROI was calculated using different d/D ratios but constant ΔP (-0.14 bar) for (a) 1.0 Xan fluid; (b) 1.5 Xan fluid; (c) 2.5 Xan fluid; and (d) dependence of ROI on d/D for the same fluids. Horizontal dotted lines show the velocity value at which the ROI was calculated ($\bar{v}=0.001$ m/s).	103
4.11 Dependence of the reduced heel volume, ΔV_H , on d/D for selected rheologically different fluids ($\Delta P=-0.14$ bar, $C=1.75$ mm).	103
4.12 Velocity magnitude contour maps for selected complex fluids discharged at different suction pressures, ΔP ($d/D=0.119$, $C=1.75$ mm): (a) 1.0 Xan; (b) 1.5 Xan; (c) 2.5 Xan.	105
4.13 Velocity magnitudes on the plane where the ROI was calculated using different ΔP ratios but constant d/D ($=0.119$) for (a) 1.0 Xan fluid; (b) 1.5 Xan fluid; (c) 2.5 Xan fluid; and (d) dependence of ROI on ΔP for the same fluids. Horizontal dotted lines show the velocity value at which the ROI was calculated ($\bar{v}=0.001$ m/s). Note that in Panel (a) an additional profile was added (for $\Delta P=-0.045$ bar).	106
4.14 Dependence of the reduced heel volume, ΔV_H , on ΔP for selected rheologically different fluids ($d/D=0.119$, $C=1.75$ mm).	106
4.15 Dependence of ROI on the reduced heel, ΔV_H , for rheologically different fluids and with various operating parameters ($C=1.75$ mm). The yellow symbols represent the same results presented in Figure 4.8b.	107
4.16 Results of statistical analysis: (a) dependence of ΔV_H on the volumetric flow rate according to Eq. 4.6; (b) parity plot for ΔV_H vs. $\Delta V_{H-Correlation}$ obtained using the statistical model represented by Eq. 4.5.	111
4.17 Comparison of computationally predicted (CFD) and experimentally determined (PIV) velocity magnitude contour maps.	113
4.18 Comparison of computationally predicted (CFD) and experimentally determined (PIV) ROI. Note that the ROI results of 16 Silica are not shown since they were both 0.	114

LIST OF FIGURES
(Continued)

Figure	Page
5.1 Portion of the bottle that is optically monitored. Note that the black dashed lines represent the region analyzed by using <i>Method 1</i> , whereas the red dashed lines represent the region analyzed by using <i>Method 3</i>	125
5.2 Velocity magnitude contour maps and the corresponding heel profiles for three different orifice shapes obtained by <i>Method 1</i> and <i>3</i> , respectively.	131
5.3 PIV output for one angled cut orifice at zero clearance ($C=0$ mm): (a) Velocity magnitude contour map and the corresponding heel profile obtained by <i>Method 1</i> and <i>3</i> , respectively; (b) velocity magnitude distribution map corresponding to a close look on the right half of the bottle obtained by <i>Method 1</i> . The velocity vectors in Panel (b) are in the region delimited by the white box in Panel (a).	132
5.4 Comparison of heel obtained by <i>Method 4</i> at various clearances and orifice shapes. Error bars represent 95% confidence intervals, obtained by five repetitions of each experiment.	132
5.5 Comparison of volumetric flow rate at $C=0.5$ mm for all types of orifices studied in this work. Error bars represent 95% confidence intervals, obtained by four repetitions of each experiment.	133

NOMENCLATURE

A	Cross-sectional area available for flow (m ²)
A_{or}	Cross-sectional area of the orifice (m ²)
C	Tube orifice clearance from the peak of the bottle bump (mm)
C_d	Orifice discharge coefficient
d	Tube or orifice inner diameter (m or mm)
d_o	Tube outer diameter (mm)
D	Vessel, pipe, or bottle inner diameter (m)
D_B	Bottle outer diameter (mm)
Eu	Euler number
g	Gravitational acceleration (m/s ²)
h_B	Bottle total height (mm)
h_{or}	Elevation of the orifice (m)
ROI	Region of influence
k	Flow consistency index (Pa.s ⁿ)

k_{or}	Orifice pressure loss coefficient
L	Orifice length (m)
n	Flow index
ΔP	Suction pressure generated by the pump (bar)
ΔP_{or}	Pressure drop across the orifice (Pa)
p_{wor}	Wetted perimeter of the orifice cross-section (m)
r	Radius of any selected point on the radial plane of the bottle (mm)
R	Radius of the bottle (mm)
Re	Reynolds number
ΔV_H	Reduced heel volume (cm ³) (see text)
ΔV_{H-CFD}	Reduced heel volume obtained with the CFD method (cm ³)
ΔV_{H-EXP}	Experimentally determined reduced heel volume (cm ³) (see text)
$\Delta V_{H-EXP-Predicted}$	Predicted reduced heel volume using Equation 3.6 (cm ³) (see text)
$\Delta V_{H-Correlation}$	Predicted reduced heel volume using Equation 4.5 (cm ³) (see text)
V_H	(Total) Heel volume (cm ³)

V_{H-CFD}	Heel volume obtained with the CFD method (cm ³)
V_{H-PIV}	Heel volume obtained with the experimental imaging method (cm ³)
$V_{H-Weight}$	Heel volume obtained with the experimental weighing method (cm ³)
V_{H0}	Fluid volume below the lower end of the dip tube (cm ³)
Q	Volumetric flow rate (m ³ /s)
\bar{v}	Velocity magnitude (m/s)
v_i	Axial velocity (m/s)
v_j	Radial velocity (m/s)
$\dot{\gamma}$	Shear rate (s ⁻¹)
λ	Time constant in Carreau model (s)
η	Dynamic viscosity (Pa·s)
η_0	Low-shear viscosity limit (Pa·s)
η_∞	High-shear viscosity limit (Pa·s)
ρ	Fluid density (kg/m ³)
σ	Shear stress (Pa)

σ_0 Effective yield stress (Pa)

σ_y Yield stress (Pa)

CHAPTER 1

INTRODUCTION

1.1 Background and Significance

Complex fluids consist of mixtures in which two phases coexist, including mixtures of solids in liquid (such as suspensions or solutions of macromolecules), liquids in liquid (emulsions), and gases in liquids (foams). Examples include milk, yogurt, chocolate, cosmetics, paint, blood, and mucus [1]. Complex fluids can be considered homogeneous at the macroscopic scale but are heterogeneous at the microscopic scale. For example, in the case of colloidal crystals, such as a cornstarch suspension, the microscopic scale includes both the water molecules and the cornstarch grains ($\sim 1 \mu\text{m}$), whereas the macroscopic scale is on the order of magnitude of the size of the containers, such as a cup ($\sim 10 \text{ cm}$), at which scale the fluid appears homogeneous [2, 3]. Such fluid will respond quite differently to applied stress, depending on the solids' size, solids concentration, and the arrangement of the solids in the suspending liquid. Hence, the macroscopic flow behavior (rheology) of complex fluids is a strong function of the fluid microstructure. Some examples of complex fluids are shown in Figure 1.1.

Unlike Newtonian fluids for which the viscosity does not change when the fluid is sheared, complex fluids typically possess non-Newtonian characteristics, which may include shear-dependent and/or time-dependent viscosity, yield stress, elastic effects, and others [4]. In many cases, the non-Newtonian properties of complex fluids can be advantageous since those characteristics are often used to obtain fluids with desired and useful mechanical properties stemming from the variety of their structures [5, 6]. For instance, when a toothpaste (a silica suspension in a humectant (glycerin or sorbitol))

solution [7, 8]) is extruded on a toothbrush, it does not run off but it holds its shape, as intended [9]. Similar behavior is obtained with mayonnaise, mortar, concrete, and many other fluids [10].



Figure 1.1 Examples of complex fluids: paint (left panel) and toothpaste (right panel). Sources: <https://en.wikipedia.org/wiki/Paint> (Retrieved on 10/26/2022), <https://en.wikipedia.org/wiki/Toothpaste> (Retrieved on 10/26/2022).

However, in the case of a discharge from industrial equipment or from consumer products, where high rates of discharge (i.e., shorter discharge time) are desired, the complex rheological behavior of these fluids may become problematic since it typically slows down or even prevents the discharge process because of high viscosity, yield stress, and viscoelastic properties, all of which increases as the disperse phase concentration increases. Figure 1.2 shows the common types of fluid behavior under shear.

The discharge of a fluid through an orifice from industrial tanks, pipes, or any other type of container or packaging is an old and, in many cases, complex problem. As far as Newtonian liquids are concerned, this topic has received significant attention and has been discussed extensively in the literature for fluids having both low viscosity [11-15] and high viscosity [16, 17]. As a result, correlations are available to characterize their fluid discharge behavior, typically through the experimental determination of the discharge rate

through orifices and the interpretation and correlation of the data to extract non-dimensional discharge parameters of general applicability, such as discharge coefficients (C_d) or pressure loss coefficients (k_{or}) which are, essentially, parameters representing the mechanical energy losses in the orifice due to friction and contraction (by relating the actual flow rate to the theoretical flow rate) [12, 14, 18-23].

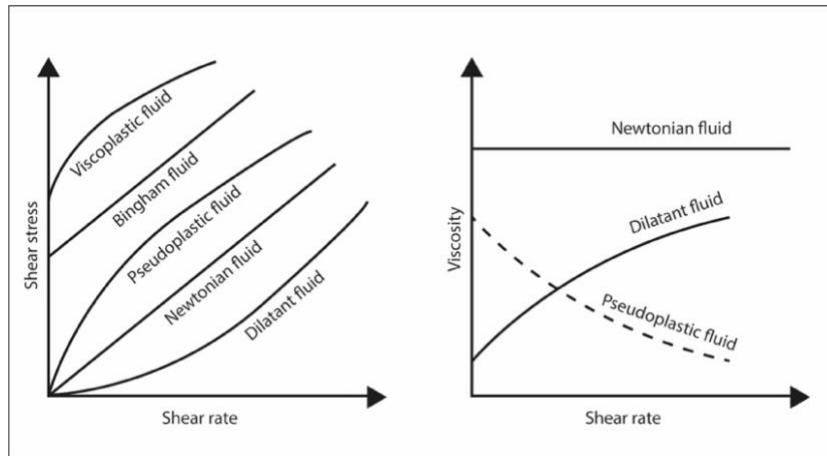


Figure 1.2 Shear stress-shear rate dependence for common fluids in simple shear. Source: [24].

However, the literature on the discharge of complex fluids, such as paints, ketchup, shampoos, hand sanitizers, or toothpaste, is much more limited although these fluids are often encountered in industry and are typically required to be easily and nearly completely discharged from their vessels, containers, tubes, and dispensers for personal use. The most common examples of commercial complex fluids along with their packaging, i.e., the bottles with hand pumps, and squeezable tubes, are shown in Figure 1.3. In these processes, the material is expelled from a larger cylinder through a smaller orifice, under its own weight in the case of drainage, or by an externally applied pressure in the case of hand-pumping the fluid out from a bottle, or extruding it from a squeezable tube [25].

Handling non-Newtonian fluids during drainage can be challenging, particularly under laminar flow conditions, because of their complex rheological behavior [26-28]. The rheological characteristics of these fluids often depend on the size and distribution of particles that they may contain, the concentration of those particles, dimensions of the conduit, flow regime, temperature, and dynamic viscosity of the liquids, and other rheological parameters [29].



Figure 1.3 Examples of most common commercial complex fluids in various packaging: (a) bottles of different geometries with hand pumps for hand sanitizers, dishwashing liquids, lotions, and gels; (b) a squeezable tube having toothpaste product.

The control and optimization of discharge processes require knowledge of the effects of all these variables on the non-dimensional discharge parameters [30]. Correlations predicting the discharge coefficients for complex fluids are available, at least for a limited number of fluids [17, 18, 29, 31-36]. However, this information is often unavailable for many other fluids since the role of those variables on their discharge is still not well understood and correlations for orifice discharge are not easily available. As a result, engineers working with these materials cannot often predict the orifice flow rates and have to rely on experimentation. This is especially significant for a number of fluids for which the rheological characterization has proven to be quite challenging, especially if

the fluids have viscoelastic or thixotropic properties [37], which is often the case for complex fluids.

The diagram in Figure 1.4 shows examples of fluids that are typically used in the industry, from low to high complexity (larger fraction of the disperse phase). Accordingly, a *gel* can be obtained when a polymer (e.g., xanthan gum, carbopol, CMC, etc.) is mixed with a liquid [7]. A gel has been defined phenomenologically as a soft, solid-like material consisting of two or more components, one of which is a liquid, present in substantial quantity [38]. Gels typically possess shear-thinning characteristics and they are the most common types of complex fluids in personal and oral care industries (e.g., hand sanitizers, lotions, hand soaps, dishwashing liquids, etc.), pharmaceutical drug delivery systems, biomaterials, and many others [39].

When finely divided solid particles (typically silica) is added to the gel, a *paste* (e.g., mustard, toothpaste) can be obtained [7]. In physics, a paste is a substance that behaves as a solid until a sufficiently large load or stress is applied, at which point it flows like a fluid [4]. In terms of rheology, paste is an example of a yield-stress fluid. Clearly, a paste has more complex rheological properties than a gel, such as much more pronounced yield stress, thixotropy, and shear thinning properties. Nevertheless, surprisingly, hardly any studies are present to characterize the discharge behavior of gels and paste from bottles, tubes, hand pumps, or simply, orifices. However, one should note that the characterization of the discharge from these geometries through non-dimensional discharge parameters relating the actual flow rate to the theoretical flow rate (e.g., C_d and k_{or}) would be more challenging when one wants to characterize the discharge behavior of gels and pastes, and the accuracy of these correlations will decrease every time when a new variable is

introduced in the discharge equation, such as viscoelasticity, thixotropy, yield stress, and shear viscosity.

Therefore, a more detailed understanding of discharge hydrodynamics of complex fluids is needed. These include the determination of the velocity distribution within the fluid to be discharged using experimental flow monitoring techniques such as particle image velocimetry (PIV), or computational methods such as computational fluid dynamics (CFD), from which useful data describing the discharge hydrodynamics can be extracted and analyzed. In addition to the abovementioned discharge issues and the lack of knowledge in the field, other issues may arise with complex fluids, typically related to remnants of fluids left in the container at the end of the discharge process because of yield stress and viscoelastic properties of the fluids acting against their flow. This residual material often referred to as *heel*, can result in losses of material, fouling of the container, and, as far as the industrial processes are concerned, complex cleaning steps to avoid compromising the quality of the new batch of product in the same container [40].

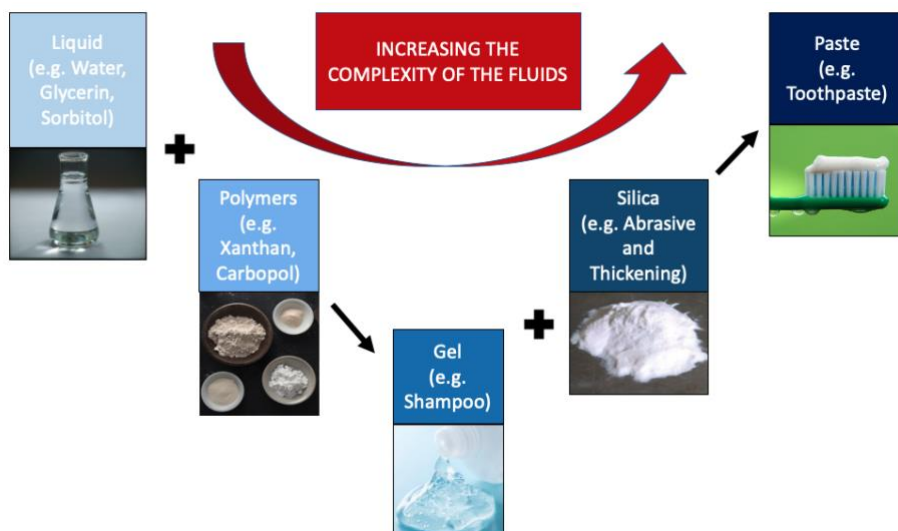


Figure 1.4 Diagram showing the increased complexity of the fluids frequently used in the oral care product industry.

Frequently, operators are concerned about the heel mainly from the point of view of the tank cleaning [41]. A full tank discharge effectively eliminates or greatly minimizes these residual products and helps maintain cleanliness. In addition, without a proper full discharge system, process operators may need to enter a tank and incur the risk of coming in contact with or inhaling hazardous chemicals in the confined space. This could be especially dangerous when harmful chemicals are being processed or stored, which, in addition, could cause contamination of the upcoming batch. However, to this date, information on the formation of a heel is scarce and this topic remains largely uninvestigated, especially for consumer packaging of various geometries.

Ideally, the discharge process should occur rapidly and result in a negligible amount of heel. This could be especially important in contraction flows since the low-shear zones near the contraction contribute significantly to the mechanical energy loss [40, 42]. Thus, if the flow characteristics of the complex fluid of interest are not well understood, and the equipment/orifice is not designed properly, the discharge process of complex fluid and the formation of a residual heel can become problematic.

1.1.1 Factors Affecting the Discharge of Complex Fluids through Orifices

Previous research has shown that the geometry of the orifices, including the shape of the orifice (e.g., circular, triangular, square), the diameter ratio d/D , and the aspect ratio, L/d , affect the mechanical energy losses at the orifice that are quantified by using discharge coefficients (C_d) or pressure loss coefficients (k_{or}) [12, 19, 21, 31-33, 35, 36, 43-50].

To account for the shape of the orifice, many researchers calculated the Reynolds number [51-56] using the orifice hydraulic diameters, defined as $d_{hor}=4A_{or}/p_{or}$, where d_{hor} is the hydraulic diameter of the orifice (m), A_{or} is the cross-sectional area of the orifice

(m^2), and p_{wor} is the wetted perimeter of the orifice cross-section (m) [57]. For Newtonian fluids, Wang et al. found that circular orifices produce a more stable flow than square-shaped orifices [45]. Novak et al. investigated gas flow through orifices of different shapes and found that the discharge coefficients of narrow rectangular orifices were much higher than discharge coefficients for comparable circular orifices. They observed the same phenomenon for triangular orifices, but they added that this effect decreases with increasing orifice area [44]. For power-law and yield stress fluids, however, a recent study conducted by Khahledi et al. showed that the orifice shape does not have any effect on the discharge coefficient, including the triangular shape since the effect of the orifice shape becomes negligible compared to the high viscous properties of non-Newtonian fluids, which dominate the characteristics of the flow [29]. These results are in line with the previous study of Ntamba for the pipe discharge of complex fluids [19], but how the orifice shape affects the discharge of complex fluids from more complicated systems, such as from a dip tube of a hand pump in a dispensing bottle, still remains to be investigated.

The discharge process is affected not only by the orifice diameter but also by the orifice length L , since both the external friction (caused by adhesion between the fluid and the orifice wall) [58], and the internal friction of the fluid (viscosity) at the outlet vary with orifice length and diameter. As far as the orifice length is concerned, increasing the orifice length L typically results in higher mechanical energy loss due to prolonged friction, therefore decreasing the discharge rate. This was thoroughly studied by several researchers but only for a limited L/d range [16, 17, 29]. Chowdhury and Fester, and Bohra studied orifices with L/d ratios larger than those commonly found in consumer packaging, such as lotion bottles, that have a long pipe and a pump at the end [16, 33, 35]. It should also be

noted that while increasing the length of the orifice usually results in higher mechanical energy losses, the diameter of the orifice may also contribute to this, as shown by Ntamba and Fester [34], and Chowdhury and Fester [35]. Typically, as the diameter of the orifice increases, the pressure loss coefficient decreases (or C_d increases). In summary, understanding the effect of the orifice geometry (orifice shape, length, and diameter) on the discharge of complex fluids is important in the accurate design of discharge equipment.

The discharge process is also significantly affected by the rheology of the fluid, especially if complex. In general, the main rheological property that can reduce the discharge rate is a large value of the fluid viscosity [4]. In complex fluids, this is especially significant, and high viscosity implies higher mechanical energy loss in the laminar regime. In addition, complex fluids may have varying viscosity. Hence, proper rheological characterization and relating the rheological properties of the fluids to the other parameters affecting the discharge process is critical. Dziubinski and Marcinkowski used various concentrations of CMC solutions in their experiments and showed that solutions with higher viscosity yielded lower C_d when all other geometric constraints were kept similar [17]. A similar phenomenon was observed in orifice flows in a pipe where k_{or} was found to increase with increasing fluid viscosity, i.e., lower Reynolds numbers [34, 35], indicating, again, that high viscosity slows down the discharge process.

Additional investigations examined the effect of the yield stress as well as viscosity. The effect of yield stress was studied using concentrated kaolin or bentonite suspensions [29, 35, 59] and carbopol gels [30] showing that at low Reynolds numbers these fluids do not discharge at all. Furthermore, Toplak et al. showed that when carbopol gels of higher viscosity are used during their gravitational draining of a vessel, the decreasing height of

the fluid tends to stabilize at higher values, therefore decreasing the discharge rate, and contributing to the formation of a heel [30].

Although often ignored, another rheological property that significantly affects the discharge process is the viscoelasticity of the fluid, defined as the property of a substance exhibiting both elastic and viscous behavior [4]. This may result in high extensional viscosity, commonly known as *stringiness* in the industry [9, 60], where the fluid forms a filament (or string) during the discharge, slowing its discharge rate. Ahuja and Potanin specifically emphasize the industrial importance of stringiness, as it affects production at filling stations since filling lines often operate at set (high) speeds and stringiness can interfere with reproducible filling and can slow the line operation [9]. Previously, it was also shown that the extensional properties of the fluid at the entrance region of a contraction can lead to an additional pressure drop [50, 61]. Della Valle et al. found that the extensional viscosity could have an effect on the flow three times as high as that of the shear viscosity [48]. These results were similar to the findings of Sridhar for a Boger fluid (defined as a fluid that exhibits significant elastic properties while viscosity remains independent of shear rate) [62]. Recently, and for the first time, Rituraj and Vacca quantified the viscoelastic effects on the discharge and included it in their discharge model [31].

Wall slip is another phenomenon that should be taken into account in discharge investigations [58, 63, 64]. When a thin layer of fluid remains on the vertical walls of the vessel during the discharge, it indicates that the slip on the vessel walls is negligible. However, the presence of wall slip would imply a finite velocity of the fluid at the wall so that no material would remain on the wall behind the flow [30]. This would be beneficial as far as the discharge rate is concerned. However, wall slip could also result in inaccurate

viscosity determination during the rheological characterization of the fluid. Chhabra and Richardson warn that serious errors could occur when the wall slip is not accounted for [65]. They suggest that to account for the wall slip, more than one diameter tube should be tested during rheological measurements to precisely understand the rheological characteristics of the fluids to be investigated. Hence, it is important to ensure that discharge investigations are conducted in equipment with no-slip boundary conditions.

The factors affecting the discharge of the complex fluids and the theoretical background presented until this point clearly shows that more experimental data are needed to better understand all the above-mentioned effects on the discharge process. These will be discussed later in detail.

1.1.2 Rheological Characterization of Complex Fluids

In order to understand the hydrodynamics during the discharge process of a complex fluid, their rheological characterization is crucial. The characterization typically involves the measurement of the fluid flow properties over an appropriate shear rate (or shear stress) range [4, 65, 66]. There are several available models to rheologically characterize the fluids, where Bingham, Herschel-Bulkley, Ellis, Casson, and Carreau models being the most common ones [4, 67]. Among those, the Herschel-Bulkley model is widely used for characterizing the non-Newtonian liquids having a yield stress [4]:

$$\sigma = \sigma_y + k\dot{\gamma}^n \quad (1.1)$$

where, in SI units, σ is the shear stress (Pa), σ_y is the yield stress (Pa), k is the flow consistency index ($\text{Pa}\cdot\text{s}^n$), $\dot{\gamma}$ is the shear rate (s^{-1}), and n is the flow behavior index. While

n defines the degree of non-Newtonian behavior of the fluid, k defines its consistency: the larger the value of k the “thicker” or “more viscous” the fluid [56]. In addition, if $0 < n < 1$, the fluid shows pseudoplastic or shear-thinning behavior. Here a smaller value of n means a greater degree of shear-thinning. If $n=1$: the fluid is considered as a Bingham fluid. If $n > 1$: The fluid shows dilatant or shear-thickening behavior with a higher value of n resulting in stronger shear-thickening. If $\sigma_y=0$, then the fluid is considered a power-law fluid, represented by the equation:

$$\sigma = k\dot{\gamma}^n \quad (1.2)$$

Here, it should be reminded that the existence of a “true yield stress” has been a long debate in the literature. Barnes argued that the yield stress is nothing more than an extrapolation, and with a rheometer having an enhanced resolution, one may see that the fluid acts as a Newtonian fluid at very low shear rates below the yield point [68, 69]. According to this approach, everything flows if the time scale is enough. Hence, models such as Herschel-Bulkley that represent “true” yield stress may fail to accurately describe the fluid deformation at stresses below the yield point as the yield stress is determined by an extrapolation of the curve to zero shear rate, which ignores the fluid deformation before the inception of the flow. This is especially critical if the fluid has thixotropic behavior, as the fluid may be “disturbed” before its flow during the rheological measurement, causing the misdetermination of the rheological parameters of the fluid especially if proper geometries are not used [37, 70-81].

Moreover, Herschel-Bulkley model may also fail to accurately represent the fluid

behavior at very high shear rates such as 1000 s^{-1} , which typically corresponds to a shear rate during the pumping of complex fluids through pipes or tubes [25]. The reason is that fluids tend to become more Newtonian at high shear rates (thus giving the high-shear plateau, or equilibrium viscosity), and the power-law fit will fail to capture the plateau accurately (as the curve will bend down and flatten out at high shear rates, moving away from the power-law fit).

Therefore, for the cases in which the fluid behavior at very low and very high shear are significant, Carreau model can be used as it enables capturing low and high shear plateaus [82], as will be described later in detail. In this work, the fluid behavior at very low- and high- shear rates are both significant, as the former corresponds to the region in the bottle closer to the dispensing bottle wall that may impact heel formation, the latter is directly related to the dip tube region which has a much higher shear distribution. Hence, for the purposes of this work, the Carreau model will be used to accurately capture both the low- and high- shear viscosity limits.

1.1.3 Experimental and Computational Tools Used for Flow Monitoring

Several experimental and computational methods have been utilized to investigate hydrodynamics in mixing and flow studies. However, surprisingly, they have never been used to study discharge hydrodynamics. Although a comprehensive review of the flow monitoring techniques can be found elsewhere [83], the most commonly used techniques that are also used in this work (PIV and CFD) are briefly reviewed here but will be discussed later in greater detail.

1.1.3.1 Particle Image Velocimetry (PIV). Velocity measurements using PIV are based on flow visualization and image processing. A PIV system typically consisted of a double-

pulsed laser combined in a single unit, both yielding a light emission at a 532 nm wavelength that passes through an optical lens and generates a laser light sheet, as reported previously [84].

The laser light sheet illuminates the seeding particles that are suspended inside the fluid, and the camera captures multiple image pairs while the fluid is in motion. Then, the distance that particles traveled between the image pairs is determined through a cross-correlation analysis, which eventually yields a velocity vector at each point within the investigated region of the fluid. The seeding particles utilized in PIV studies have to be small enough to follow the fluid flow (Stokes Number $\ll 1.00$) but large enough (typically larger than 10 μm) to scatter the laser light. The most common examples of such seeding particles are polyamide or fluorescent seeding particles. PIV is advantageous over other flow measurement methods, e.g., Laser Doppler Velocimetry (LDV) [61, 83], and Electrical Resistance Tomography (ERT) [85-106], as it can rapidly capture velocities over an entire cross-section with a very high resolution.

In this work, the PIV technique was used to investigate the hydrodynamics during the discharge of complex fluids from a dispensing bottle, which is equipped with a hand pump. More specifically, the lower region of the bottle including the dip tube of the hand pump was monitored during and after the discharge to obtain useful information about the discharge hydrodynamics as well as the heel profiles and volumes.

1.1.3.2 Computational Fluid Dynamics (CFD). Computational Fluid Dynamics (CFD) could be a useful tool to better predict the hydrodynamic characteristics of the discharge of complex fluids hence yielding more accurate modeling of the orifice flow for any orifice geometry or to study the effect of the fluid rheological properties.

CFD has been an increasingly important computational tool used to analyze and quantify complex fluid flow systems by solving the appropriate conservation equations (mass, momentum, and energy balance equations) that describe the flow [107, 108]. The analysis typically incorporates four main components, i.e., geometry definition and mesh generation, setting-up of a physical model, numerically solving the conservation equation with the appropriate boundary conditions, and post-processing the result to extract useful information such as velocity distributions in the investigated system. CFD approach has been used extensively in hydrodynamic prediction in mixing and fluid flow systems [49, 108-114]

In the present case, ANSYS Fluent package with a simplified generalized Newtonian approach was used. More specifically, the geometry of the lower region (up to 20 mm in height) of the dispensing bottle apparatus was drawn based on real dimensions, and the resulting volume is divided into a number of cells by defining a computational mesh. The proper boundary conditions were applied based on the problem, and the laminar model was used. The CFD software numerically solved the general equations representing the conservation of mass and momentum. CFD results were then validated experimentally using Particle Image Velocimetry (PIV), which was described earlier.

1.2 Overall Research Objectives of This Dissertation Work

It is apparent from the brief introduction above that although general correlations representing the discharge of complex fluids through orifices are available for a limited amount of fluids, a more in-depth analysis of the fluid dynamics of the discharge process of complex fluids of a wide range of fluid rheology is needed to improve industrial equipment and consumer packaging design. Furthermore, all the previous work on orifice discharge was conducted in vessels or pipes. Hence, surprisingly, significant gaps were observed in the literature on the discharge studies of such fluids from dispensing bottles which are more commonly utilized in daily life. If such processes are better understood, the design of consumer packages and dispensers can be improved so that the product is expelled more quickly and efficiently, and residual waste is decreased. These issues involve, once again, the determination of which parameters affect the discharge process, and the prediction of the discharge behavior of such fluids.

Therefore, the overall objective of this work is to quantify the hydrodynamic characteristics of complex fluids discharged from consumer packaging, more specifically from dip tube orifices of the dispensing bottles, through the use of experimental and computational approaches. The particle image velocimetry (PIV) approach could be useful for the hydrodynamics investigations of the discharge process since it is a well-established non-invasive optical technique for measuring the velocity field in fluids. Furthermore, its high-intensity double-pulse laser which can penetrate inside fluid of interest, and its simultaneous high-speed image-capturing capabilities could carry additional importance for monitoring such fast-occurring, transient processes. In addition, to achieve the most effective and meaningful approach for studying flow fields, a computational approach

using computational fluid dynamics (CFD) will be used and compared with the experimental (PIV) results. As a result, robust knowledge on the discharge hydrodynamics of fluids of low to high complexity, including optimizing critical parameters in the process such as the transparency of such fluids for their optical investigations, can be established.

In summary, the overall objective of the work is to provide a detailed insight into the system hydrodynamics and conduct a detailed experimental investigation aimed at fully characterizing the velocity and heel profiles in different consumer packaging, which should alleviate the need to better understand not only how the fluid rheology affects the discharge, but also how the bottles, tubes, and orifices, should be better designed in order to obtain an improved discharge efficiency and reduced the amount of heel. Figure 1.5 shows the conceptual framework of this research.

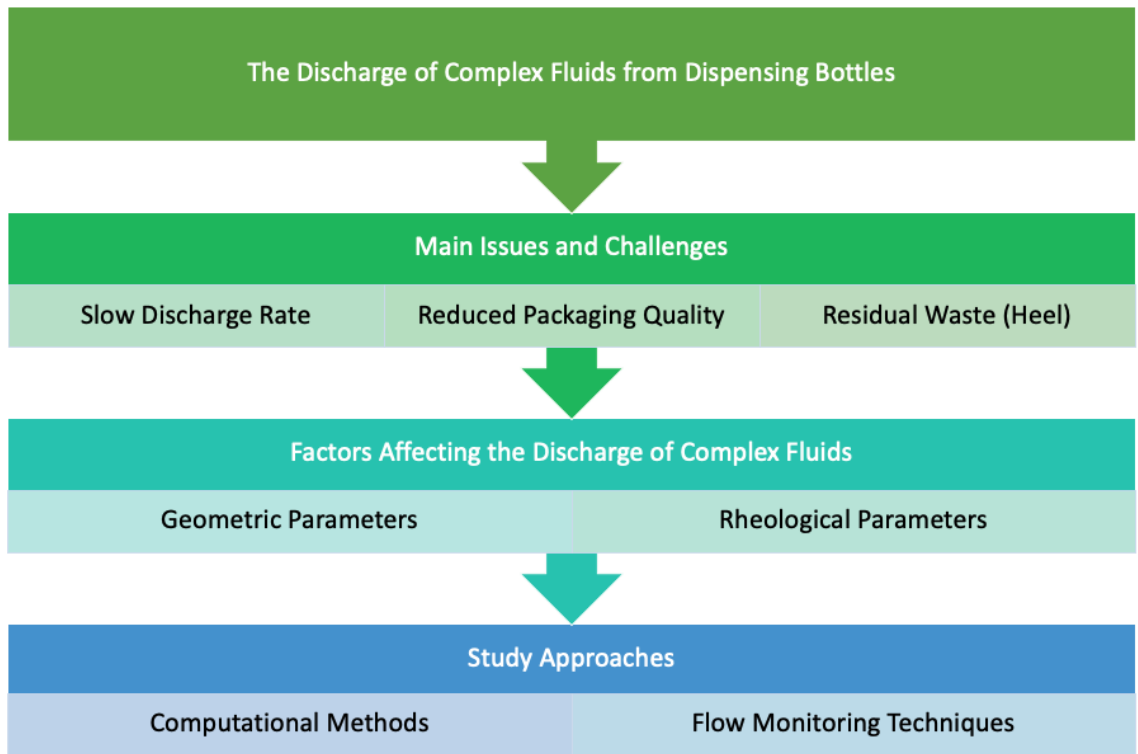


Figure 1.5 Conceptual framework of the research.

To summarize, this study attempts to address the following outstanding scientific questions:

- How to design dispensing bottles with a hand pump and their operational parameters, such as dip tube orifice shape, clearance, tube-to-bottle diameter ratio, and suction pressure generated by the hand pump, so that the discharge of complex fluids is improved, and heel amount is minimized?
- Can we develop methodologies to monitor the heel formation and determine and/or predict its volume in dispensing bottles?

1.3 Organization of the Dissertation

The material presented in this document is divided into six chapters, as follows:

Chapter 1 is an introductory chapter that provides the background and significance of the research study conducted in this work, including the overall research objectives.

Chapter 2 provides detailed information about the complex fluids preparation, specifically, such as gels and pastes, and the optimization of the optical transparency of highly complex fluids through the use of the refractive index matching method with the ultimate objective of enabling their hydrodynamic investigations using optical techniques such as PIV.

Chapter 3 presents experimental results and computational predictions of the heel volume in dispensing bottles, for a wide range of fluid rheologies.

Chapter 4 describes how the flow hydrodynamics during the discharge determines the heel profile after the discharge process for rheologically different fluids and for various operational parameters. More specifically, the effect of suction pressure, tube-to-bottle diameter ratio, and fluid rheology on the discharge hydrodynamics were investigated. Furthermore, computational methods to predict the heel volume in dispensing bottles are

presented.

Chapter 5 reports the effect of the dip tube orifice shape on the discharge hydrodynamics of complex fluids from dispensing bottles, as well as the corresponding heel profiles and volumes. More specifically, flat cut, one angled cut, and two angled cuts dip tube orifices that are commonly utilized in commercial product packaging were investigated.

Chapter 6 provides a summary and conclusion of this work.

CHAPTER 2

IMPROVING THE OPTICAL CHARACTERISTICS OF HIGHLY COMPLEX FLUIDS FOR OPTICAL INVESTIGATIONS USING THE REFRACTIVE INDEX MATCHING METHOD

2.1 Abstract

Many complex fluids such as toothpastes or other personal care products consist of suspensions of silica particles in aqueous gels of humectants and other soluble constituents. In industrial practice, it may be desirable to develop new formulations that retain the desired characteristics of the original products but also have high optical transparency. In addition, and more importantly, the development of a rheologically complex optically transparent fluids can enable the investigators to experimentally study the hydrodynamics using tools such as LDV or PIV. Here, we used the refractive index matching method to manufacture highly transparent toothpastes. Accordingly, we determined the refractive indexes of different liquid gels, each containing a different humectant concentration, and measured the light transmittance and turbidity of formulations containing those gels and the silica. By fine-tuning the humectant fraction in the gel, we obtained toothpastes with optimal transparency and also determined the effective refractive indexes of different commercial silica. All silica had similar indexes irrespective of their supplier, particle size distribution, and morphology. We believe that this approach could be extended to a wide range of highly complex fluids in order to study complex flow behavior using optical experimental methods.

2.2 Introduction

Silica particles are commonly used as additives in a number of liquid and gel products manufactured in the personal care product industries, typically as thickeners such as in toothpaste, skincare products, cosmetics, and others, or as abrasive additives in many other industrial applications [7, 115, 116]. Their presence is necessary to make a paste (a typical yield-stress fluid). Toothpaste offers a good example of a suspension of silica particles in a polymer gel in which achieving the highest transparency is desirable for optical studies of complex fluid flow investigations. In this type of product, the solid silica particles (usually referred to as “backbone” in the industry) can be of different types, such as “abrasive” or “thickening,” qualitatively describing their physical characteristics and function, and typically associated with their particle size distribution, particle sphericity, and impurity profiles. The liquid media in which these particles are dispersed is commonly an aqueous gel also containing a number of soluble additives [7].

It is well known that the optical transparency of solid suspensions in transparent or semi-transparent fluids can be maximized when the refractive index of the fluid media closely matches that of the suspended particles [117-119]. Here, one should note that while the refractive index of gels can be easily measured experimentally, that of the silica backbone cannot. However, an empirical approach has been reported in the literature to determine the *effective refractive index* of the silica, defined here as the refractive index of a fluid mixture that maximizes the optical transparency of the fluid mixture-silica suspensions when silica particles are added to it [118]. The basic method, referred to as *refractive index matching*, that has been used in the past consists of dispersing the silica particles in different fluid mixtures, each having a different refractive index, measuring the

scattered light intensity of the resulting suspension at different angles with respect to the incident light, and recording the fluid composition for which the intensity of the scattered light shows a minimum, which, for practical applications, can be associated with the maximum transparency of the suspension. The refractive index of this fluid mixture, devoid of particles, of course, can be taken as the effective refractive index of the silica [120, 121]. A comprehensive review of the literature on refractive index matching for different materials and systems is available elsewhere [119].

This approach has been successfully used previously to determine the effective refractive index of silica particles of uniform diameter and regular (spherical) shape in suspensions of low particle concentration (<0.1 wt.%) [119, 122] as well as in suspensions of concentrated particles, often for the purpose of studying the hydrodynamics of complex systems using experimental methods such as Laser Doppler Velocimetry (LDV) or Particle Image Velocimetry (PIV) [123-126].

However, this approach has never been applied to commercial suspensions of polydispersed, irregular-shaped, highly concentrated (10-30 wt. %) silica suspensions such as those commonly encountered in consumer products and related industries, with the ultimate objective of maximizing the optical transparency of the finished product. In addition, in many commercial formulations, more than one type of silica is typically used to impart specific properties to the product. For such applications, the possibility of maximizing the transparency of the product can be of primary importance not only for aesthetical purposes but also for optical investigations, and it is unclear if the approach detailed above would be generally applicable to a large number of products with similar but not identical compositions and with different types of silica of similar but not identical

characteristics in the same product.

Addressing the issue of the determination of the effective refractive index of silica particles for this broad class of suspensions could also be valuable to study the hydrodynamics of these complex but industrially relevant systems, such as the determination of the velocity distribution of suspensions in mixing vessels, pipes, distribution and dosing systems, and product dispensers, using LDV or PIV. These tools can only be used in the fluid or suspension is transparent. However, the lack of transparency of many commercial suspensions has prevented the use of these investigative tools for such industrial applications.

2.3 Experimental Equipment, Materials, and Methods

2.3.1 Equipment

Mixer. A Whip Mix WPM2 mixer (Whip Mix Corp., Louisville, KY), shown in Figure 2.1, was used to prepare gels containing water/glycerin or water/sorbitol solutions plus other soluble additives and to incorporate silica powders into the gel. This mixer was selected because (a) it operates under vacuum using a twin-chamber oil-less vacuum pump, thus minimizing the incorporation of difficult-to-remove air bubbles in viscous materials, and (b) it allows the user to pre-program speeds and mixing times for specific materials, including a premixing stage that eliminates the need for hand incorporation of powders by using alternating paddle direction.



Figure 2.1 Whip Mix WPM2 Mixer.

Refractometer. A laboratory digital refractometer (Sper Scientific Laboratory, Model No. 300033) was used to measure the refractive index of the base liquid gels used in this work. This instrument is capable of measuring refractive indexes in the range 1.4098 to 1.5318 with an accuracy of ± 0.001 and requiring only low-volume samples (0.4 mL). The refractometer is shown in Figure 2.2a.

Turbidimeter. Turbidity measurements are simple and effective ways to measure the optical characteristics of a suspension [127, 128]. In this work, a portable turbidimeter (Hach-2100Q, Hach Co., Loveland, CO), as shown in Figure 2.2b, was used to measure the turbidity of silica gel-silica dispersions (formulations). This type of instrument uses a nephelometric technique to measure the intensity of light scattered at a 90° angle from an incoming light beam generated by a tungsten filament lamp. This instrument has the capability of measuring turbidity from 0 to 1000 NTU, with an accuracy of $\pm 2\%$ of reading (plus stray light), and repeatability of $\pm 1\%$ of reading or 0.01 NTU (whichever is greater). Therefore, the samples having turbidity values exceeding 1000 NTU were discarded.



Figure 2.2 Portable equipment used in this work: (a) Sper Scientific Laboratory 300033 refractometer and (b) Hach-2100Q turbidimeter.

Light Transmittance Analyzer. Optical light transmittance through the sample was measured independently by a Turbiscan™ LAB stability analyzer (Formulation, France) [129, 130]. The apparatus and the technique are represented in Figure 2.3.

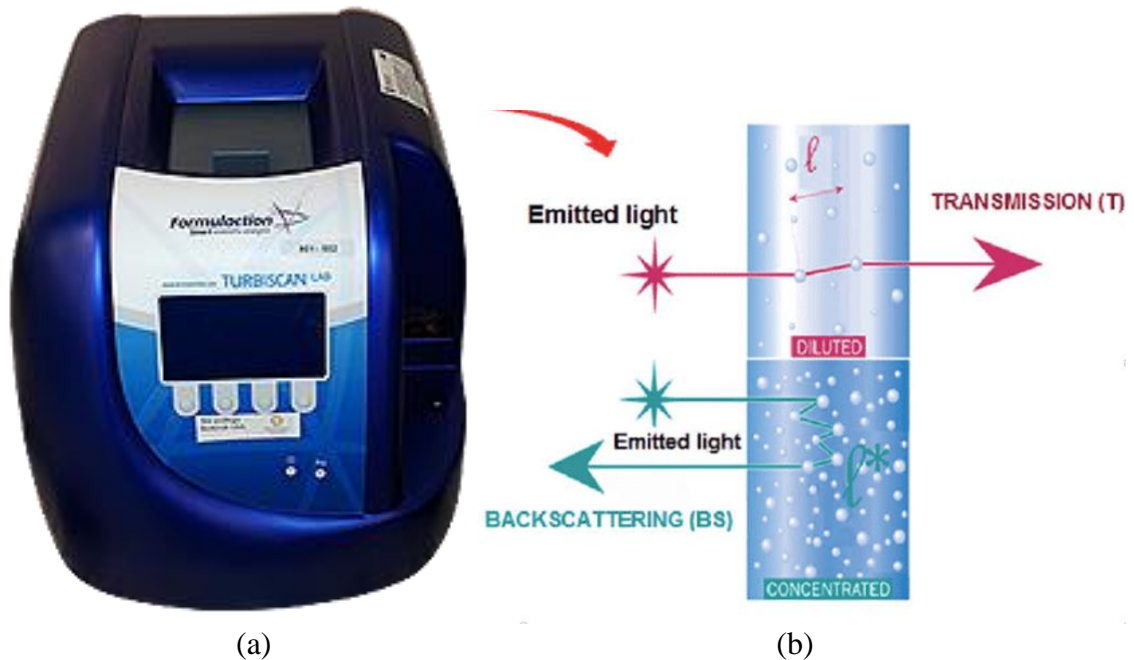


Figure 2.3 Light transmittance analysis technique used in this work: (a) Turbiscan™ LAB stability analyzer and (b) illustration showing the transmission and backscattering of light for the cases of diluted (or the cases in which the refractive index of the particles are identical to the liquid) and concentrated (or the cases in which the refractive index of the particles are different from that of the liquid) solutions, respectively.

This apparatus is widely used in industry to characterize the stability of various products. A pulsed near-infrared light source (wavelength=880 nm) passes light through the sample. The light emerging from the sample is detected by two synchronous detectors, i.e., a transmission detector receiving the light going straight across the sample and a back-scattering detector measuring the intensity of the light scattered backward by the sample at 135° from the incident beam, both reported as a percentage of transmitted light reaching the light detectors. In addition, this apparatus can vertically optically scan the sample in the measurement cell to detect particle settling/migration phenomena over time, resulting in vertical profiles of percentage transmitted and backscattered light. In our study, we used this apparatus to measure only the percentage of transmitted light across a 10 mm vertical sample and reported the highest value measured by the instrument in this vertical range.

2.3.2 Materials

Two formulations were used here to determine the effective refractive index of the silica particles used in toothpaste (as well as to obtain optimally transparent final products), each one containing different concentrations of the soluble components of the generic toothpaste and different types and concentration of silica particles.

Two gels of different compositions, i.e., *Gel 1* and *Gel 2* (as shown in Table 2.1) were prepared. *Gel 1* contained only xanthan gum, different amounts of a humectant (either glycerin or sorbitol) depending on the experiment, and the balance water. *Gel 2* contained polyethylene glycol, xanthan gum, either glycerin or sorbitol as a humectant, a number of flavors, sweeteners, surfactants and active ingredients, and the balance water. The compositions *Gel 2* is also provided in Table 2.1, although the exact composition of the active ingredients is not reported for proprietary reasons.

Gel 1 and *Gel 2* were the bases for the actual toothpaste formulations, i.e., *Formulation 1* and *Formulation 2*, respectively, as reported in Table 2.2. In any given experiment, the humectant used in both formulations was either glycerin or sorbitol (no formulation included both), but their concentration was varied so as to determine the optical humectant concentration resulting in gels whose refractive indexes matched more closely those of the silica particles.

The two formulations also differed in the amount and type of silica used. *Formulation 1* contained 16 wt. % total silica, whereas *Formulation 2* contained 23 wt. % total silica. The type and composition of the silica used in the formulations were also different. *Formulation 1* contained two types of silica, referred to here as Silica 1 and Silica 3 (J.M. Huber Corporation). Micro-photographs of these two types of silica particles are shown in Figure 2.4. Their particle size distributions were measured with a particle size analyzer (PSS AccuSizer 780 SIS, Soliton, Germany) by taking a sample of *Gel 1* to which only one type of silica had been added and diluting it in water to achieve a 0.03 wt. % silica dispersion. The size distributions of both types of silica are reported in Figure 2.5. Both of them were also used in previous work by our group [131]. Here, one should notice that Silica 1 had a larger fraction of larger particles, making it more suitable in applications requiring high abrasive, whereas Silica 3 had a lower mean particle size, but a broader distribution than Silica 1. *Formulation 2* contained Silica 3 as well as another type of silica, referred to as Silica 2, whose characteristics are not reported here for proprietary reasons. Furthermore, in order to investigate the effects of the gel type on the refractive index, additional experiments were conducted with a non-commercial formulation (labeled here *Formulation 3* for convenience, although only used for

comparison purposes) containing *Gel 2* and the same amount and type of silica as in *Formulation 1* (8 wt. % of Silica 1 plus 8 wt. % of Silica 3), as reported in Table 2.2. Only glycerin was used as a humectant in these experiments.

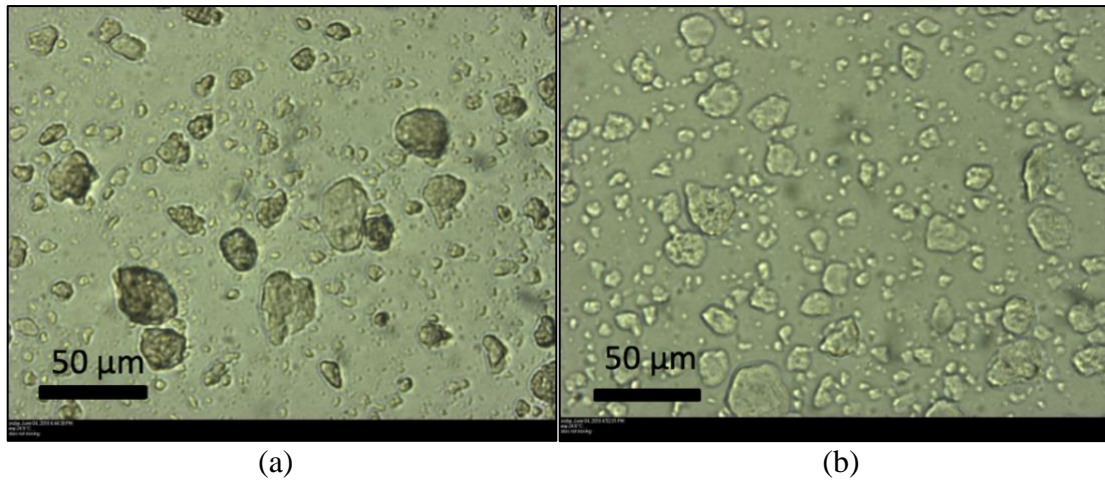


Figure 2.4 Microphotographs of the silica particles dispersed in water/glycerin mixture at 0.03 wt. %: (a) Silica 1; (b) Silica 3.

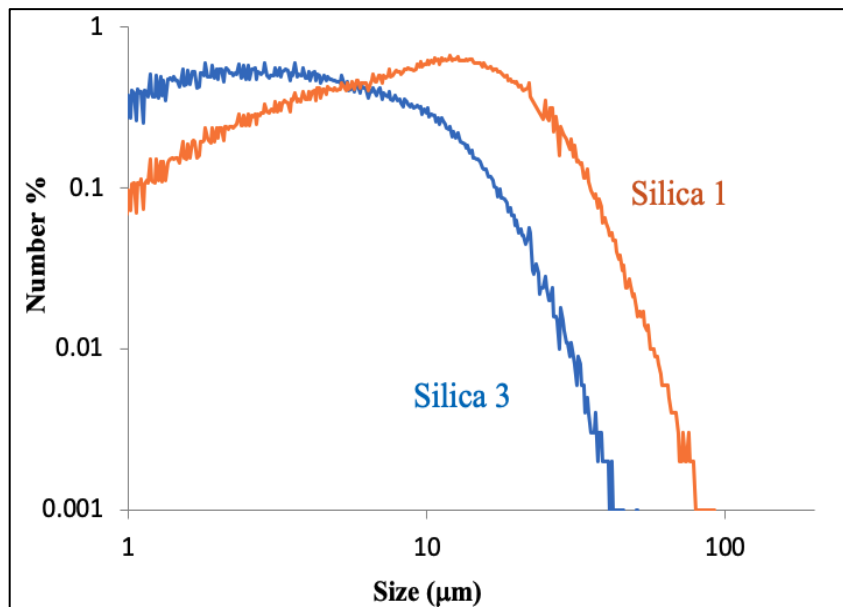


Figure 2.5 Number distribution of the Silica 1 and Silica 3 particles.

Table 2.1 Compositions of the Gels used in This Work

Component	Amount in <i>Gel 1</i> (g)	Amount in <i>Gel 2</i> (g)
Polyethylene Glycol 600	0.000	2.597
Xanthan Gum	0.476	0.519
Flavors and Sweeteners	0.000	3.442
Surfactants	0.000	2.750
Active Ingredients	0.000	2.797
Humectant (either Glycerin or Sorbitol, but not both in any formulation)	Varied in each experiment	Varied in each experiment
Water to 100 g	Q.S.	Q.S.
Total	100.000	100.000

Table 2.2 Compositions of the Formulations used in This Work

Component	Amount in <i>Formulation 1</i> (g)	Amount in <i>Formulation 2</i> (g)	Amount in <i>Formulation 3</i> (g)
Gel 1	84.000	-	-
Gel 2	-	77.000	84.000
Silica 1	8.000	-	8.000
Silica 2	-	15.000	-
Silica 3	8.000	8.000	8.000
Total	100.000	100.000	100.000

2.3.3 Methods

Solutions of all soluble components (the above-mentioned “gel”) were prepared using different amounts of humectant in either water/glycerin or water/sorbitol mixtures, utilized here as liquid bases. All gel components were homogenized in the Whip Mix WPM2 mixer. When making gels, all ingredients (including actives, flavors, sweeteners, and surfactants in the case of *Gel 2*), as well as the other components, were directly compounded in the Whip Mix mixer. Then, the gel was deaerated by centrifugation and its refractive index was measured with the refractometer. The silica particles were then added to the gel and compounded using the same mixer to make a final formulation with the desired humectant concentration. Only the type and concentration of the humectant were varied in the gels and hence in the formulations, as reported in Table 2.2. Once the silica particles were fully dispersed in the gel, the complete formulation was deaerated and a sample was collected in order to measure its turbidity and light transmittance. First, the sample was placed inside a Hach-2100Q portable turbidimeter and the turbidity measurement was taken and reported in NTU units. Then, the sample was placed in a round measurement cell and inserted in the Turbiscan apparatus where point-by-point values of transmittance were obtained on multiple cross-sections at different vertical positions in each cell. Only the maximum transmittance was recorded thus minimizing the effects of small air bubbles still remaining in the sample even after centrifugation.

All experiments were performed in triplicates by taking three different samples of the same gel or formulation and independently measuring the refractive index, transmittance, and turbidity values. In order to qualitatively evaluate the transparency of the most commercially relevant formulation (*Formulation 2*), vials containing different

concentrations of glycerin as the humectant in *Formulation 2* were placed against a colored pink background and visually inspected to detect the vial with the highest level of transparency. In addition, identical lines of text were printed on a sheet of paper and the formulations were extruded on them with a syringe to visually detect the one that resulted in the most legible text behind it.

2.4 Results

Experiments were conducted with different concentrations of humectants, and, as a result, different refractive indexes of the gel in order to maximize light transmittance and minimize turbidity of the formulations containing silica, with the ultimate objective of manufacturing optimally transparent products, such as toothpaste, and, at the same time, obtaining the effective refractive indexes of the silica particles used in each case to be then utilized for other similar future applications and products.

In this section, the results of all experiments are presented. The error bars in each figure represent the standard deviations of each set of triplicate experiments. The cumulative average coefficients of variation CoV ($\text{CoV} = \text{Standard Deviation} / \text{Mean}$) of all refractive index measurements, light transmittance measurements, and turbidity measurements in all experiments, calculated as the average of all CoV's for all triplicate experiments, were found to be 0.0026, 0.0198 and 0.0064, respectively, indicating a high degree of reproducibility.

2.4.1 Results of Refractive Index-Matching Experiments

Figure 2.6 shows the transmittance and turbidity of *Formulation 1* as a function of the humectant fraction in the corresponding gel (*Gel 1*). Clearly, both the transmittance and

turbidity of the formulations were very different depending on the humectant used in the gel. Nonetheless, shape of the curves was similar, i.e., transmittance was maximized and turbidity minimized at the same fraction of humectants (61.3% for sorbitol and 78.1% for glycerin) which may be thought of as representing the optimum humectant level for these formulations from the point of view of their transparency.

Re-plotting the same transparency and turbidity data against the refractive index of the two versions of *Formulation 1* (Figure 2.7) resulted in both curves becoming superimposed on each other. Thus, the optimum transparency of *Formulation 1* was achieved at the refractive index of the corresponding gel, i.e., 1.4415 for sorbitol and 1.4408 for glycerin, i.e., which, when taking the average, is 1.4412 regardless of which humectant was used.

Similar plots were generated for *Formulation 2* (Figures 2.8 and 2.9). As one can see, when compared to *Formulation 1*, the optimum transparency this time was achieved at lower humectant fractions, i.e., 57.1% for sorbitol and 74.9% for glycerin). Nonetheless, as in the case of *Formulation 1*, re-plotting the data against the refractive index of the corresponding gel resulted in the curves from Figure 2.8 becoming superimposed on each other (see Figure 2.9). The optimum transparency was achieved for formulations with a refractive index of about 1.4592 (i.e., 1.4598 for sorbitol and 1.4586 for glycerin). This value is higher than that reported above for *Formulation 1*.

To investigate this difference, additional experiments were conducted with the abovementioned non-commercial formulation (*Formulation 3*) containing *Gel 2* plus the same amount and type of silica as *Formulation 1*. Only glycerin was used as a humectant in these additional experiments. The results are presented in Figures 2.10 and 2.11.

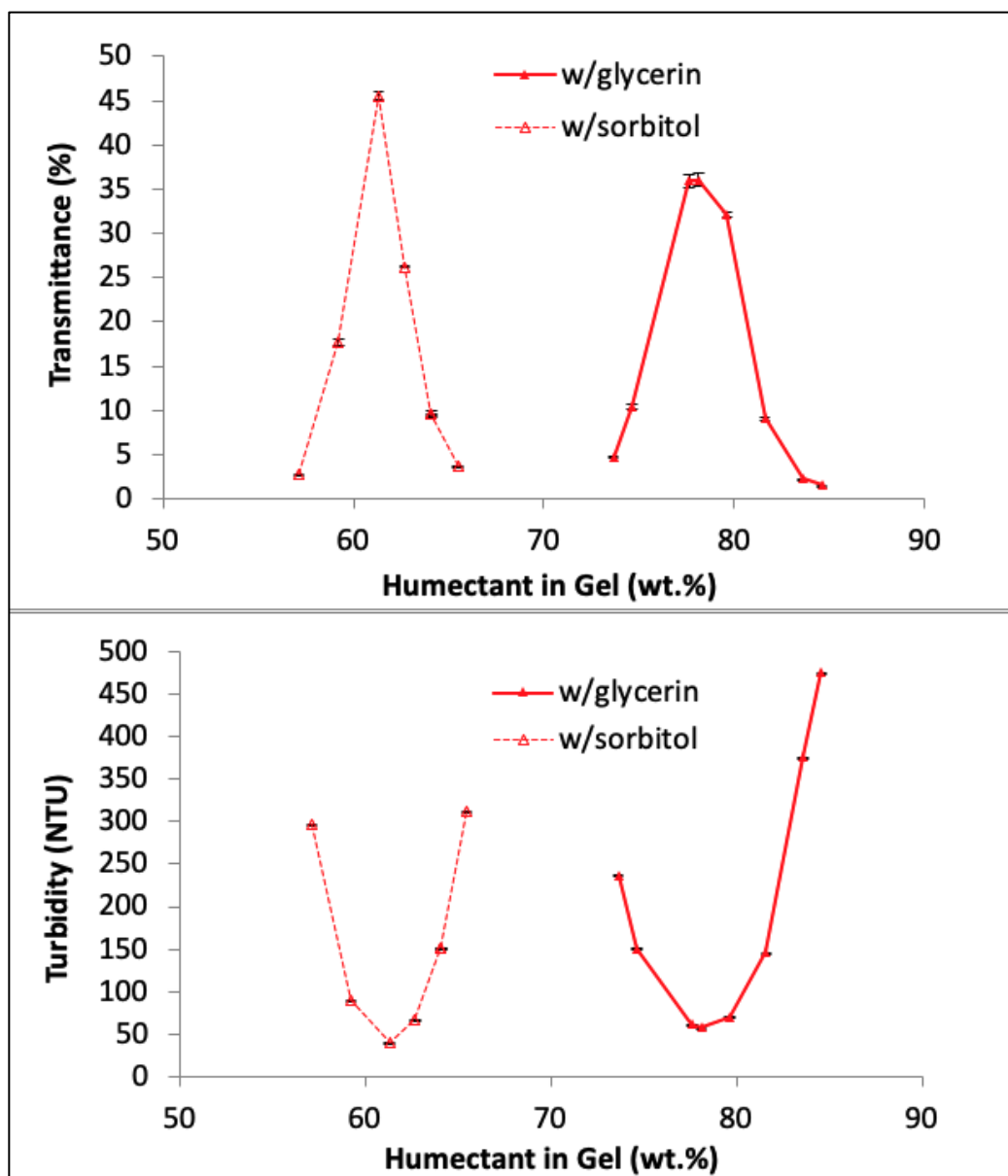


Figure 2.6 Transmittance (top panel) and turbidity (bottom panel) of *Formulation 1* as a function of the humectant fraction in the corresponding gel (*Gel 1*).

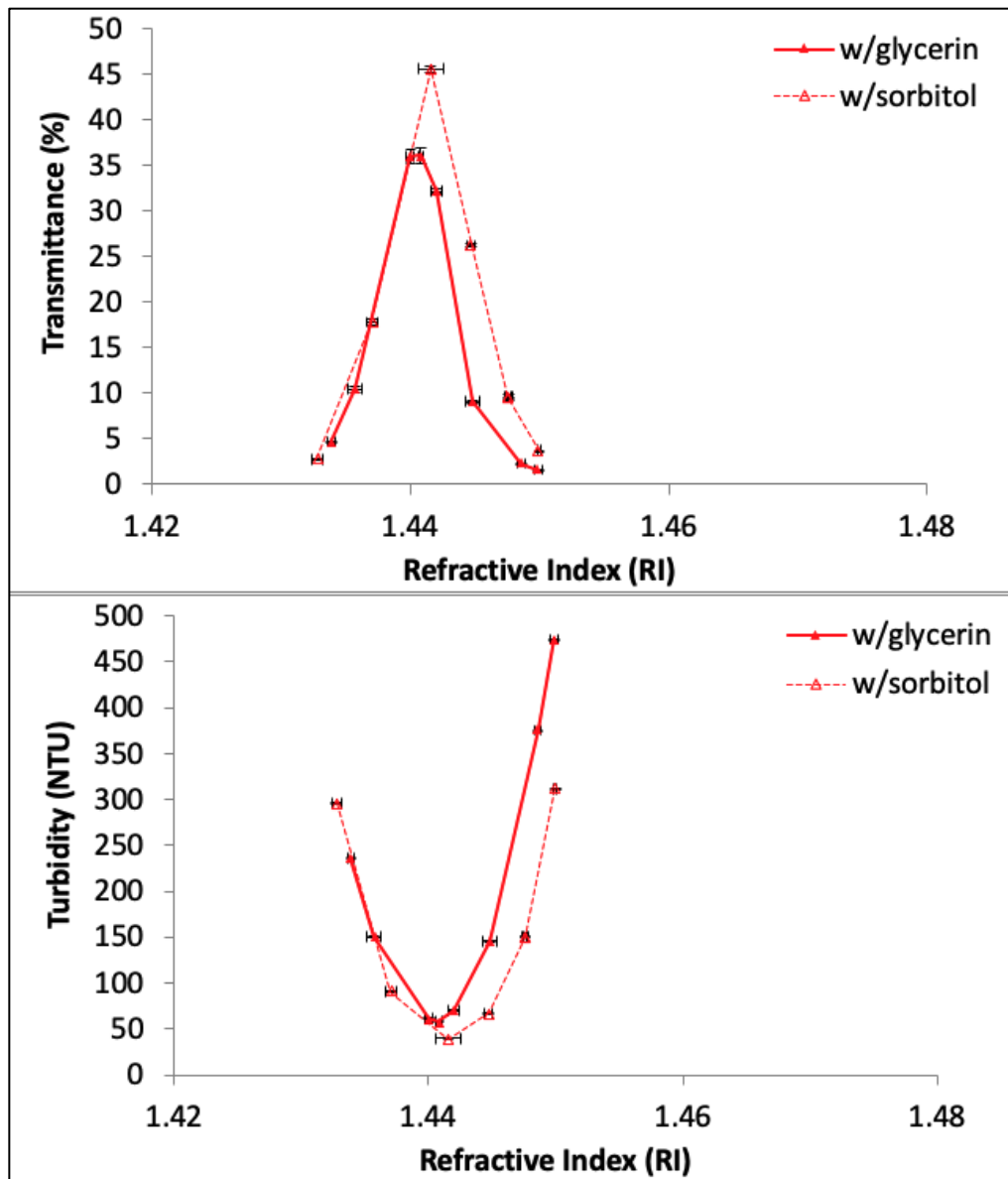


Figure 2.7 Transmittance (top panel) and turbidity (bottom panel) of *Formulation 1* as a function of the refractive index of different versions of the corresponding gel (*Gel 1*) for different humectant fractions.

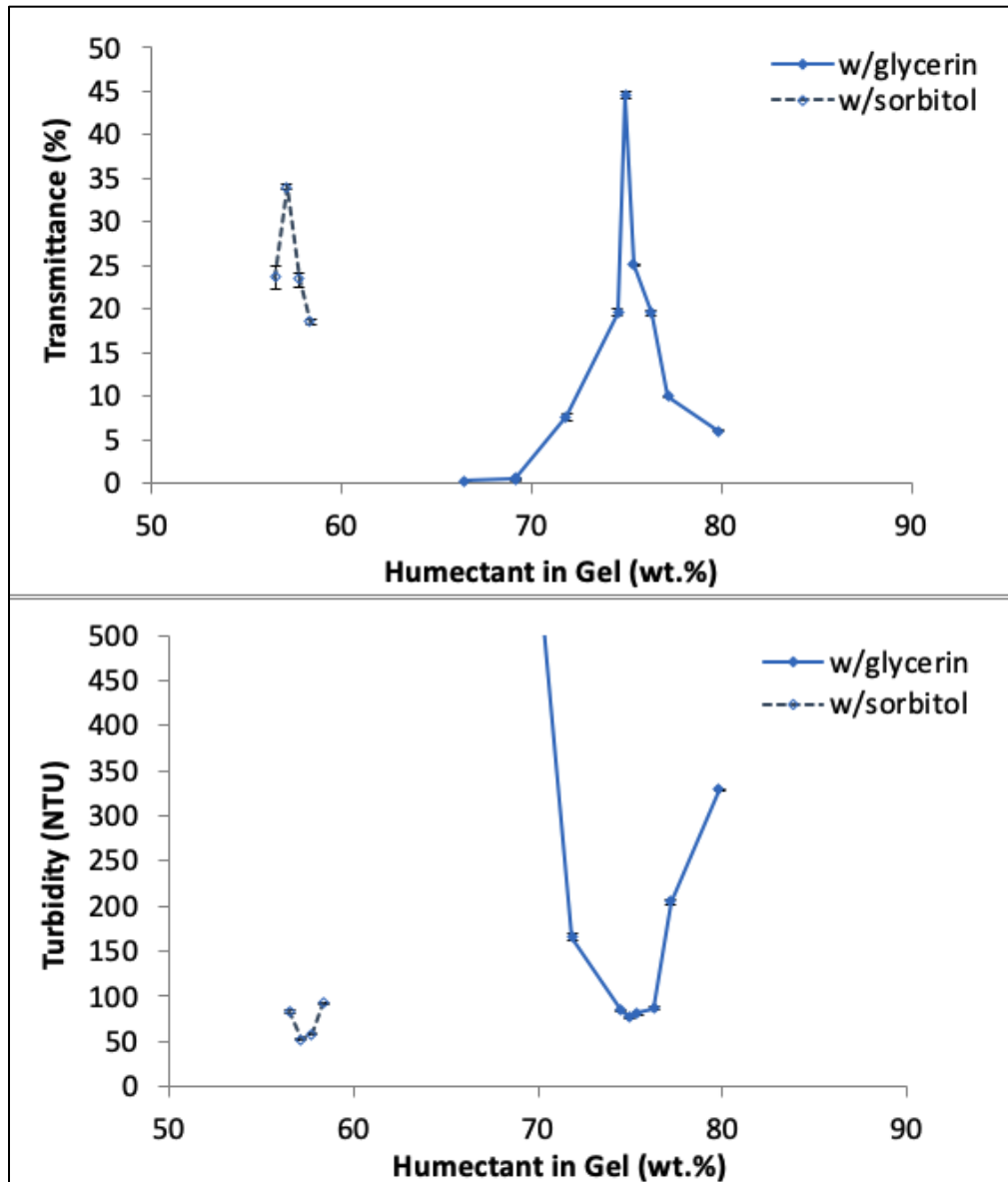


Figure 2.8 Transmittance (top panel) and turbidity (bottom panel) of *Formulation 2* as a function of the humectant fraction in the corresponding gel (*Gel 2*).

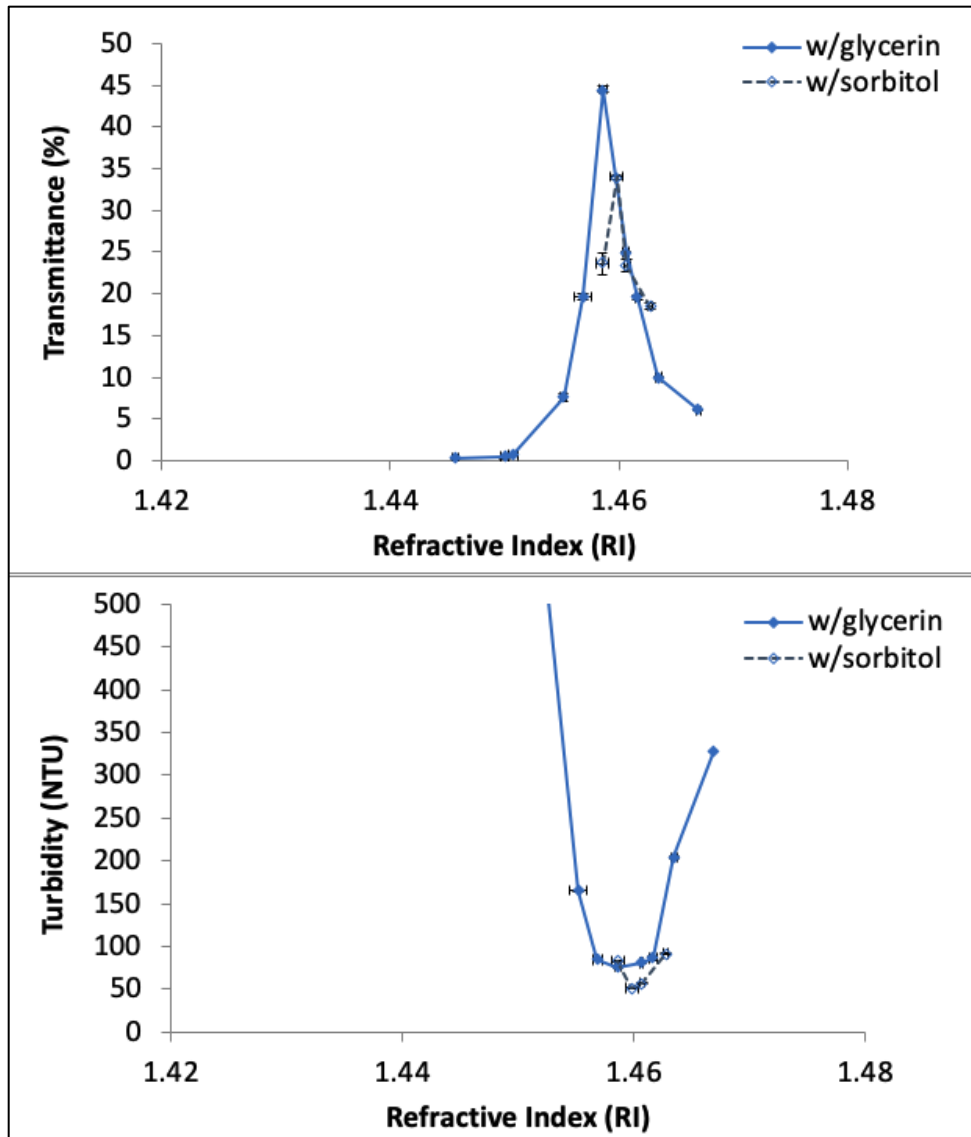


Figure 2.9 Transmittance (top panel) and turbidity (bottom panel) of *Formulation 2* as a function of the refractive index of different versions of the corresponding gel (*Gel 2*) for different humectant fractions.

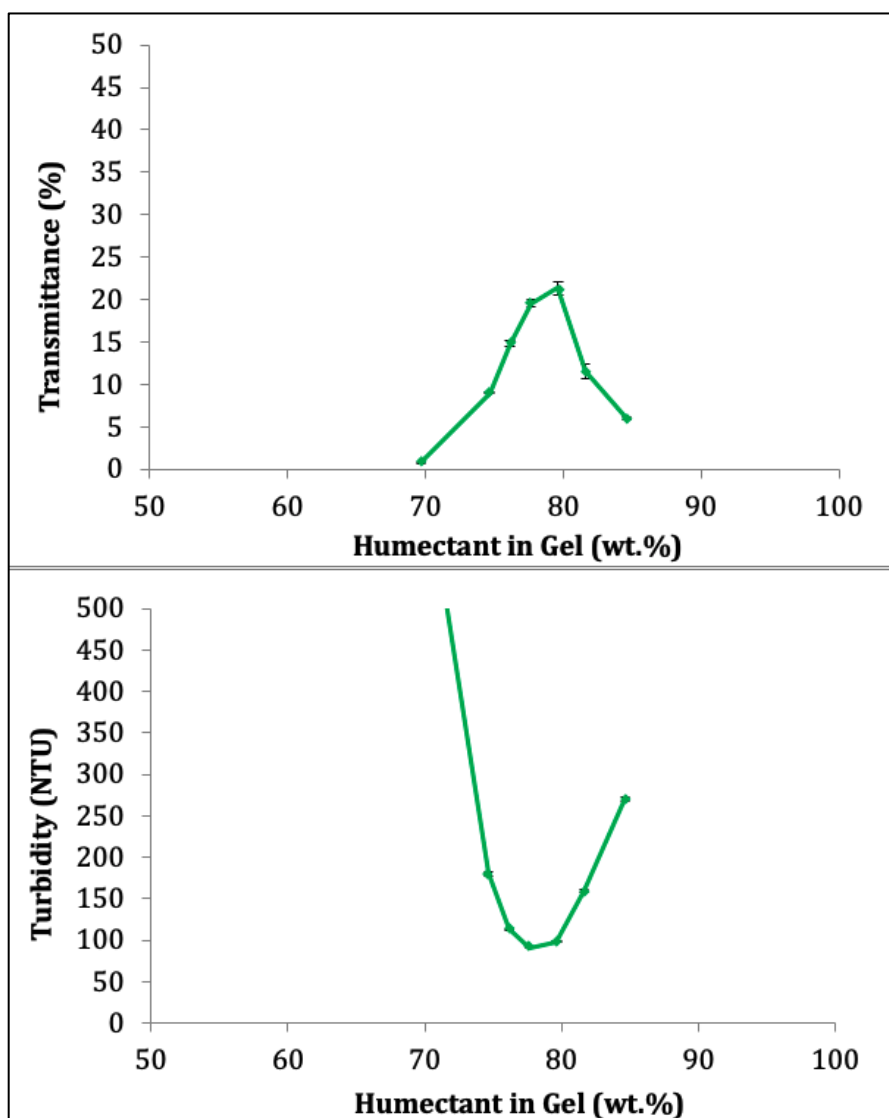


Figure 2.10 Transmittance (top panel) and turbidity (bottom panel) of *Formulation 3* as a function of the humectant (glycerin) fraction in their corresponding gel (*Gel 2*).

The highest transmittance values and the lowest turbidities were achieved when similar concentrations of glycerin were used in both formulations (~78-79%; Figure 10). However, it was found that the highest transmittance value was reached for a slightly higher refractive index value (RI=1.451) when using *Gel 2* (Figure 2.11) than when *Gel 1* was used (RI=1.4408; Figure 2.7), although the silica concentration was identical in both cases.

In addition, the actual value of the transmittance was lower for *Formulation 3* compared to *Formulation 1*, indicating that the dissolved components of *Gel 2* (polyethylene glycol, surfactants, flavors, sweeteners, and active ingredients) contribute to making *Gel 2* less transparent.

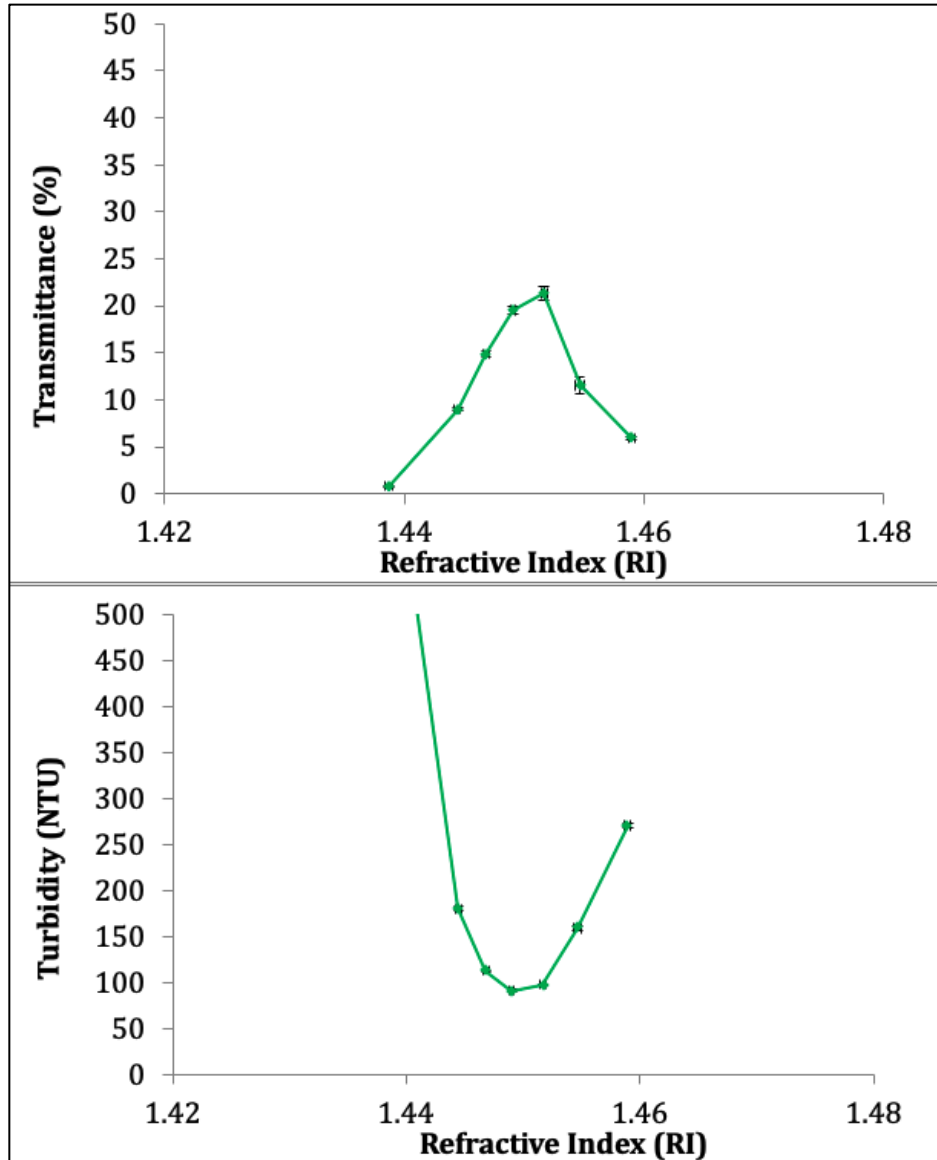


Figure 2.11 Transmittance (top panel) and turbidity (bottom panel) of *Formulation 3* as a function of the refractive index of different versions of their corresponding gel (*Gel 2*) with different humectant (glycerin) fractions.

2.4.2 Results of Visual Inspection of Formulations

Figure 2.12 shows the visual results for three different versions of *Formulation 2* with different humectant fractions, i.e., 79.8% glycerin (328 NTU), 74.9% glycerin (76 NTU), and 69.2% glycerin (846 NTU), from left to right in Figure 2.12(a) and from top to bottom in Figure 2.12(b), respectively. Figure 2.12(a) shows a photograph of those vials placed in front of a common background. Visually, one can see that the middle vial, containing 74.9% glycerin was the most transparent. Figure 2.12(b) shows a photograph of three lines of text onto which the same versions of *Formulation 2* were extruded with a syringe. As one can see, the letters are most clearly visible for the sample in the middle, i.e., the formulation with 74.9% glycerin once again, which is the formulation in correspondence of the peak in the top panel in Figure 2.8.

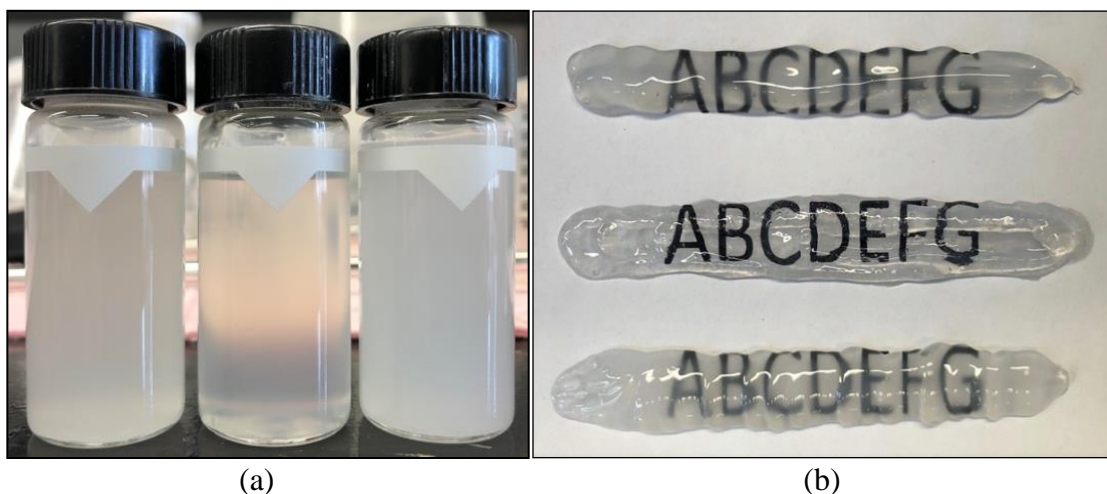


Figure 2.12 Visual results for *Formulation 2* with different glycerin fractions: (a) Vials with glycerin fractions equal to 79.8%, 74.9%, and 69.2%, from left to right, respectively; (b) lines of text onto which the same formulations were applied, from top to bottom, respectively.

2.5 Discussion

The results of this work show that it is possible to use the refractive index matching approach to manufacture commercial products, specifically toothpaste, that is optically transparent while containing complex mixtures of gels, a number of additives, and highly non-homogeneous combinations of commercial silica particles with different characteristics, size distribution, and shapes. The selection of the fluid is clearly critical to achieving refractive index matching of the selected solid particles, but in commercial products, the carrier fluids are chosen for reasons other than matching the refractive index of the solids. However, here we found that by varying the concentration of common humectants in aqueous solutions for toothpaste manufacturing, such as sorbitol and glycerin, the refractive index of the resulting gel would vary in a range that is compatible with the refractive index of silica reported in the literature (~1.44-1.45) [118, 122]. This, in turn, opened the possibility of fine-tuning the composition of the gel to match that of mixtures of the commercial silica particles used as abrasives in toothpaste, possibly resulting in transparent finished products.

The results were different for *Gel 2*. The presence of the other components (glycol, surfactants, sweeteners, surfactants, and active ingredients, as shown in Table 2.2) had a marked effect on the refractive index of this gel with respect to the baselines containing only humectant and water. However, even for this gel, the refractive index could be fine-tuned to match that of silica. In fact, when the silica particles were added to the gels the refractive index matching approach could be successfully used to maximize the transparency and minimize the turbidity of the resulting formulations by adjusting the concentration of humectant. In both formulations, the fraction of silica particles was

significant (16 wt. % and 23 wt. %, respectively).

In addition, the silica used in this work was commercial silica, and not silica made of monodispersed, high-purity, spherical, low-concentration particles as in a significant number of previous studies [119]. In addition, the solids were made of dispersions of two types of different commercial silica. The fact that the refractive index matching approach worked well in our systems, and that the final products with a high degree of transparency and low level of turbidity could be manufactured, is an indication that this approach is very robust and could be successfully used for a variety of industrial applications.

In addition to being able to obtain a product with the desired optical property, namely high transparency, we were able to use our experimental results to obtain the effective refractive indexes of the silica mixtures used here. Despite their different characteristics and morphology, the effective refractive indexes of the two silica mixtures were similar, as one can see in summarized in Table 2.3. This table also reports the values of effective refractive indexes of monodispersed, spherical, high-purity silica particles available in the literature. A comparison among all these results shows that all these values for the effective refractive indexes of silica are similar and on the order of 1.4505 (average value for all experiments in our work), which, with hindsight, could have been anticipated at least for the case of pure silica, but which was somewhat unexpected for commercial silica of different size, morphology and, possibly, impurity profiles.

This observation further reinforces our previous statement about the general applicability of this approach to different commercial products in the personal care product industry, and toothpaste in particular, since other commercial silica products, even from different suppliers, can be expected to have effective refractive indexes similar to the

average value reported in Table 2.3.

Table 2.3 The Effective Refractive Index of Silica Particles

Source	Effective Refractive Index of Silica Particles
This Work (<i>Formulation 1</i> with Sorbitol)	1.4415
This Work (<i>Formulation 1</i> with Glycerin)	1.4408
This Work (<i>Formulation 2</i> with Sorbitol)	1.4598
This Work (<i>Formulation 2</i> with Glycerin)	1.4586
This Work (<i>Formulation 3</i> with Glycerin)	1.4516
Average for This Work	1.4505
Ojeda-Mendoza et al.	1.4450
Philipse et al.	1.4547
Tan et al.	1.4580
Brixner , B.	1.4518
Average from the Literature	1.4524

2.6 Conclusions

The objective of this work was to determine whether specific toothpaste formulations could be made transparent by fine-tuning the composition of some of their basic constituents. This was achieved using the refractive index matching approach, which additionally resulted in the determination of the effective refractive indexes of the silica particles. All commercial silica particles tested here had similar effective refractive indexes irrespective of their supplier, particle size distribution, and morphology. This has important consequences for the applicability of this approach to optimize future formulations incorporating different additives and active ingredients in the primary liquid gels and/or silica particles with different specific morphologies.

CHAPTER 3

RESIDUAL HEEL VOLUME DURING THE PRESSURE-DRIVEN DISCHARGE OF COMPLEX FLUIDS FROM DISPENSING BOTTLES

3.1 Abstract

The discharge of complex fluids from consumer bottles containing liquid soaps, creams, lotions, and others, typically results in *heel* formation, i.e., the ultimate residual amount of fluid left the container. Here, we investigated the fluid rheology effect on heel formation in a commercial hand pump bottle containing different complex fluids and including humectants, gels, and pastes. CFD was used to simulate the flow of fluids whose rheology was based on the Carreau equation, resulting in the prediction of the heel volume. These results were validated using weight measurements to quantify the volume of fluid left in the container and, separately, with an imaging method based on the use of PIV. All these results were in good agreement. The effective yield stress σ_0 at a predefined level was found to be the critical parameter to predict the heel volume.

3.2 Introduction

Complex liquid discharge from industrial vessels, pipes, or other types of containers is a complex process, which, if not characterized properly, can result in slow discharge rates, reduced finished product/packaging quality, and the presence of residual fluid in the original container, often referred to as *heel*, after the discharge process is completed [25, 40, 132]. The discharge topic has received significant attention for Newtonian fluids of various viscosities [11-17]. Nevertheless, a much more limited amount of work has been conducted on the discharge of complex non-Newtonian fluids from vessels of different diameters through orifices of different shapes [17, 29, 30], and through pipes [18, 31, 32, 34, 35], as comprehensively reviewed in a recent article [132].

The current state of the art shows that the discharge process is significantly attributable to the rheology of the complex fluids [132]. Most of the previous work was focused on the characterization of the efflux of complex fluids *during* their discharge process. However, the determination of the fluid residue in the container *after* the discharge process is completed, i.e., the quantification of the residual *heel*, has received much less attention. A heel can be expected to occur in any type of container (e.g., a tank, bottle, pump, pipe, or tube) if the fluid rheology is complex and yield stress is present. The formation of a heel is of significant importance industrially since it can result in material loss, container fouling, product cross-contamination, and other undesired effects [132].

An optimal discharge process would be one that occurs rapidly and results in a minimal residual heel. Nonetheless, this is rarely the case with highly viscous and rheologically complex fluids. Furthermore, and to the best of our knowledge, we are only aware of one study specifically conducted on this topic, which was limited to the study of

xanthan gum and CMC gels discharged from an industrial tank [40]. Clearly, there is a significant gap in our ability to predict heel in general and especially for complex fluids, such as soaps, creams, and pastes, dispensed from commercial consumer dispensers.

Hence, the current situation still requires further research on the heel formation in consumer containers with the ultimate objective of gaining a better understanding of how the container geometry, the complex fluid rheology, and the modality through which the fluid is removed from the container, (e.g., with a hand pump creating a suction pressure discharging the fluid at a given velocity) can affect the formation of the heel. Such knowledge could lead to improved designs of the containers and discharge devices for specific fluid rheologies, which could result in the minimization of the heel.

Among the many types of consumer containers available, bottles provided with hand pumps are highly relevant since they are commonly used for a variety of products such as liquid hand soaps, hand creams, body lotions, body wash, hair products, and many others. Additionally, unlike all the discharge studies available in the literature, hand pump bottles require the fluid to be discharged by flowing *upwards*, which, to the best of our knowledge, has not been studied yet. Therefore, which geometric, mechanical, and rheological properties dominate the discharge of complex fluids from these types of bottles, and the formation of the heel still remains to be investigated.

In order to quantify the heel formation in detail, the utilization of Computational Fluid Dynamics (CFD), and the determination of velocity distribution using Particle Image Velocimetry (PIV) can be very useful. These techniques have been proven to be highly effective to study complex systems, including those in which the fluid is highly turbulent [109]. Nevertheless, these techniques have not yet been used for heel investigations in

consumer bottles.

Therefore, the objective of this work was to quantify the effect of fluid rheology on heel formation in a commercial dispensing bottle using both PIV and CFD. Accordingly, we studied the discharge of fluids with different rheologies, such as humectants, gels, and pastes [7, 8, 132], using a continuous pumping system mimicking the differential pressure applied by a typical commercial hand pump. This was accomplished using CFD to simulate the flow of fluids whose rheology was based on the Carreau equation, ultimately resulting in the prediction of the heel volume (V_{H-CFD}). The Carreau parameters were extracted from rotational rheology experiments. The CFD predictions were then validated using experimental methods relying on weight measurements of the fluid removed from the container and hence the quantification of the volume of fluid left in the container, i.e., the heel ($V_{H-Weight}$) and, separately, with an imaging method based on the use of PIV to determine the heel volume (V_{H-PIV}). The flow index, n , the effective yield stress, σ_0 , and the low shear viscosity, η_0 , of the fluid can all affect the formation of the heel. However, we found that fluids with high η_0 , and high σ_0 resulted in significantly larger heel volumes due to the fact that the fluid does not move in zones where low shear stress is present, i.e., in the region away from the fluid collection point at the end of the dip tube in the bottle.

3.3 Experimental Equipment, Material, and Methods

3.3.1 Experimental Equipment

Mixer. A Whip Mix WPM2 mixer (Whip Mix Corp., Louisville, KY) was used to prepare the complex fluids studied in this work. The details of this mixer were reported in Chapter 2, and will not be repeated here.

Centrifuge. An Eppendorf Centrifuge 5804 (Thermo Fisher Scientific, Waltham, MA) was used to centrifuge the samples in order to remove the remaining air bubbles, which can cause light reflections. A low rotational speed (typically 3000 rpm for the gels, but up to 5000 rpm for pastes) was used to ensure that the tracer particles used in the PIV experiments (as described below) did not sediment because of the centrifugal force. In all cases, the samples were centrifuged for 3 minutes.

Rheometer. Rheological measurements were performed with a DHR-3 rheometer (TA Instruments, Delaware, USA), shown in Figure 3.1a, with two different Couette-type geometries, i.e., the vane-in-cup geometry and concentric cylinder (DIN) geometry (Figure 3.1b and Figure 3.1c, respectively).

For low and moderate shear measurements, a four-paddled vane of 15 mm diameter and 38 mm length was used in a 30 mm diameter cup (internal diameter-to-external diameter ratio=0.5), since this geometry is best suited to characterize the flow inception, as described before [37]. For high shear measurements, a narrow-gap, concentric cylinder geometry (DIN standard, with an internal diameter-to-external diameter ratio of 0.92) was used, since this geometry accurately describes the typical “pumping” conditions, as shown previously [25]. Here, we believe that why these two different geometries were used at different shear ranges deserves some detailed explanations. Firstly, it should be indicated that concentric geometries disturb the fluid while being immersed in it, as the fluid is being “squeezed”, and a large portion of the fluid penetrates the narrow gap, which already creates a shear that causes an immediate drop in viscosity of the fluid. The vane geometry, on the other hand, only “cuts” a relatively smaller portion of the fluid like a knife (with its thin paddles) while being immersed into the fluid, which, in turn, minimizes the fluid

disturbance, and provides more accurate rheological parameters, especially at flow inception conditions (i.e., at very low shear rates) [71, 133, 134]. Furthermore, concentric geometries may cause slip (unless a serrated one is used) that yields wrong rheological parameters, which is not the case when a vane geometry is used.

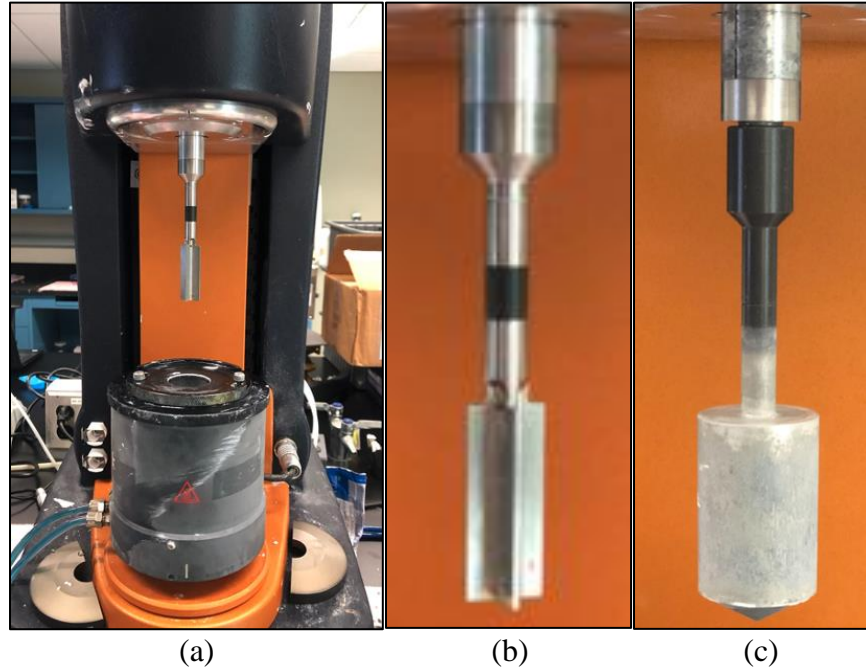


Figure 3.1 Rheological apparatuses used in this work: (a) DHR-3 rheometer (TA instruments, Delaware, USA); (b) vane-in-cup geometry; (c) concentric cylinder (DIN) geometry.

Particle Image Velocimetry System. The PIV system used in this work was identical to the one used in a previous study conducted by our research group [84]. The laser in this system was a New Wave Research Model Solo 120 15-HZ (Fremont, CA, USA) unit with a visible green laser light sheet emitted at 532 nm. In our experiments, the thickness of the laser light sheet was constant at 3 mm. A VCXU FlowSense digital camera (Dantec Dynamics, Denmark) provided with a red color filter was mounted on a traversing system in order to accurately align the system. Figure 3.2 shows the PIV experimental system,

and Figure 3.3 shows the diagram of the entire experimental setup. Additional details of the PIV system are provided elsewhere [84].

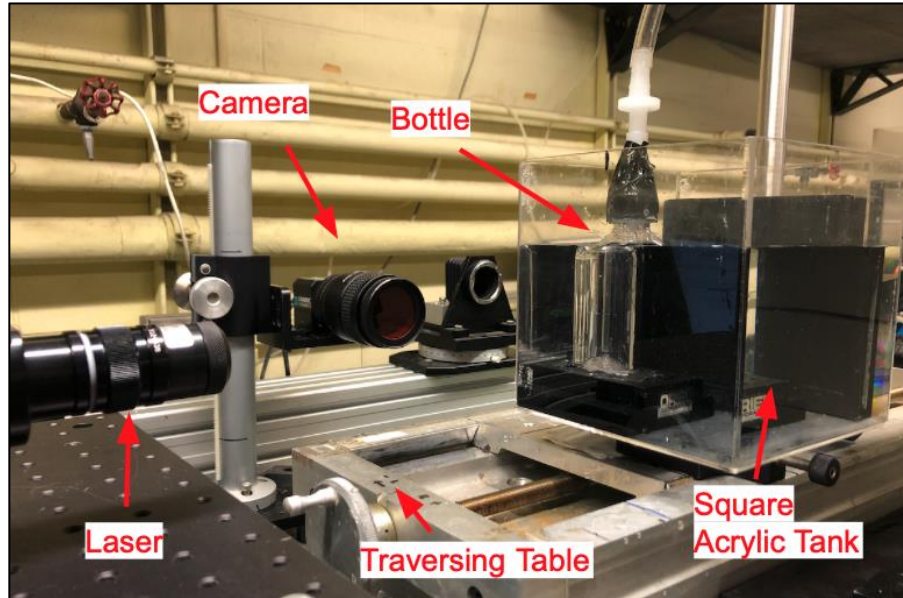


Figure 3.2 PIV experimental system.

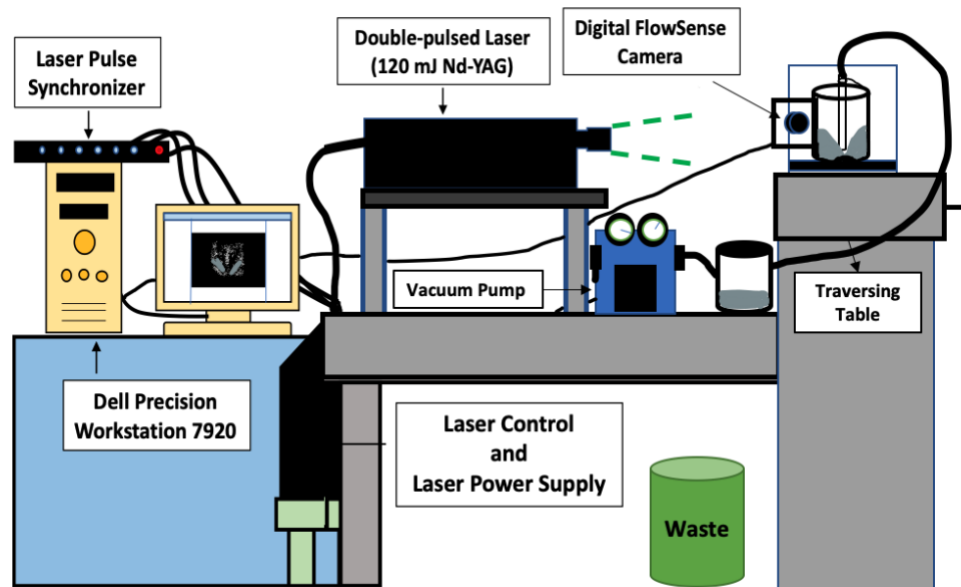


Figure 3.3 Diagram of PIV experimental system.

Test Bottle and Discharge System. A commercial lotion bottle (total height, $h_B=103$ mm; outer diameter, $D_B=45$ mm) was used in this work. A typical bottle, shown in Figure 3.4a, is equipped with a hand pump connected to a small dip tube inside the bottle (ID=5 mm, OD=6 mm) to manually dispense the bottle content. However, here the hand pump was not used. Instead, the bottle shown in Figure 3.4b was actually used in this work. In this bottle, the pumping mechanism of the pump was removed, and the dip tube was connected to a vacuum system that discharged the fluid out from the bottle and into an external container maintained at a constant negative pressure of about -0.14 bar (measured at the tube orifice), mimicking the approximate differential pressure that a hand-pump generates. More specifically, the spring and the piston chamber of the original hand pump were replaced with a tube fitting connected to a vacuum pump to provide continuous pumping. Additionally, the original translucent dip tube connected to the hand pump body was replaced with a transparent polycarbonate tube having the same length, inner diameter, and outer diameter as the original, so as to improve the quality of the PIV optical measurements. The same bottle was used in all experiments.

The bottle was secured with double-sided tape to a heavy black metal plate (Figure 3.4b) to ensure its stability during pumping. This assembly was then placed inside a small acrylic square tank and mounted in front of the PIV system. The corners of the metal plate were matched up to the corners of the square tank so as to ensure that the bottle was correctly placed at the same location with respect to the PIV in each experiment. The small square tank was filled with deionized water so as to minimize the refractive effects at the curved surface of the bottle and tube wall during the PIV measurements.

Most commercial bottles have a curved bottom, often referred to as a “bump”,

“dimple” or “kick-up” in the plastic industry, although its more common name is a “punt,” a term also used in the wine industry [135]. The presence of this bump ensures the mechanical stability of the bottle and increases its resistance to impact or internal pressure. The bottle used here also had a bump with a peak height of 5 mm from the bottom rim of the bottle. The lower end of the dip tube was 1.75 mm above the bump.

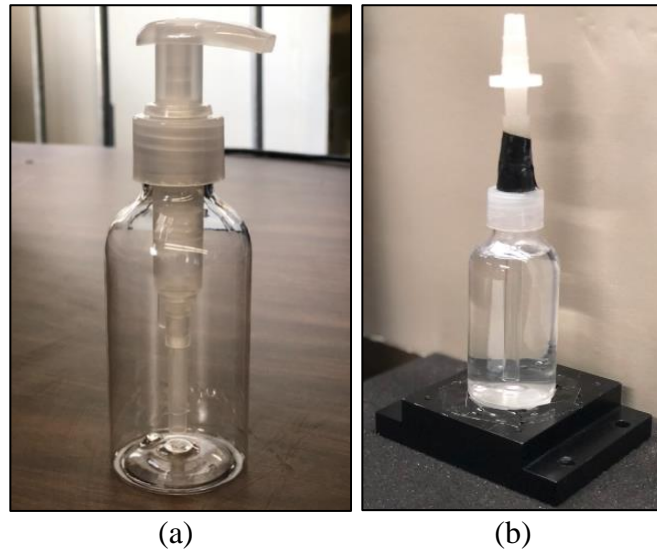


Figure 3.4 Typical commercial lotion bottle: (a) original bottle with hand pump; (b) bottle actually used in this work with the modified hand pump mechanism removed for continuous discharging of its content.

3.3.2 Materials

Tracer Particles. Fluorescent red polyethylene particles (Cospheric, CA, USA) with a particle size range of 10-45 μm and a density of 0.995 g/cm^3 were used as tracers in the PIV experiment. Since the red color filter mounted on the camera only allowed light with wavelengths at or above that of red color, the camera could only detect the signals from the tracer particles, thus removing the light reflections of the green laser light from the tube and the bottle that could cause interference. Polyoxyethylenesorbitan monooleate (Tween 80, Sigma-Aldrich 9005-65-6) was used as a surfactant in order to wet the tracer particles.

A stock suspension of the tracer particles was prepared by adding about 1 g of tracer particles into 100 mL deionized water with Tween 80 (about 1-2 droplets in 100 mL of stock suspension). The tracer suspension was stirred using a magnetic stirrer at 100 rpm for about a minute before being added to the fluids to be tested.

Fluids. In order to study the discharge of fluids with a wide range of complexity, two liquid humectants (sorbitol and glycerin, both Newtonian fluids), five gels (0.5 Xan, 1.0 Xan, 1.5 Xan, 2.5 Xan, and 15 Carbopol), and two pastes (11 Silica Paste, and 16 Silica Paste) were used in this work, as summarized in Table 3.1.

To prepare the xanthan gels, xanthan gum was first dissolved in glycerin using an IKA-WERKE overhead mixer (Ika-Works Inc, USA) after which about 10 mL of the stock tracer particle suspension was added. Then, make-up water was added and the mixture was transferred to the WhipMixer where complete homogenization with minimal air bubbles entrainment was achieved after 4 minutes of mixing under vacuum. In addition to xanthan gum, Carbopol was also used in our study as another thickening agent. The type of Carbopol used here was Acrylates Crosspolymer-4 (Carbopol® Aqua SF-2, Lubrizol, USA). To prepare the Carbopol gel with the overhead mixer, the Carbopol was added to the water under continuous agitation, and liquid NaOH was added dropwise into the solution until the point the fluid became transparent, indicating complete neutralization of Carbopol. It should be noted that while Carbopol is typically used in industrial applications at 3-5 wt.%, we deliberately prepared a more highly concentrated solution to expand the range of rheological properties of the fluids that we examined in our work and take advantage of the fact that this formulation was both viscous and transparent. In addition, it is experimentally very difficult to prepare and work with xanthan gum polymer solutions

having a xanthan concentration higher than 4-5 wt.%. For this reason, we preferred to use a Carbopol solution to explore the behavior of a high viscosity fluid.

Two model pastes (named here “11 Silica Paste”, and “16 Silica Paste” for simplicity) were prepared using the same procedure for the xanthan gum gels. However, in this case, the thickening silica (Silica 3, previously used in [8]) was added prior to the WhipMixer stage, after which the WhipMixer homogeneously dispersed the silica into the gel, thus forming a paste [7]. Additional details (manufacturer, number distributions) and other physical properties of this silica can also be found elsewhere [8]. The pastes were prepared considering the humectant-water ratio at which the refractive index of the liquid matched that of the suspended silica particles, thus maximizing optical transparency. Specifically, in both pastes, the glycerin concentration in the gel component (i.e., glycerin, water, and xanthan gum only) was 78 wt.%, which is the concentration required to optimize the optical transparency of such systems [8].

Table 3.1 Composition of the Fluids Experimentally and Computationally Studied in This Work

Fluid	Xanthan Gum (wt.%)	Carbopol (wt.%)	Thickening Silica (wt.%)	Sorbitol (wt.%)	Glycerin (wt.%)	Water (wt.%)	Density (g/cm ³)
Sorbitol	-	-	-	70	-	30	1.343
Glycerin	-	-	-	-	100	-	1.260
0.5 Xan	0.5	-	-	-	49.75	49.75	1.102
1.0 Xan	1.0	-	-	-	49.50	49.50	1.104
1.5 Xan	1.5	-	-	-	49.25	49.25	1.106
2.5 Xan	2.5	-	-	-	48.75	48.75	1.110
15 Carbopol	-	15	-	-	-	85	0.876
11 Silica Paste	0.39	-	11.53	-	69.14	18.94	1.331
16 Silica Paste	0.37	-	16.36	-	65.37	17.90	1.405

3.3.3 Methods

3.3.3.1 Rheological Characterization of the Fluids. Rheological measurements were performed on the DHR-3 rheometer (TA Instruments, Delaware, USA) operated with Trios software. All the measurements and data processing at low shear rates (below 10 sec^{-1}) were performed as described previously [40] and using the same tool, namely the vane-in-cup geometry [37]. As mentioned in that work, two types of tests were performed, i.e., creep tests at sufficiently low stresses so as to recover the low-shear viscosity plateau, and shear rate sweeps with shear rates ranging from 0.2 to 10 sec^{-1} . To account for the flow at higher shear rates, the narrow-gap concentric cylinder Couette geometry (DIN) was used, and the data were analyzed with the Trios software.

To parameterize the data, the Carreau equation [82] was used:

$$\eta = \frac{\eta_0 - \eta_\infty}{(1 + (\lambda\dot{\gamma})^2)^{(1-n)/2}} + \eta_\infty \quad (3.1)$$

with four fitting parameters: η_0 , η_∞ , λ and n . The fitting procedure was also the same as in previous work [40].

The use of the Carreau equation to parameterize the data in the context of the dispensing tests described above deserves some explanation. This model may seem inconsistent with the fact that at least some of the fluids tested are usually considered yield-stress fluids. However, one should keep in mind that the dispensing tests, by their very nature, are constrained to rather short periods of time during which the fluid is being evacuated from the bottle. In our case, depending on the fluid, it lasted from about 25 sec to 4.7 min, which can be easily estimated from the volumetric velocities listed below. The

apparent low-shear viscosity of these fluids under such conditions depends on the time of the test [136]. In fact, in a recent study conducted by Ahuja and Potanin (Figure 3 therein), it was shown that as the time of the applied stress lengthens, the low-shear viscosity (i.e., η_0 in Equation 3.1) increases while the stress at which viscosity drops decreases [9]. The latter may be referred to as the “effective yield stress”, not to be confused with the true yield stress which the fluid may or may not have. This effective yield stress by definition depends on the time during which the stress is applied and will approach the true yield stress as this time increases and the flow approaches a steady state. Potanin and Shapley (2021) have shown that thus defined effective yield stress may be a useful parameter to describe transient processes, such as discharge of strongly shear-thinning fluids from tanks, provided the stress time is chosen to be close to the characteristic time of that process. Here it is worthwhile to point out that the question of the *existence* of the true yield is not the subject of this work. We are fairly certain that some of the systems studied (e.g., Carbopol solutions), do have the true yield stress while others (e.g., most of Xanthan gum solutions) do not, and it could have been measured had the flow been allowed to reach the steady state. However, our goal was to develop a simple method applicable to the transient experiments (in our case- discharge from bottles) rather than to explore the steady state. A more sophisticated model may take into account the thixotropic behavior of the fluid so as to describe the changes in its rheology as it travels down the wall of the container, but, as our experiments show, the simpler approach based on the Carreau parameterization for CFD analysis may work just fine.

The parameters extracted by fitting the data were subsequently used in CFD simulations to predict the behavior of those fluids, as described below. In addition, CFD

simulations were also conducted using parameters mimicking the rheology of several imaginary model fluids to identify the rheological parameters that affect the heel the most, thereby extending the range of rheological profiles beyond those experimentally available.

3.3.3.2 Experimental Determination of the Average Velocity in the Dip Tube Using

PIV. The hydrodynamic characterization of the flow in the dip tube, and especially the velocity profile in the tube, is critical to correctly simulate the formation of the heel in the bottle. To accomplish this objective, the PIV approach was used to quantify the two-dimensional (2D) velocity distributions in the dip tube on the vertical plane across it. Then, the velocity values on a selected horizontal section inside the tube were used to calculate the flow rate out of the bottle and establish the velocity boundary conditions in the CFD simulations, as described below. Here, it should be clearly noted that unless one wants to study the flow inside the dip tube itself (e.g., to study the velocity profiles such as parabolic or plug flow that would be affected by the fluid rheology), the exact boundary conditions near the upper end of the tube would play a minor role in the hydrodynamics in the bottle. In fact, we have also tried using volumetric flow rate boundary conditions, which gave almost identical results.

Accordingly, the bottle was completely filled with a liquid, the vacuum pump was turned on, and PIV measurements were started. The vacuum pump continuously removed fluid from the bottle and discharged it to another empty container. PIV software (DynamicStudio 6.11.33) was utilized to collect and process the experimental data. The time difference between two laser pulses, Δt , was 1000 μs for low viscosity fluids (such as sorbitol, glycerin, and 0.5 Xan) and 3000 μs for higher viscosity fluids. Only for 16 Silica paste, Δt equal to 5000 μs was used to capture the slower flow. The PIV collected image

pairs at a frequency of 8 Hz. The size of the interrogation windows was 32×32 pixels.

For each pair of images in each interrogation window, the background noise was subtracted to remove most of the bright areas caused by few residual reflections from the bottle and tube, and then analyzed using the adaptive PIV function to determine the spatial displacement of the particles and hence the liquid velocities. In each case, many image pairs were taken, i.e., at least 150-200 images for low viscosity fluids, but up to 400 for higher viscosity fluids as the discharge for such fluids progresses slowly whereas for lower viscosity fluids the discharge occurs more rapidly. Axial time-averaged velocities at each point on the dip tube diameter were extracted.

The velocity values on the horizontal plane 10 mm above the orifice of the tube (to avoid the entrance effect) were averaged and used as the velocity boundary condition in the CFD simulations. An example of the typical velocity distribution output obtained by PIV using the 0.5 Xan fluid is shown in Figure 3.5. The white line indicates the horizontal plane 10 mm above the orifice. The average velocities obtained with this approach for each fluid are presented in Table 3.2. For the imaginary model fluids, an average velocity of 5 mm/s was used.

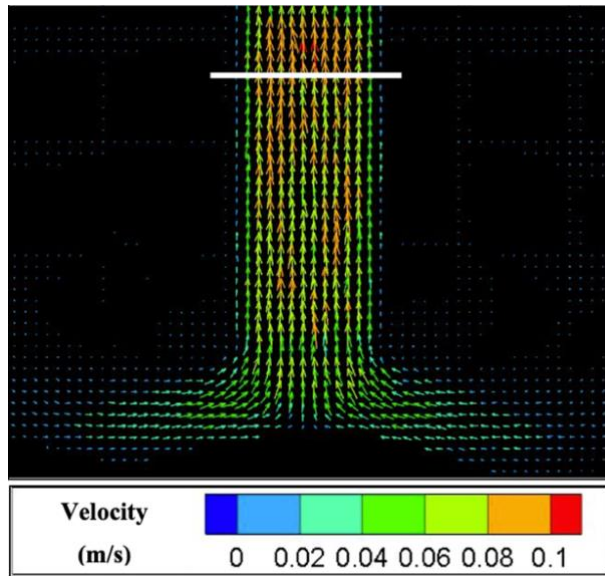


Figure 3.5 Typical PIV output: Velocity distributions for 0.5 Xan while being sucked out from the bottle. The white line shows the horizontal plane 10 mm above the orifice, as described in the text.

Table 3.2 Average Velocities on the Horizontal Cross-section 10 mm Above the Orifice of the Tube, as Determined with PIV

Fluids	Sorb.	Gly.	0.5 Xan	1.0 Xan	1.5 Xan	2.5 Xan	15 Carbopol	11 Silica Paste	16 Silica Paste
Average Velocity (mm/s)	69.6	8.3	67.7	18.1	7.6	7.0	3.3	4.3	1.1
Standard Deviation	4.0	2.0	1.7	0.5	0.1	1.2	0.2	0.4	0.2

3.3.3.3 Computational Determination of Heel Volume Using CFD (V_{H-CFD}). The CFD approach consists of discretizing and solving the partial differential equations (PDEs) describing the appropriate conservation equations that describe the flow [137]. The mass conservation equation is given by:

$$\nabla \cdot \mathbf{u} = 0 \quad (3.2)$$

and the Cauchy momentum conservation equation for incompressible fluid is given by:

$$\frac{D\mathbf{u}}{Dt} = -\frac{1}{\rho}\nabla \cdot \boldsymbol{\sigma} + \mathbf{g} \quad (3.3)$$

Equation (3.3) becomes the Navier-Stokes equations for fluids with constant viscosity. For non-Newtonian fluids, one has to solve Equation (3.3) along with a constitutive equation describing the rheology of the fluid since the viscosity is not constant. As mentioned above, we used the Carreau equation to parameterize the viscosity curve (Equation (3.1)).

In this work, all numerical simulations were conducted using a commercial software package, ANSYS Fluent v2021-R2, running on a Dell Precision T5810 Workstation [84]. The geometric model of the bottle was generated in the preprocessor by ANSYS SpaceClaim software. Only half of the bottom portion (up to 20 mm height from the bottom) of the bottle was modeled axisymmetrically in 2D, as shown in Figure 3.6. A 2D axisymmetric model represents a slice of the actual three-dimensional model which, if revolved around the y-axis of the reference Cartesian coordinate system, would give the original three-dimensional structure. The main advantage of 2D axisymmetric modeling is that since the number of cells is much smaller than the number of cells that would have been created in 3D, the computational time is significantly reduced. Furthermore, the geometry is much easier to create and easier to manipulate. For instance, the user does not have to rotate the geometry or hide/show the faces to see all the zones of the geometry.

Two zones were created within the geometry and then meshed: (1) the “dip tube” zone having quadrilateral mesh that becomes finer in the entrance region, and (2) the “bottle” zone having triangular mesh, which corresponds to the total geometry minus the

tube, again, becoming finer in the tube entrance region. The resulting grids contained 734 cells, 1229 faces, and 496 nodes. The grid was finer in the regions near the tube entrance so as to accurately capture the moment at which the air goes in the tube, stops the discharge, and results in a heel. The simulations were conducted with increasingly finer grid mesh sizes until the computed velocities were grid-independent.

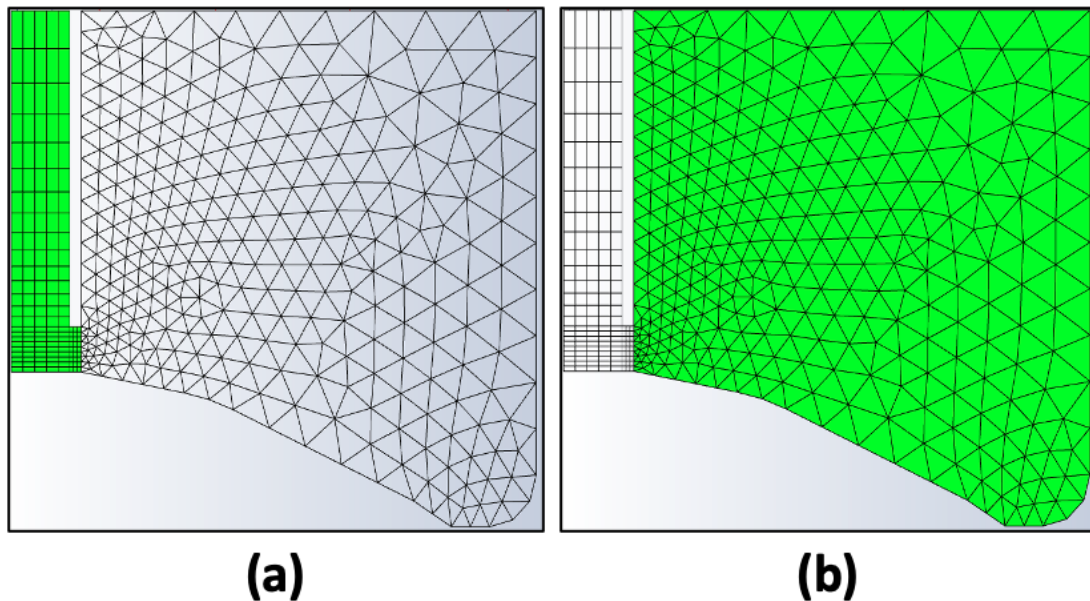


Figure 3.6 CFD geometry and mesh showing both computational zones (shown in green color): (a) “dip tube” zone; (b) “bottle” zone.

The quality of the computational mesh was always carefully considered since it can significantly affect the convergence of the simulation. For all the mesh elements, the maximum aspect ratio was 7.79, the minimum orthogonal quality was 0.16, and the equi-angle skewness was less than 0.76 for any individual cell, leading to a good mesh quality.

In the ANSYS Fluent module, the volume of fluid (VoF) model was used. The transient solver was selected in order to track the evolution of the fluid volume contained in the bottle until the point when the suction process stopped. “Air” and “liquid” were

defined as the two phases, where the “liquid” was parameterized in terms of the Carreau model. This means that the viscoelastic effects were neglected. Despite this major assumption, it was shown that the Carreau model accurately predicted the heel volume in industrial tanks, irrespective of the presence of any viscoelastic effects [40]. This was also the case in this work, as shown below.

The parameters of the Carreau equation for each fluid (all reported in the Results section), i.e., the low- and high- shear viscosities (η_0 and η_∞ , respectively), the flow index n , and the time constant, λ were entered in Fluent software. Other parameters of the model were as follows: surface tension of 0.07 N/m, air viscosity of $1.8 \cdot 10^{-5}$ Pa·s, and acceleration of gravity of 9.81 m/s^2 . The density values were varied in each experiment depending on the density of the fluid used (Table 3.1). A Pressure Implicit with Split Operator (PISO) scheme was used to solve the velocity-pressure coupling, which derives a pressure equation to iteratively and effectively solve the momentum equation, and is typical for transient simulations. Boundary conditions were set as no slip on the walls, and ambient pressure at the inlet at the upper boundary of the bottle zone (Figure 3.6b), while at the upper boundary of the tube (Figure 3.6a), an average upward velocity, obtained from the PIV measurements as described above, was used. Here, it is noteworthy to mention that the velocity in the tube could have also been calculated by using the generalized Hagen-Poiseuille equation (see Equation 8 in [25]), which enables the calculation of the volumetric flow rate of a fluid in a tube once the fluid rheological parameters, tube diameter, and length are known. Here, we have used experimental velocities since they had actually been measured using PIV.

In each simulation, 50,000 time steps were used with a fixed time step size of 0.005

seconds. In each time step, the maximum iteration number was 20. It was found that times smaller than 0.005 seconds did not result in any significant difference in the results. Therefore, to save computational time, 0.005 seconds were used as the time step. For all the rheologically different fluids studied here, 50,000 time steps were enough to capture the entire process, including the moment at which the heel volume dropped below the lower end of the dip tube end and air started entering the dip tube.

A relevant question one may pose is which heel value should be extracted from the CFD simulations or, similarly, at what point of the discharge process one should measure the heel, which itself makes the problem even more complicated considering the thixotropy or relaxation time of the fluids. In general, it was found here that the heel volume decreased very slowly with time after the first moment at which air started becoming entrained in the dip tube. Figure 3.7 shows the dependence of the heel volume in the bottle zone as a function of the air fraction in the tube.

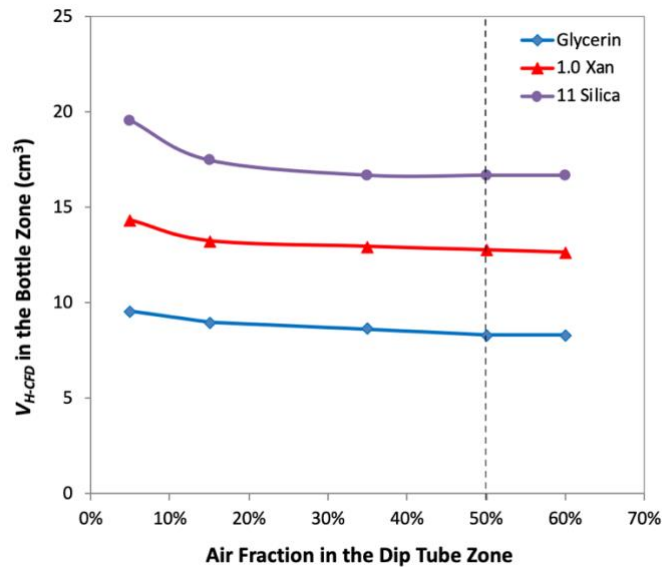


Figure 3.7 Dependence of the computationally predicted heel volume in the “bottle” zone on the air fraction in the “dip tube” zone for rheologically different fluids. Connecting lines were added to better visualize the trends.

As one can see, the heel volume in the bottle zone does not significantly change after the point at which the air concentration in the tube zone reaches 50%. It should be noted that a similar trend was obtained for all the fluids studied here, although not shown in Figure 3.7 to avoid confusion since the data points were close to each other and/or overlapping. In this work, *the heel volume in the bottle zone when 50% of the tube was filled with air was taken as the final heel volume*, named V_{H-CFD} for simplicity.

3.3.3.4 Experimental Determination of Heel Volume Using the PIV Imaging Method

(V_{H-PIV}). In this work, the PIV technique was not only used to obtain the velocity distributions but also for the visualization of the air-liquid interface during the discharge process and the quantification of the residual heel volumes once the discharge process was completed. To obtain an accurate profile of the heel, a cross-sectional slice of the bottom of the bottle was selected (Figure 3.8a). This can be quite challenging especially if the fluid is complex, considering optical obstacles such as the formation of air bubbles during the discharge blocking the view and the partial opacity of the complex fluid. In most cases these issues can be overcome by installing a color filter on the camera that minimizes the visibility of the air bubbles and by using a high-intensity laser sheet from the PIV system, often capable of penetrating inside the fluid. Then, the bottle was filled with the fluid up to a height of 20 mm of height from the bottom of the bottle, and the vacuum pump was turned on. When the discharge process stopped, the vacuum pump was turned off and a single image was taken using the PIV system. This image, showing the portion of the residual fluid where the tracer particles were found, was used to quantify the heel volume (Figure 3.8b). To do so the image was processed by the ImageJ software [138] for better visualization of the heel (Figure 3.8c). This was done by using the “*Process/Subtract*

Background” feature, after which a rolling ball radius of 100 pixels was entered with the “*Light Background*” option. This feature of ImageJ is based on the rolling-ball algorithm which is a frequently used method in the biomedical image processing [139]. This algorithm estimates the background intensity (using a user-specified threshold) of a grayscale image in case of an uneven exposure and subtracts it from the original image. This technique is described elsewhere in greater detail [140]. Upon completion of these steps, the portion of the experimental image corresponding to the “bottle” zone used in the CFD model, shown in Figure 3.8c, was further analyzed. To parameterize the heel profile, the selected heel picture was placed on a digital r - z coordinate system, where r is the radial coordinates with origin on the vertical centerline of the bottle extending up to the radius of the bottle, R , and z is the vertical coordinate with origin at the bottle bottom, i.e., where the bottle rests on a flat support. For the digitizing process, we used www.desmos.com/calculator, although any other approach that enables placing a picture on a coordinate system could also be used. Then, 8 radial positions were selected, and the exact z coordinates of the liquid heights at those r values were extracted, together with the z value of the dimple at the same r value. These data were exported to MS Excel, and a fourth-order polynomial function, $f(r)$, was fitted through the z values for the liquid surface. A similar procedure was also followed to parameterize the profile of the dimple, resulting in a fourth-order polynomial function, $g(r)$. The heel volume was then calculated using the following equation:

$$V_{H-PIV} = 2\pi \int_a^R r \cdot [f(r) - g(r)] dr \quad (3.4)$$

where a is the radial coordinate of the beginning of the bottle zone in Figure 3.8a. The heel volume obtained with this method will hereafter be referred to as “ V_{H-PIV} ”.

3.3.3.5 Experimental Determination of the Heel Volume Using the Weighing Method

($V_{H-Weight}$). In addition to the V_{H-CFD} , and V_{H-PIV} methods, a conventional discharged fluid collection approach was also used to validate the computational results. The bottle was filled with a liquid up to about 20 mm in height from the bottom, the modified hand pump was placed inside, and the vacuum pump was turned on.

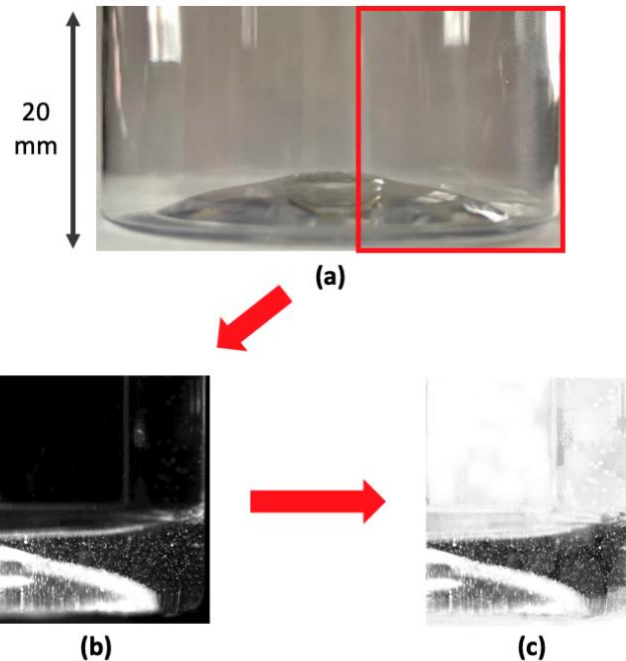


Figure 3.8 The three steps used in the experimental imaging method: (a) Image of the bottom of the bottle taken by a phone camera; (b) Raw image of the right-hand side of the bottle bottom obtained with the PIV camera after the discharge was completed; (c) Background subtracted-PIV image, as processed by ImageJ, used here to quantify the heel volume as described in the text.

After the discharge was complete (the moment at which the air enters the tube), the

vacuum pump was turned off, the tube was removed, the bottle was weighed, and the heel amount was calculated knowing the weight of the empty bottle. Since the fluid densities were all known, the measured heel amount was converted into heel volume, reported here as $V_{H-Weight}$.

3.4 Results

The experimental rheological data for different fluids are presented in Figure 3.9, showing the broad range of rheological properties of the fluid studied here. Adding xanthan gum resulted in a more shear-thinning behavior, as expected [40]. Highly viscous materials such as the Carbopol gel and all the pastes had a significant shear-thinning behavior as well as high low-shear viscosity limits (i.e., equilibrium viscosity), much higher than the xanthan gum gels. Figure 3.9 show the best-fitted curves based on the Carreau equation (Equation 3.1) from which the corresponding rheological parameters were extracted. Note that while the fitting was performed using the viscosity vs. shear rate data, the viscosities in Figure 3.9 were plotted against shear stress to better reveal the shape of each curve and facilitate their reading.

As one can see from this figure, the viscosity for those fluids drops abruptly in a certain narrow range of the shear stress, which may be interpreted as the yield stress. While the Carreau equation assumes the existence of the low-shear viscosity plateau and therefore no “true” yield stress, one can use this value to define an “effective yield stress”, σ_0 . Potanin and Shapley (2021) suggested an alternative definition of σ_0 as the stress of the mid-point of the viscosity on the plots like those in Figure 3.9. This definition works well, but we found that one can just as well use a simpler approach, namely defining the effective

yield stress σ_0 as the shear stress corresponding to a 1% drop in viscosity from the low shear plateau of the curves. The σ_0 values so obtained are presented in Table 3.3 along with Carreau fitting parameters for all the experimental curves. It is worthwhile to state that the question of the existence of the “true” yield stress, which has been discussed before by different authors [68, 69, 136, 141], is beyond the scope of this work. Here, we used the effective yield stress just as a convenient engineering parameter which, as shown below, correlates well with experimental data as well as numerical calculations of the heel.

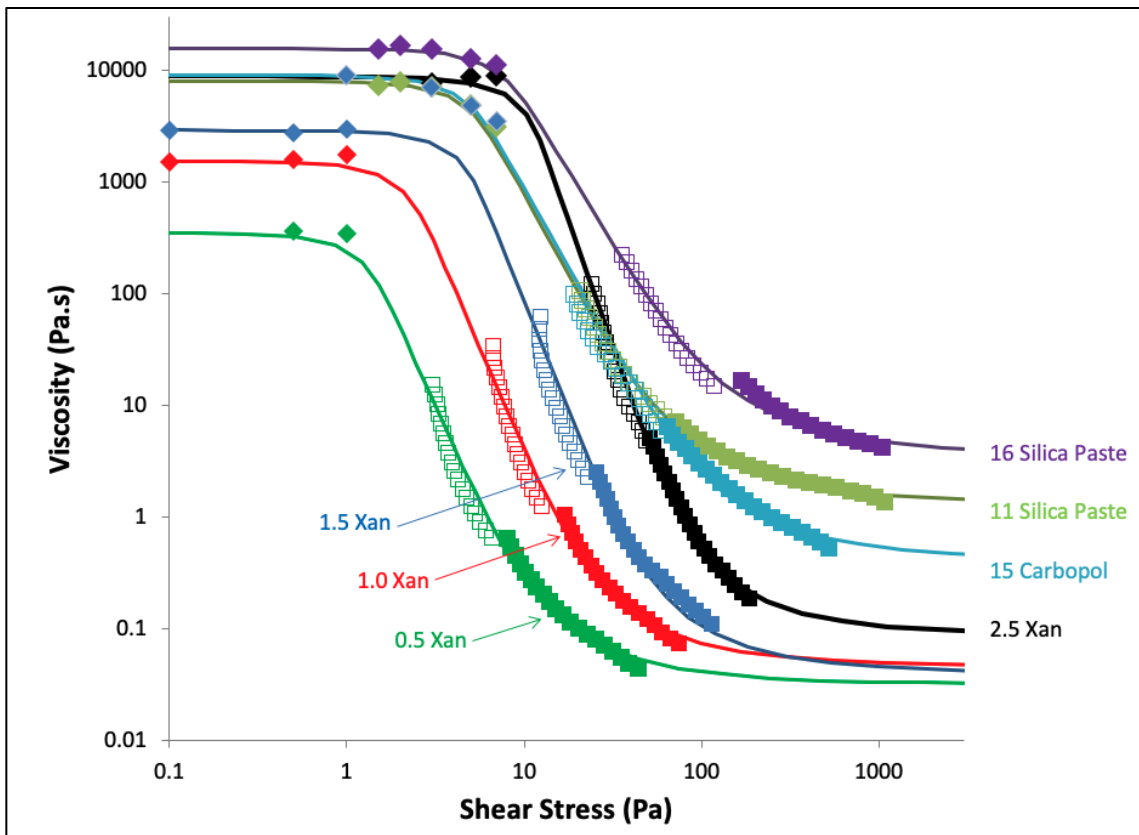


Figure 3.9 Experimental flow curves (symbols) and the curves fitted using the Carreau equation (lines). The former is a combination of three tests performed with various tools (vane-in-cup and DIN concentric cylinders) as described in the text: low-shear creep tests (filled diamonds), low-shear rate sweeps (empty squares), and high-shear rate sweeps (filled squares).

Table 3.3 Rheological Parameters for the Humectants, Gels and Pastes Experimentally and Computationally Studied in This Work

Fluid	η_0 (Pa·s)	η_∞ (Pa·s)	λ (s)	n (-)	σ (Pa)
Sorbitol	0.11	0.11	N/A	N/A	N/A
Glycerin	0.95	0.95	N/A	N/A	N/A
0.5 Xan	346	0.03	296	0.218	0.442
1.0 Xan	1520	0.05	762	0.213	0.838
1.5 Xan	2886	0.04	700	0.202	1.789
2.5 Xan	8800	0.09	943	0.180	4.241
15 Carbopol	9000	0.41	442	0.136	2.130
11 Silica Paste	8000	1.33	1798	0.256	2.126
16 Silica Paste	15500	3.61	2251	0.273	3.352

Additionally, in order to extend the range of possible rheological profiles, we performed numerical calculations of the heel for several imaginary model fluids whose rheological parameters listed are in Table 3.4. The corresponding flow curves are shown in Figure 3.10.

Table 3.4 Rheological Parameters for the Imaginary Model Fluids Computationally Studied in This Work

Fluid	η_0 (Pa·s)	η_∞ (Pa·s)	λ (sec)	n (-)	σ (Pa)
Model 1	4963	3.58	1472	0.29	1.607
Model 2	27860	2.62	3056	0.17	4.356
Model 3	10000	0.05	750	0.15	5.982
Model 4	20000	3.00	1000	0.08	8.879
Model 5	200	0.10	300	0.30	0.256
Model 6	400	0.05	500	0.20	0.303
Model 7	800	0.40	1500	0.10	0.200
Model 8	200	1.00	50	0.30	1.538

The reason for this inclusion was to better verify potential correlations between the heel and critical rheological parameters. Indeed, one can see from the experimental results

in Figure 3.9 that for the real fluids studied here having higher viscosity η_0 also means having higher yield stress σ_0 . Therefore, we additionally examined model fluids that have higher (Model 7) and lower (Model 8) low-shear viscosities than the experimental fluids with the same yield stress point.

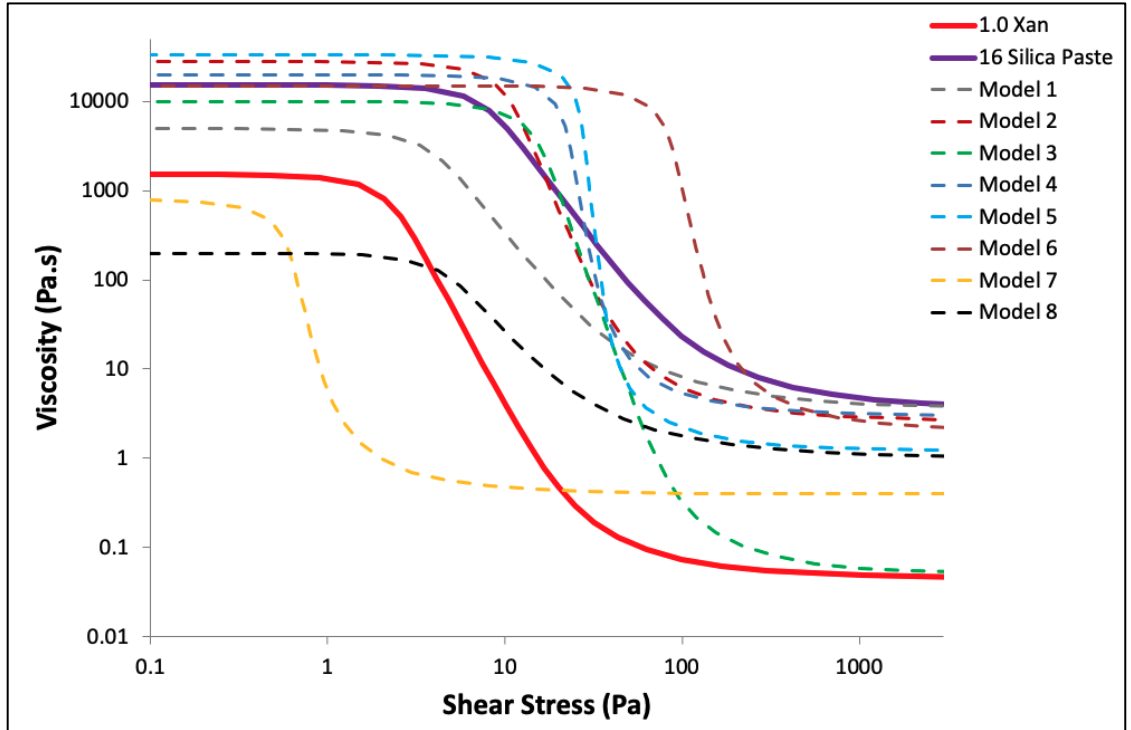


Figure 3.10 Flow curves for the eight additional imaginary “model” fluids used to verify correlations between CFD calculations of the heel to the rheological parameters. Two curves of the fluids tested experimentally from Figure 3.9 are also shown for comparison.

The results of the heel profiles obtained by PIV and CFD are presented in Figure 3.11. The visual agreement between the experimental results and the computational predictions is overall quite good. For sorbitol and glycerin, both Newtonian fluids, a flat heel profile was obtained. However, as the complexity of the fluid increased, the heel volume increased significantly.

It is interesting to notice that while for most of the fluids the shape of the experimental heel profile was smooth, a slightly wavy heel profile was obtained for the xanthan gels, especially when the xanthan concentration was higher (e.g., the 2.5 Xan profile). This is typical for xanthan gum gels since they possess high viscoelasticity. However, the CFD model did not include viscoelasticity and therefore the experimental wavy profiles could not be replicated by the simulations. Nevertheless, the overall qualitative agreement between the experiments and the simulations is quite good.

In order to better understand the heel results, examining shear rate maps could be useful. Figure 3.12 shows the CFD-predicted shear rate contour plots for selected fluids of low and high complexity, i.e., 0.5 Xan, 1.5 Xan, and 16 Silica Paste, respectively. The zone near the dip tube entrance had the highest shear rate, while lower shear rate values can be seen as one approaches the bottle wall. Furthermore, the low shear stress zone shrinks as the solid-like behavior of the fluids increases (higher σ_0), which can be intuitively expected. This also visually correlates with the results previously presented in Figure 3.11: as the size of the unsheared zone increases, the heel increases.

The overall comparison between V_{H-CFD} , $V_{H-Weight}$, and V_{H-PIV} is presented in Figure 3.13. The average error between V_{H-CFD} and $V_{H-Weight}$ was found to be 10%, whereas the average error between V_{H-CFD} and V_{H-PIV} was 8%, and between V_{H-PIV} and $V_{H-Weight}$ was 7%, indicating substantial agreement between the computational and experimental methods presented here.

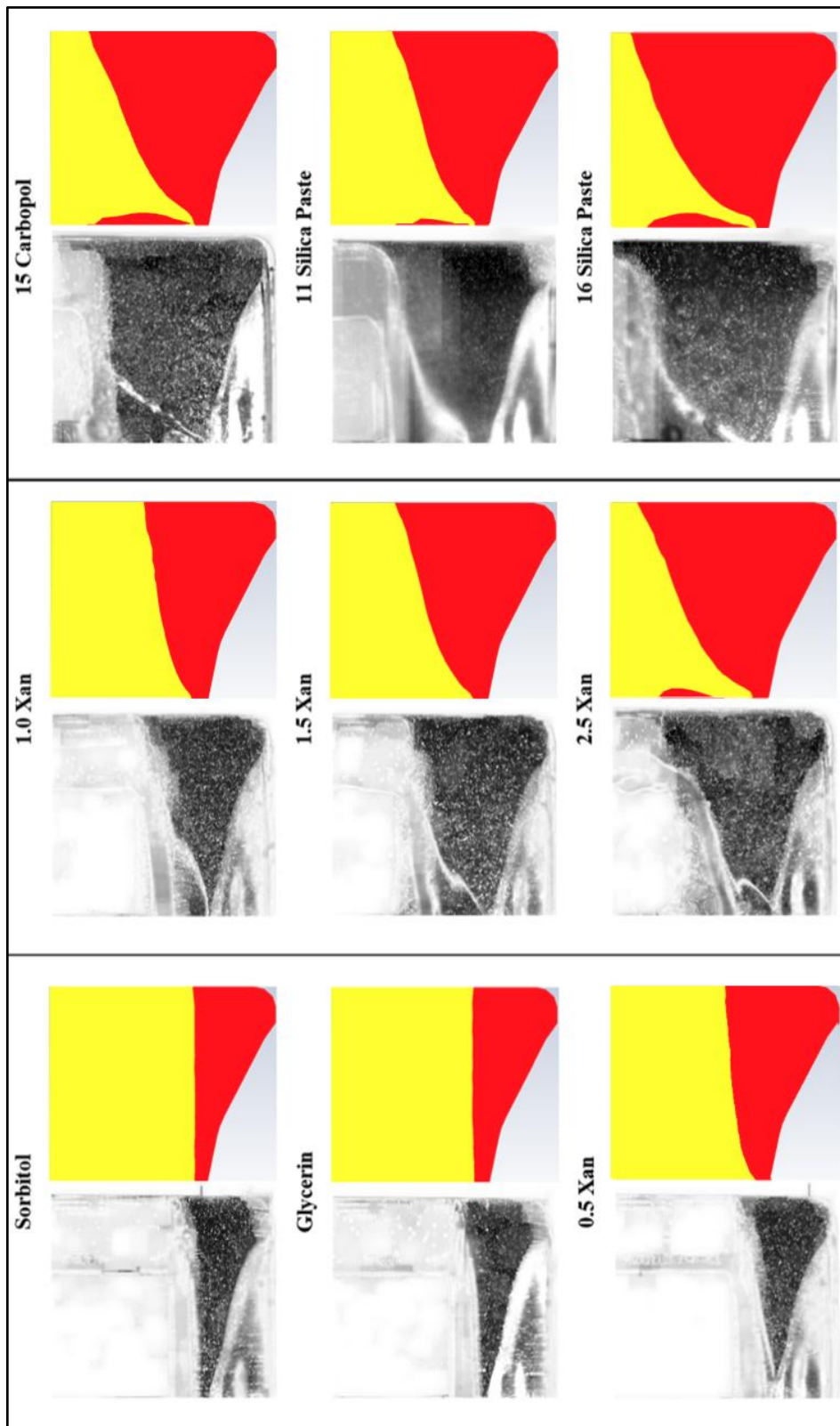


Figure 3.11 Heel volume profiles obtained by PIV (left panels; shown in grayscale, where the darker gray color corresponds to the liquid phase) and CFD (right panels; shown in yellow and red colors, corresponding to the air and liquid phases, respectively). Only the right-hand side of the bottle (red insert in Figure 3.8a) is shown in the panels.

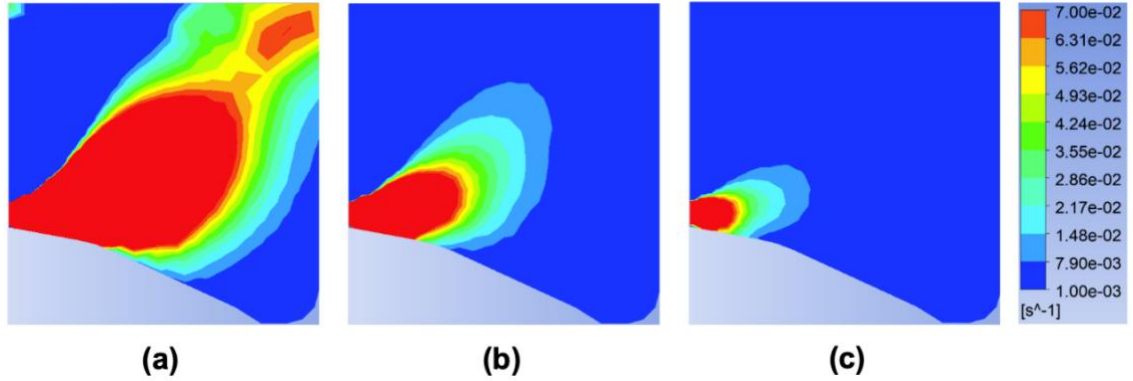


Figure 3.12 Shear rate contour plots in the bottle zone for selected complex fluids during their discharge at $t=5$ s: (a) 0.5 Xan; (b) 1.5 Xan; (c) 16 Silica Paste.

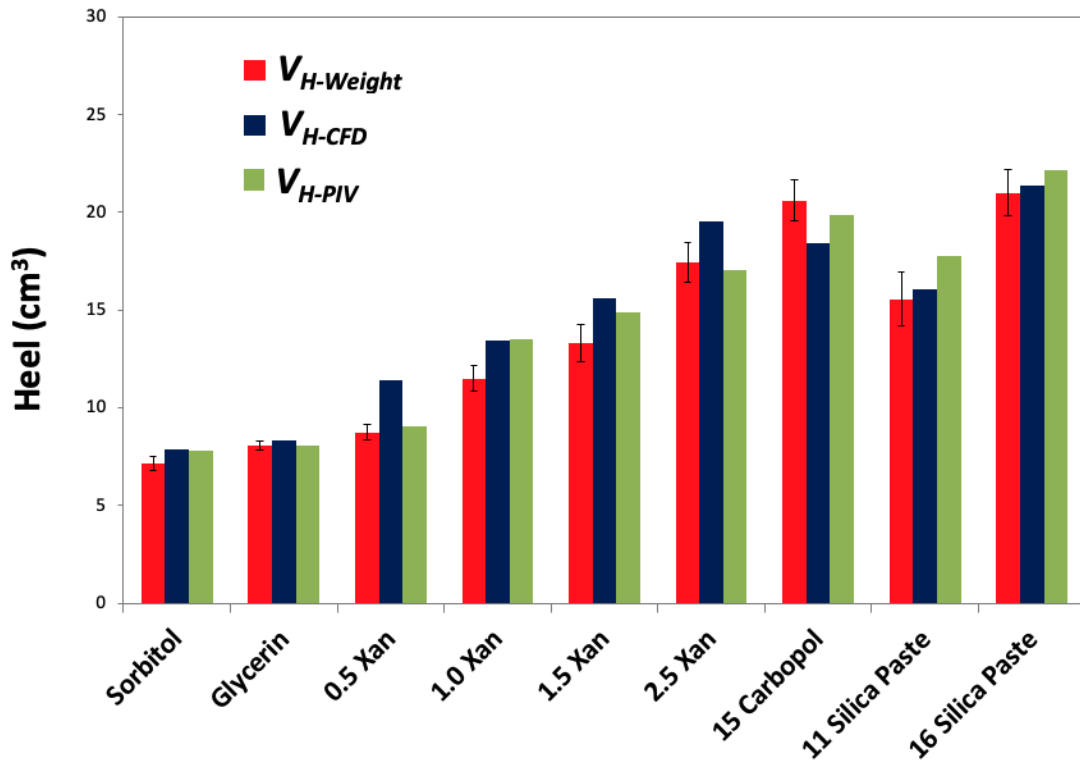


Figure 3.13 Overall comparison of $V_{H-Weight}$, V_{H-PIV} , and V_{H-CFD} for all the fluids studied in this work. Error bars represent 95% confidence intervals, obtained by three repetitions of each experiment.

3.5 Discussion

The results presented above show that heel amount in consumer bottles can be determined or predicted through the use of PIV (V_{H-PIV}) and CFD (V_{H-CFD}). Potentially this approach can be extended to a variety of applications. This work presents novel results considering the lack of research work performed in this field. To the best of our knowledge, most of the previous research on the discharge of complex fluids was conducted in the systems having orifices from which the fluid was discharged *downwards*, as in the case of a discharging vessel (gravitational), or *horizontally* in the case of a pipe. In this work, the fluids are discharged *upwards* through a dip tube, which is very common for practical applications (e.g., liquid hand soap, lotion, shampoo, shower gel, ketchup, and oil dispensers). Moreover, unlike the only present study on the heel that was conducted in the industrial tanks [40], this work consists of the investigation of the heel in a commercial consumer bottle, therefore paving the way for future research in a variety of consumer containers through the use of the abovementioned techniques with the ultimate objective of improving the product and packaging design and eventually, minimizing the heel volume.

The results presented in this study show that CFD can be effectively used to predict the heel. However, from a practical point of view, it would also be convenient to be able to predict the heel in the given bottle using a simple correlation, possibly involving a minimal number of rheological parameters. To address this question, one first needs to define the characteristics of the heel volume that would be less dependent on the particular shape of the bottle. The total heel volume, V_H , may be written as follows:

$$V_H = V_{H0} + \Delta V_H \quad (3.5)$$

where V_{H0} is the fluid volume that is below the lower end of the dip tube. For the bottle studied here the value of V_{H0} was found to be equal to 7.86 cm^3 . This portion of the fluid would remain in the bottle irrespective of the fluid rheology once the air starts becoming entrained in the dip tube. In this equation, ΔV_H is the *reduced heel volume*, i.e., the additional portion of the heel that can possibly be left in the bottle as a result of the complex rheology of the fluid, and especially the effective yield stress. Clearly, for a Newtonian fluid ΔV_H would be zero since the air-liquid interface would be flat at all times, assuming pseudo-stationary fluid removal.

In order to establish possible correlations relating the reduced heel to the rheological parameters, we first plotted ΔV_H vs. the effective yield stress, σ_0 . The results, presented in Figure 3.14a, show that σ_0 is a very good predictor of the heel volume, irrespective of the type of fluid used, real or model. The resulting correlation predicting the reduced heel was found to be:

$$\Delta V_H = 5.20 \cdot \sigma_0^{0.62} \quad (3.6)$$

This correlation had an R^2 value of 0.96. This result is, of course, not surprising since yield-stress fluids tend to form a funnel around the tip of the dip tube which facilitates earlier air entrance into it.

Figure 3.14b shows a similar correlation between ΔV_H and η_0 . In this case, the

agreement was generally appropriate for the real fluids, but for most of the model fluids, and especially the more extreme cases represented by model fluids Model 7 and Model 8, the agreement was very poor (overall $R^2=0.77$).

The predictive value of Equation 3.6 is further confirmed by the parity plot in Figure 3.15, comparing the ΔV_H values predicted with Equation (3.6) ($\Delta V_{H-Predicted}$) vs. those obtained through CFD simulations (ΔV_{H-CFD}). Clearly, the agreement is quite satisfactory.

It should be reminded that in order to understand the effect of complex fluid rheology on the discharge process, one has to keep all other operating and geometric parameters constant (such as suction pressure, tube and bottle geometry, etc.). This was the main constraint that limited the scope of our investigation to a single geometry. It follows that Equation (3.6) is a dimensional equation valid only for dispensing bottles having the same tube-to-bottle diameter ratio as the one studied here ($d/D=0.12$). However, the analysis presented in this work clearly shows that the effective yield stress is the dominating parameter for heel formation, thus giving future researchers using CFD to predict V_H a good starting point on what rheological parameter to alter to obtain a product that minimizes heel formation.

The V_{H-CFD} approach presented here can be used by product developers, especially in the oral and personal care industries, alleviating the need of formulating products and determining the heel amount experimentally, which itself is quite a time consuming and would result in a significant waste of material during the formulation process. Instead, upon the extraction of the rheological data of a given product using a rotational rheometer, one can simulate the discharge process to optimize the container design, including an

optimized d/D ratio (where d is the tube orifice diameter and D is the bottle inner diameter) as well as an optimized geometry of the bottom of the bottle (including the dimple) that minimizes the heel volume. In addition, by varying the suction velocity boundary conditions in CFD, one could determine the optimum geometric characteristics to improve the hand pump designs.

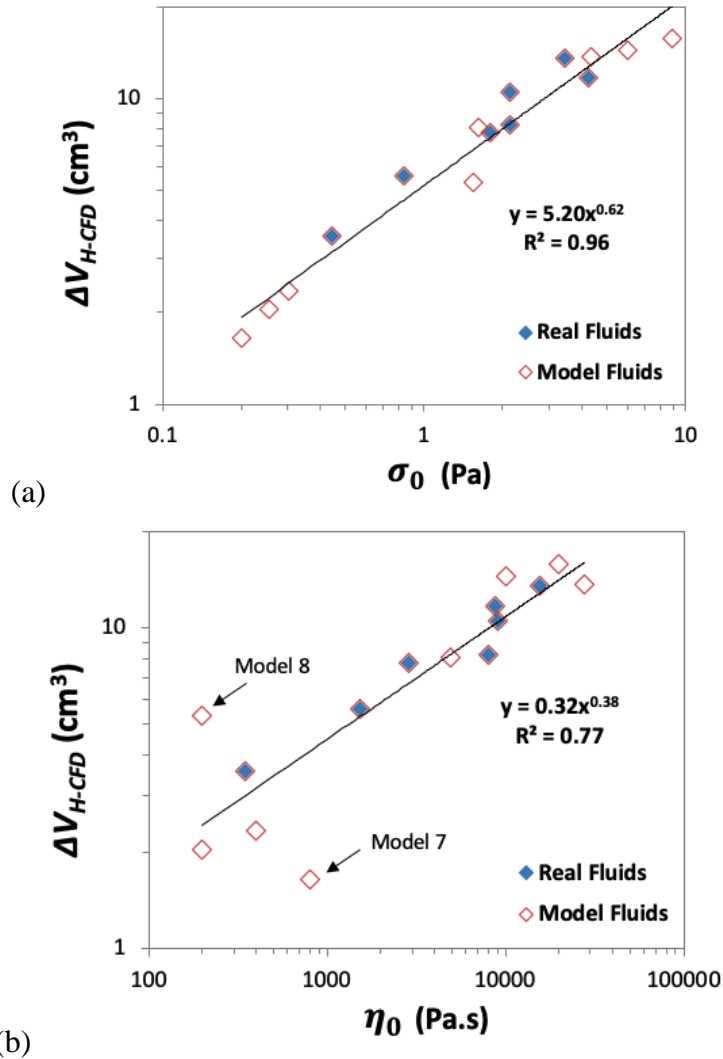


Figure 3.14 Dependence of reduced heel volume ΔV_H on the rheological parameters of the fluids: (a) effective yield stress, σ_0 ; (b) low shear viscosity limit, η_0 .

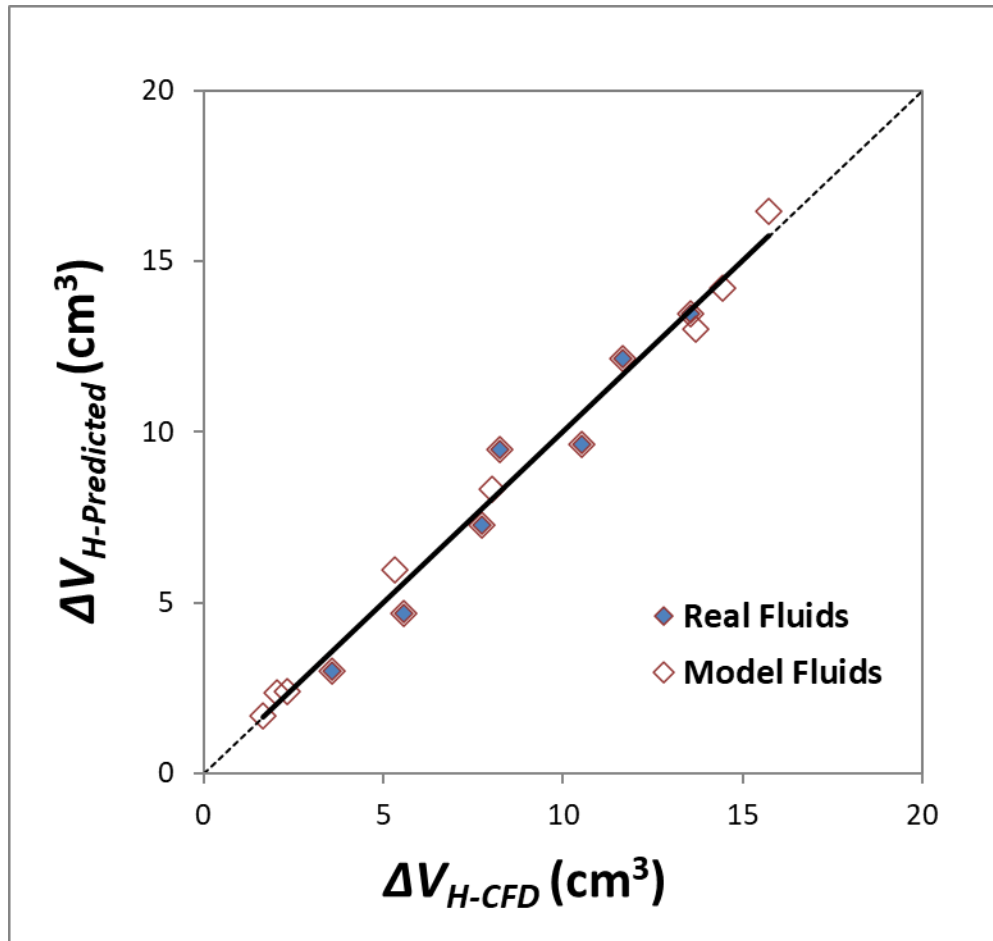


Figure 3.15 Parity plot of the ΔV_H values predicted with Equation 3.6 ($\Delta V_{H-Predicted}$) vs. those obtained through CFD simulations (ΔV_{H-CFD}).

Similarly, the V_{H-PIV} method presented here could help in the experimental determination of the heel. Furthermore, V_{H-PIV} not only quantifies the amount of heel but also its cross-sectional profile, which, again, could be used to monitor how the heel profile changes with respect to the fluid rheology and the container geometry.

This work additionally shows that the recently developed refractive index matching method [8] resulting in optimized transparency of otherwise opaque fluids can be effectively used to study the hydrodynamics of highly complex pastes using optical methods such as PIV. In fact, the good agreement between the heel profiles of silica pastes

obtained using experimental and computational methods described here indirectly shows that the velocity values determined by PIV were quite accurate since these values were used as the boundary conditions in the simulations. Furthermore, the heel profiles were also clearly detectable for pastes, as shown in Figure 3.11, indicating that the laser beam successfully penetrated inside the fluid.

3.6 Conclusions

A number of conclusions can be drawn from this work:

- CFD simulations based on the Carreau model predict the heel volume in the consumer hand pump bottles with less than 10% error;
- The PIV technique can not only be used to obtain velocity distributions but also to visualize and quantify the heel volume in any type of container, provided that the container and the fluids are transparent;
- It is possible to optically investigate highly complex pasty materials through the use of the refractive index matching method;
- Heel volume correlates well with the effective yield stress of the fluid, i.e., the stress at which viscosity drops;
- It is expected that the results obtained in this work will help guide product designers and packaging engineers in designing dispensing bottles for many industrial applications.

CHAPTER 4

EFFECT OF RHEOLOGY AND OPERATIONAL PARAMETERS ON THE DISCHARGE HYDRODYNAMICS OF CONSUMER DISPENSING BOTTLES

4.1 Abstract

Complex fluids, such as gels, shampoos, and creams are ubiquitous in the consumer product industry. However, little information is available on the discharge process from consumer packaging, often resulting in a heel, i.e., the residual waste material after the discharge process is complete. Here, we used Particle Image Velocimetry (PIV) to investigate the discharge of rheologically different fluids from a dispensing bottle provided with a modified hand pump and different dip tube diameter-to-bottle diameter ratios (d/D) and discharged under different differential pressures. The data were analyzed by defining the dimensionless *Region of Interest (ROI)* to capture the relative “high velocity” region in the fluid during the discharge process and determine how ROI varied with d/D and ΔP . The characteristics of the flow during the discharge determine the heel volume at the end of the process. Correlations are presented predicting the heel volume as a function of rheological and operational parameters.

4.2 Introduction

Complex fluids are mixtures that incorporate two phases coexisting at the microscopic level, such as ketchup, shampoo, and toothpaste [1]. The presence of coexisting phases in these fluids results in a non-linear relationship between shear rate and shear stress, making their flow behavior highly complex and the rheological characterization quite important for a variety of industrial applications [4, 5, 142].

Improper rheological characterization of such fluids, as well as the sub-optimal design of their containers (e.g. a vessel, pipe, dispensing system, or consumer packaging), may result in many challenges, especially in the consumer industry, such as issues with the extrusion of toothpaste from their squeeze tubes, pumping of these fluids through long pipes in a plant [25, 37], or inhomogeneities in process equipment, as discussed elsewhere [143-147]. For instance, in mixing processes involving complex fluids, a well-mixed region (often referred to as a “cavern”) may be found in a region near the impeller [146]. Outside this region, there is either no flow in the case of a viscoplastic fluid [113] or a slow, negligible motion in the case of a pseudoplastic fluid, resulting in the formation of a “pseudo-cavern” [148]. In such cases, it is often desirable to eliminate the stagnant or low-velocity zones to ensure that all the fluid inside the vessel is in motion. To do so one should carefully select the operational and design parameters of the mixing system, such as the agitation speed, vessel shape and diameter, impeller diameter, impeller clearance, and others, with the ultimate objective of alleviating the issues associated with poor mixing, as well as mass and heat transfer [146].

Proper selection of such parameters is also critical for other processes involving complex fluids, such as their discharge from vessels or containers, which is another

ubiquitous process found not only in industrial practice but also in daily life. For instance, it is often desired that many personal and oral care products (e.g., dishwashing liquids, lotions, liquid hand soaps, and toothpaste) discharge easily and nearly completely from their containers [132]. Nevertheless, the complex nature of fluids such as yield stress, and high viscosity often negatively affects this process by reducing the discharge rate and resulting in a residual fluid left in the container at the end of the discharge process, often referred to as “heel” [40].

In order to provide a more fundamental understanding of these processes, as well as reduce the impact of the issues associated with them, several researchers have studied the discharge of complex fluids through orifices, as more extensively reviewed elsewhere [132]. Those researchers quantified the frictional losses at the orifice and suggested general correlations representing the complex discharge behavior that varies significantly depending on the fluid rheology and the geometric characteristics of the orifice, such as the orifice-to-container diameter ratio d/D (where the container is either a vessel or a pipe) as well as the orifice length and shape [17, 31, 34, 35].

However, there has been a lack of information on the discharge hydrodynamics of complex fluids, especially for more complex geometries such as dispensing bottles, from which the fluid is discharged upwards. The utilization of experimental and predictive flow quantification methods [149] such as Electrical Resistance Tomography (ERT) [94, 95], Magnetic Resonance Imaging (MRI) [40], Particle Image Velocimetry (PIV) [84], and Computational Fluid Dynamics (CFD) [37, 109], can provide point-by-point velocity data within the investigated system, thus giving detailed information on the geometric and rheological factors that cause the reduction of the discharge rate and contribute to the

formation of a heel [132]. Nonetheless, surprisingly, this important topic has not received much attention despite its relevance.

To the best of our knowledge, only two studies can be found in the literature on this specific topic. A recent study conducted by Potanin and Shapley showed that the discharge of highly complex fluids from industrial vessels can be monitored using MRI and that the heel volume can be predicted using CFD [40]. This work was followed by another study conducted in consumer dispensing bottles, showing that PIV is an effective tool to determine the amount of heel, even for highly concentrated silica pastes, through the utilization of the refractive index matching method [8]. In addition, the same authors showed that a CFD approach can also be applied to such types of containers [150]. However, both these investigations were primarily focused on the development of novel methods to predict the heel amount, and they only indirectly indicated that the flow pattern *during* the discharge process can result in different heel profiles *at the end* of the process.

For example, Potanin and Shapley generated MRI images for two selected fluids with different rheologies (two gels having different xanthan gum-CMC concentrations) and showed that adding CMC affected the flow pattern, resulting in a smoother flow and hence a more homogeneous velocity distribution around the orifice of the vessel, resulting in a smaller heel [40]. Similarly, in our recent work, we qualitatively analyzed the shear maps obtained from CFD for three rheologically different gels and pastes, and we showed that the sheared zone shrunk in size as the fluid microstructure was more complex, resulting in a larger heel [150]. While both these studies showed that the heel decreased as the overall motion of the fluid in the container increased, a more comprehensive study on how the geometric and rheological parameters affect the discharge hydrodynamics during the

discharge process has not been conducted to date.

Therefore, in this work, we experimentally quantified, via PIV, the hydrodynamics of the discharge process of a number of rheologically different complex fluids from a consumer dispensing bottle as a function of the dip tube diameter-to-bottle diameter ratio (d/D), and the differential suction pressure (ΔP). We were then able to generate a correlation relating the heel volume *at the end of the process* to the size of the zone of fluid where the velocities were above a minimum threshold value *during the discharge process*. In addition, we also established more practical correlations to predict the final heel volume as a function of the fluid rheological parameters and the values of d/D and ΔP , or the volumetric flow rate, Q , which can help researchers and product developers design an optimal dispensing system for a given product.

Finally, we used CFD to study the discharge process by computationally mapping the velocity profiles in the fluids. A comparison of these predictions with the experimental PIV data showed significant agreement for most complex fluids, but less so for those fluids whose rheology is also controlled by viscoelastic or extensional forces, which could not be incorporated into the CFD model.

4.3 Experimental Equipment, Material, and Method

4.3.1 Experimental Equipment

4.3.1.1 Equipment Used in the Preparation of the Fluids and for Rheological Characterization. The fluids used in the experiments were prepared and characterized using the following equipment:

Mixer. A Whip Mix WPM2 mixer (Whip Mix Corp., Louisville, KY) was used to prepare all fluid mixtures, as described earlier in this work (Chapter 2).

Centrifuge. In order to remove any residual air bubbles, all fluids were centrifuged at low agitation speeds (always below 3000 rpm, depending on the viscosity of the fluid) for 3 minutes using an Eppendorf Centrifuge 5804 (ThermoFisher Scientific, Waltham, MA), as described earlier in this work (Chapter 3).

Rheometer. A DHR-3 rheometer (TA Instruments, Delaware, USA) with a vane-in-cup or DIN concentric cylinder geometry was used to rheologically characterize the fluids, as previously described in this work as well as in [150].

4.3.1.2 Equipment Used to Quantify the Discharge Process and Heel Formation. The actual experiments were conducted using the apparatus shown in Figure 4.1. The details of this equipment are described below.

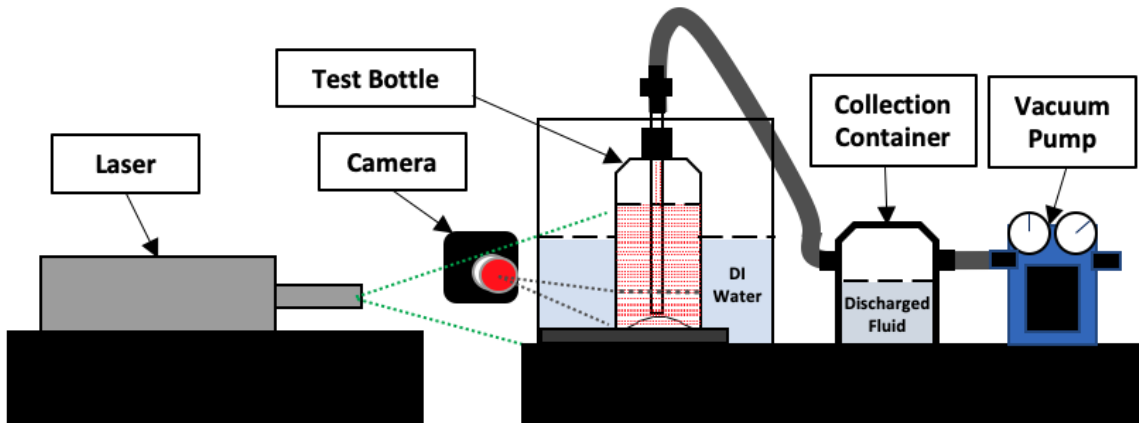


Figure 4.1 Diagram of the experimental system (not drawn to scale) including the PIV system.

Vacuum Pump. A GAST DOA-P704-AA vacuum pump (GAST, Benton Harbor, MI, USA) was used to generate the desired suction pressure to allow the fluid in the bottle

to be discharged from it.

Manometer. A Traceable® digital manometer (VWR International, Pennsylvania, USA) was used to set the suction pressure to the desired value. All the pressure measurements were taken at the orifice of the dip tube with the dip tube removed from the bottle.

Test Bottle, Dip Tubes, and Discharge System. A commercial lotion bottle (total height, $h_B=103$ mm; inner diameter, $D=42$ mm; outer diameter, $D_B=45$ mm) identical to that used in Chapter 3 was used here (Figure 4.2). This bottle had a bump at the bottom with a peak height of 5 mm from the bottom rim of the bottle and was provided with a dip tube centrally placed 1.75 mm above the peak of the bump. The bottle was modified to allow for continuous out-pumping of the fluid so as to obtain accurate velocity measurements. Accordingly, the original hand pump's spring and piston chamber (Figure 4.2a) were replaced with a tube fitting (Figure 4.2b), and the dip tube portion of this assembly was passed through a bottle cap exactly fitting the neck of the bottle (Figure 4.2b) and providing mechanical stability to the tube. The upper portion of the tube was fitted with a plastic connecting element to a vacuum pump with a flexible tube. Additionally, although not seen in Figure 4.2b, a small hole (about 1 mm in diameter) was also created between the center and the side of the cap to avoid any vacuum buildup above the liquid in the bottle.

In order to improve the accuracy of the optical measurements, the original translucent dip tube was replaced with one of three different transparent polycarbonate tubes of different internal diameters, as follows: (1) 4 mm ($d/D=0.095$); (2) 5 mm ($d/D=0.119$); (3) 6 mm ID ($d/D=0.143$). The bottle was secured with double-sided tape to

a heavy black metal plate to ensure its stability while pumping during the PIV measurements. This assembly was then placed inside a small acrylic square tank and mounted in front of the PIV system, as shown in Figure 4.1. The tank was filled with deionized water so as to minimize the laser light refraction.

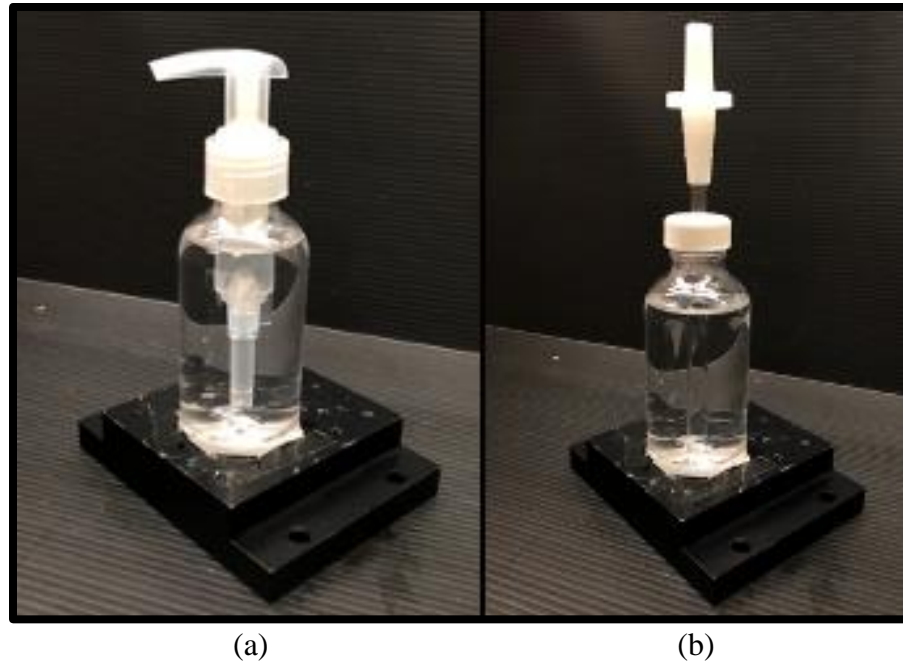


Figure 4.2 Commercial dispensing bottle: (a) original dispenser; (b) modified dispenser.

Particle Image Velocimetry System. The PIV system used here (New Wave Research Model Solo 120 15-HZ (Fremont, CA, USA)) was identical to that used previously presented and described in detail in Chapter 3.

4.3.2 Materials

Fluids. In order to study the discharge of fluids with wide rheological properties, two humectants (sorbitol and glycerin), three gels, and four pastes were used. The compositions of the fluids are summarized in Table 4.1. The detailed procedure for the

preparation of the fluid mixtures is reported earlier in Chapter 3.

Table 4.1 Composition of the Fluids Studied in This Work

Fluid	Xanthan Gum (wt.%)	Thickening Silica (wt.%)	Sorbitol (wt.%)	Glycerin (wt.%)	Water (wt.%)	Density (g/cm ³)
Water	-	-	-	-	100	1.000
Sorbitol	-	-	70	-	30	1.343
Glycerin	-	-	-	100	-	1.260
1.0 Xan	1.0	-	-	49.50	49.50	1.104
1.5 Xan	1.5	-	-	49.25	49.25	1.106
2.5 Xan	2.5	-	-	48.75	48.75	1.110
8 Silica Paste	0.46	8.00	-	71.85	19.69	1.287
11 Silica Paste	0.39	11.53	-	69.14	18.94	1.331
13 Silica Paste	0.43	13.00	-	67.95	18.62	1.361
16 Silica Paste	0.37	16.36	-	65.37	17.90	1.405

Tracer Particles for PIV Study. Red fluorescent polyethylene particles (Cospheric, CA, USA) (Particle size=10-45 μm , density=0.995 g/cm³) were used to track the flow during the PIV experiments. A 100-mL stock solution containing 1 g of tracer particles was prepared. After the addition of a few drops of Tween 80 (Sigma-Aldrich 9005-65-6) as a wetting agent, the suspension was stirred at 100 rpm using a magnetic stirrer. About 10 mL of this stock solution was added to the water component of the fluids during their preparation.

4.3.3 Methods

4.3.3.1 Rheological Characterization of the Fluids. The rheological characterization of the complex fluids studied here was identical to the one presented in Chapter 3 and included

three steps: (1) Conducting creep tests using the vane geometry for the low shear range (at very low stresses to cover the low shear plateau); (2) Conducting shear rate sweep tests using the vane geometry for the moderate shear range (from 0.2 s^{-1} to 10 s^{-1}), i.e., where the viscosity drops abruptly; (3) Conducting shear rate sweep tests using the DIN concentric cylinder geometry for high shear range (from 10 s^{-1} to 1000 s^{-1}), to obtain the equilibrium (high shear) viscosity.

The rheological raw data were fitted to the Carreau model equation, as described earlier. The resulting rheological parameters of the fluids studied here are shown in Table 4.2, and their corresponding rheology curves are plotted in Figure 4.3. It should be remarked that the fluids selected here have a wide range of rheological parameters, as Figure 4.3 clearly indicates. The effective yield stress, σ_0 , was defined as the stress corresponding to a 1% drop of viscosity from the low shear plateau of the curves, as reported previously in Chapter 3.

Table 4.2 Rheological Parameters of the Complex Fluids Studied in This Work

Fluid	η_0 (Pa·s)	η_∞ (Pa·s)	λ (s)	n (-)	σ_0 (Pa)
1.0 Xan	1520	0.05	762	0.213	0.838
1.5 Xan	2886	0.04	700	0.202	1.789
2.5 Xan	8800	0.09	943	0.180	4.241
8 Silica Paste	1750	0.59	486	0.270	1.593
11 Silica Paste	8000	1.33	1798	0.256	2.126
13 Silica Paste	8200	1.90	1018	0.258	3.856
16 Silica Paste	15500	3.61	2251	0.273	3.352

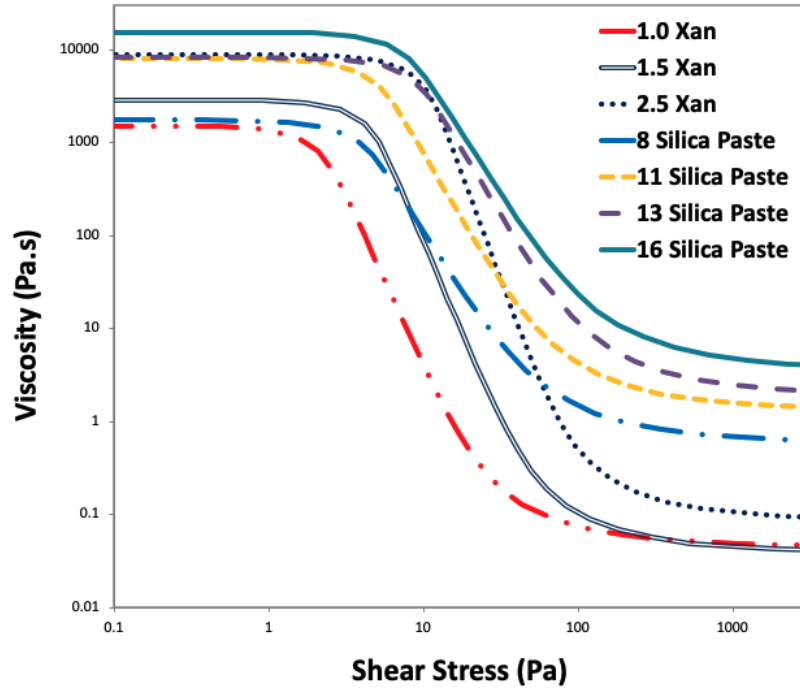


Figure 4.3 Rheology curves of the complex fluids studied in this work.

4.3.3.2 Experimental Determination of the Velocity Distributions Using PIV.

A typical experiment involved completely filling the bottle with the fluid, attaching the dip tube to the collection container linked in series to the vacuum pump, turning on the vacuum pump, and beginning the PIV measurement. The PIV measurement was initiated after powering the vacuum pump. The vacuum pump gradually emptied the bottle by continually removing the liquid from the dip tube and discharging it into a separate empty container (Figure 4.1), eventually emptying the bottle. During the continuous discharge, PIV collected image pairs at a frequency of 8 Hz. The time difference between two laser pulses, Δt , was 400 μs for 0.5 Xan, 1000 μs for 1.0 Xan and 1.5 Xan, 3000 μs for 2.5 Xan and 8 Silica Paste, and 5000 μs for other silica pastes. These Δt values were chosen depending on the viscosity of the fluid since for higher viscosity fluids, a larger Δt is required to adequately capture the tracer particle movement, and hence the fluid velocities, while a

shorter Δt was selected for low viscosity fluids in order to keep the particles within their interrogation window of the PIV system. In all cases, at least 100 image pairs were taken (depending on how rapidly the bottle was being drained) and averaged in order to minimize the error, as described previously [150]. It should be noted that only the region of the bottle marked with dashed black lines in Figure 4.4a was analyzed, since, outside this region, there was either no flow or significant light reflection caused by the dimple of the bottle. Thus, any data in this region were discarded. The velocity maps obtained by PIV were then extracted and transferred to Tecplot software (Tecplot, Bellevue, WA) for their conversion to contour maps, an example of which is shown in Figure 4.4b.

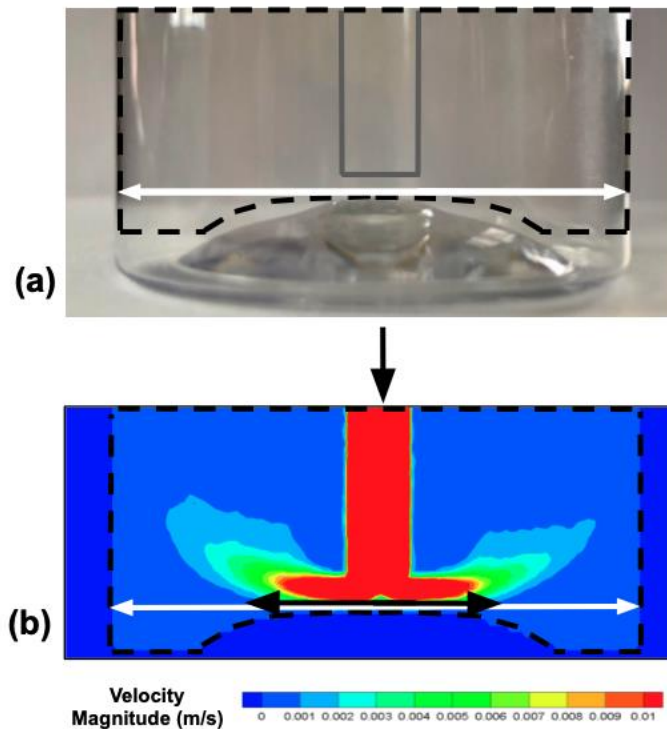


Figure 4.4 PIV analysis: (a) picture of the bottom of the bottle up to a 20 mm height showing the region analyzed here (dashed black lines) and the radial plane on the bottom (equal to the internal diameter of the bottle, shown as a white arrow) on which the ROI analysis was made; (b) example of an experimental velocity contour map as described in the text, and the region on the bottom (shown as black arrows) that is significantly affected by the flow.

It should be noted that all the velocity contour maps presented in this work correspond to the *velocity magnitude* maps, the values of which were calculated using the following formula:

$$\bar{v} = \sqrt{v_i^2 + v_j^2} \quad (4.1)$$

where \bar{v} is the local velocity magnitude (m/s) on a vertical cross-sectional plane through the dip tube, and v_i and v_j are, respectively the axial and radial velocities at the same location.

4.3.3.3 Analysis to Extract the Region of Influence (ROI) from PIV Data. During the discharge process, the entire region under investigation was in motion since none of the fluids studied here were “true” yield stress fluids (in which case an empty pocket would form around the dip tube orifice and the discharge would stop): as the fluid was discharged upwards through the dip tube, an equal amount of fluid was withdrawn from the bottle and the fluid level dropped. However, the velocities in the region closer to the lower end of the dip tube bottom were typically much higher than everywhere else in the bottle, as in the case of the abovementioned “pseudo-caverns” in the mixing processes [143, 144]. In addition, although the whole process was intrinsically time-dependent, the region of interest in Figure 4.4 where the flow intensity was higher could be considered to be operating under pseudo-steady state conditions since the bottle emptying process was slow. Therefore, in order to quantify this relative “high velocity” region, we defined the *Region*

of Influence (*ROI*) as the following dimensionless number:

$$ROI = \frac{d_I}{D} \quad (4.2)$$

where D is the bottle internal diameter and d_I is the “influenced radial diameter”, i.e., the horizontal distance from the vertical centerline where the fluid velocities on the plane below the dip tube (i.e., at 0.5 mm off the bump) were equal to, or greater than, 0.001 m/s. Figure 4.4b presents an example of d_I (shown as a *black* arrow), and D (shown as a *white* arrow in Figure 4.4b). It follows that *ROI* can only have values ranging from 0 to 1, where 0 indicates essentially no flow just below the dip tube and 1 represents the situation where the entire bottom of the bottle is fully swept by the flow. In this study, 0.001 m/s was selected as the threshold for the *ROI* because: (1) it was experimentally observed that, irrespective of the fluid type used here, regions having velocity values lower than 0.001 m/s value were appeared to be either static or nearly static when comparing image pairs obtained for the selected Δt , and (2) if any velocity was measured at all by the PIV in those regions significant experimental error was observed below this value, indicating that the PIV system was incapable of accurately measuring velocity values below 0.001 m/s.

4.3.3.4 Experimental Determination of the Reduced Heel Volume Using Weighing Method (ΔV_H). In order to determine the heel volume in each case, separate experiments were conducted. The bottle was filled with liquid up to 20 mm in height from the bottom, the modified hand pump dip tube inside was placed inside, and the vacuum pump was turned on. When air entered the tube and concluded the discharge process, the vacuum

pump was turned off. The bottle was then weighed (after the dip tube was removed). The heel amount was calculated by subtracting the mass of the bottle from the measured heel. Finally, as the fluid density was known, the mass of the heel in grams was converted to heel volume in cm^3 . From this volume, 7.8 cm^3 was subtracted as it corresponds to the volume below the dip tube orifice level (horizontal) in which region there will be a heel irrespective of the fluid rheology. The resulting heel volume, named “*reduced heel*” or “ ΔV_H ” as presented in a previous work [150] was reported.

4.3.3.5 Computational Determination of the Velocity Distributions Using CFD.

Although the main focus of this work was to experimentally investigate the discharge hydrodynamics of complex fluids from dispensing bottles, the velocity distribution in the bottle was also studied through the use of Computational Fluid Dynamics (CFD). All the hardware, software (ANSYS Fluent), geometry (axisymmetric), and mesh were identical to those used in our previous study to study the residual heel in consumer bottles [150]. Therefore, the details will not be repeated here. However, a different approach was used in the current work since this time the velocity distribution was of interest. Here, instead of a transient solver coupled with the volume of fluid (VoF) model [40, 150] a steady-state solver with a single fluid was used in each case, since during the discharge process the fluid was always present in the investigated region shown in Figure 4.4, and it was assumed that the process was conducted under pseudo-steady state conditions. The laminar computational model was used here, as before [150]. Ambient pressure was selected as the boundary condition at the upper surface of the bottle. Rather than imposing the desired negative pressure at the computational outlet of the dip tube in Figure 4.4, an average

negative average velocity was used (taken from the PIV measurements) as the velocity boundary condition at the upper level of the dip tube region, i.e., sucking the fluid out from the bottle. No slip boundary condition was applied to all other edges (except to the one located on the axis of rotation). In all cases, the simulation quickly converged in less than 400 iterations. The resulting predicted velocities were then transferred to Tecplot to obtain the contour maps showing the velocity (magnitude) distribution.

4.4 Results

In this section, the effects of fluid rheology, dip tube diameter-to-bottle diameter ratio (d/D), and suction pressure (ΔP) on the discharge hydrodynamics of complex fluids are presented in detail. It should be noted that in order to compare the results obtained with different fluids, all contour maps are reported here using the same velocity color scale (small rainbow scale, ranging from 0 m/s to 0.01 m/s with 11 shades), the only exception being the results for the 16 Silica Paste which had a scale of 0 m/s to 0.001 m/s due to its much lower velocity distribution, as shown below. It is also worthwhile to mention that all the error bars shown in this section represent 95% confidence intervals, and they were obtained by three repetitions of each experiment. Error bars were not added for ROI results, since they were obtained through an analysis of at least 100 averaged image pairs extracted from PIV, which yielded very narrow confidence intervals.

4.4.1 Effect of Fluid Rheology on the Discharge Process and Heel Volume

4.4.1.1 Experimental Velocity Contour Profiles for Newtonian Fluids. Although the main focus of this work was to investigate the discharge of non-Newtonian, complex fluids from dispensing bottles, briefly focusing on the Newtonian fluids could be useful to gain a better

understanding of the hydrodynamics of the discharge process in general, and, most importantly, to have a measure of how the fluid rheology affects the discharge as the fluid complexity (i.e., yield stress, non-Newtonian viscosity, viscoelasticity, etc.) increases.

The velocity contour maps for the Newtonian fluids studied in this work are shown in Figure 4.5. The viscosity of the fluids significantly affected the velocity maps: as the viscosity of the Newtonian fluid increased, the size of the higher velocity zone shown in red in the figure, decreased. While for water ($\eta=0.001$ Pa·s) this zone extended over most of the fluid volume, for sorbitol ($\eta=0.11$ Pa·s) and glycerin ($\eta=0.95$ Pa·s), with progressively higher viscosities, the same zone progressively shrank. It should be noted, however, that the heel volume for Newtonian fluids was always equal to the fluid volume left in the bottle is below the horizontal level of the dip tube orifice (7.86 cm³), i.e., $\Delta V_H = 0$ for this case.

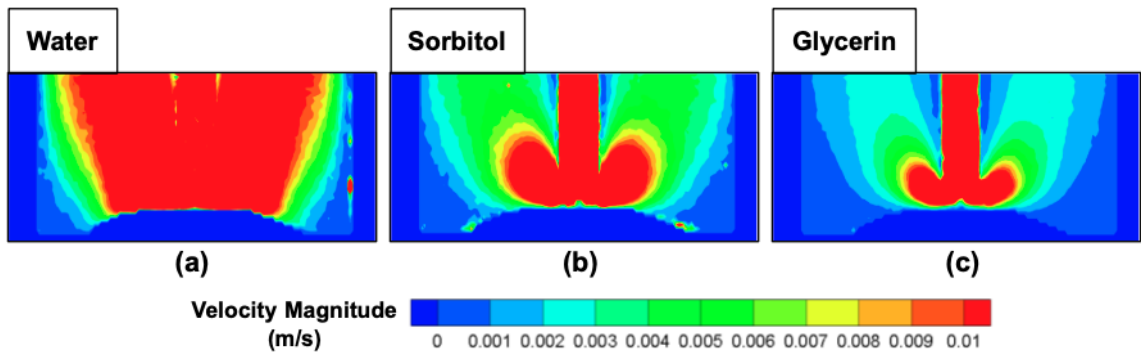


Figure 4.5 Velocity magnitude contour maps for the discharge of the Newtonian fluids studied in this work ($\Delta P=-0.14$ bar, $C=1.75$ mm, $d/D=0.119$): (a) water; (b) sorbitol; (c) glycerin.

4.4.1.2 Experimental Velocity Contour Profiles for non-Newtonian Fluids. The velocity contour maps for non-Newtonian fluids are shown in Figure 4.6. Unlike the results for Newtonian fluids, a slightly asymmetric flow distribution around the dip tube orifice was observed. There are several possible reasons for this phenomenon, possibly associated with the complex nature of these fluids (local viscosity drops, presence of viscoelastic forces). Nevertheless, the impact of the fluid rheology on the zone of higher velocities (in red) can clearly be observed: as the fluid complexity increases, this zone gradually shrinks.

Moreover, compared to the other cases considered here, the relatively higher high-shear viscosity of 8, 11, and 13 Silica pastes can also be observed in the same contour map in Figure 4.6. Accordingly, the red zone *inside* the dip tube was found to be similar for 1.0 Xan, and 1.5 Xan, shrinks slightly for 2.5 Xan, but significantly for the silica pastes, as one can expect from their rheological behavior at high shear rates for these fluids shown in Figure 4.3. These results suggest that a fluid having similar rheology with 11 Silica Paste or 13 Silica Paste may exhibit discharge issues from hand pumps (at least for a -0.14 bar of a suction pressure applied here) because: (1) they exhibit a much larger viscosity at high shear rates resulting in slower flow closer to the dip tube wall; and (2) from a practical standpoint, over time they can result in drying of the residuals on the inner surfaces of the dip tube walls, since the shear generated by the hand-pump is insufficient to either incept or develop the flow in those regions, with a potential long-term failure of the hand-pump.

Figure 4.7a shows the velocity distribution across the selected radial plane on the bottom of the bottle, as previously indicated in Figure 4.4b. One can see that the velocity values decrease as the fluid complexity increases, as expected. Furthermore, for 2.5 Xan and silica pastes, the velocity data are erratic especially for a very low-velocity range (up

to 0.001 m/s), since, as discussed earlier, our PIV system was not able to accurately detect velocities around this range and is therefore prone to errors. It should be noted that for 16 Silica Paste, the velocities were much below the threshold of 0.001 m/s as shown in Figure 4.7a, therefore a different velocity scale (0 m/s to 0.001 m/s) was used. Hence, due to the experimental limitations, a significant amount of error can be seen in its contour plot. Nevertheless, the flow inside the tube was still detectable (Figure 4.6).

Figure 4.7b presents the ΔV_H results for all the rheologically different complex fluids studied here. Overall, it can be seen that the reduced heel volume increased significantly with fluid complexity. The results of Figure 4.7 seem to indicate that as the higher velocity region shrinks during the discharge as a result of the increased complexity of the fluid the corresponding residual heel increases. Therefore, the data in this figure were replotted in Figure 4.8a. This figure clearly shows the inverse linear relationship between ROI and ΔV_H , from which a correlation can be obtained ($R^2=0.86$) as:

$$ROI = 0.97 - 0.08 \cdot \Delta V_H (\text{cm}^3) \quad (4.3)$$

It should also be noted that although the number of fluids studied here is limited, they have significantly different rheology, therefore providing an analysis of ROI for a wide range of rheological behavior.

In Chapter 3, based on the analysis of the CFD results for a variety of different fluids, we reported that the effective yield stress, σ_0 , turns out to be the most statistically significant parameter with the reduced heel volume depending on it via a power law. The experimental data obtained in this work for the seven tested fluids match this dependence

quite closely, see Figure 4.8b in which the dashed line corresponds to this equation.

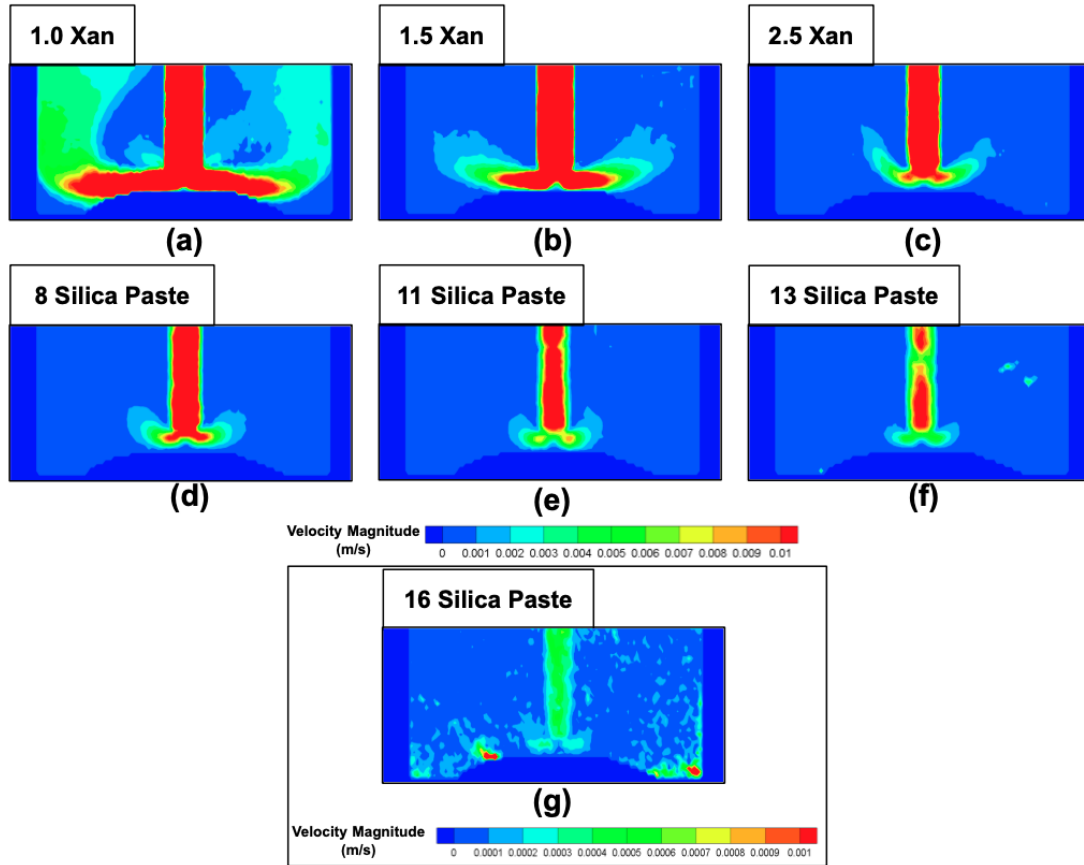


Figure 4.6 Velocity magnitude contour maps for the discharge of non-Newtonian fluids studied in this work ($\Delta P = -0.14$ bar, $C = 1.75$ mm, $d/D = 0.119$): (a) 1.0 Xan; (b) 1.5 Xan; (c) 2.5 Xan; (d) 8 Silica Paste; (e) 11 Silica Paste; (f) 13 Silica Paste, (g) 16 Silica Paste (this panel has a different velocity scale than the other panels).

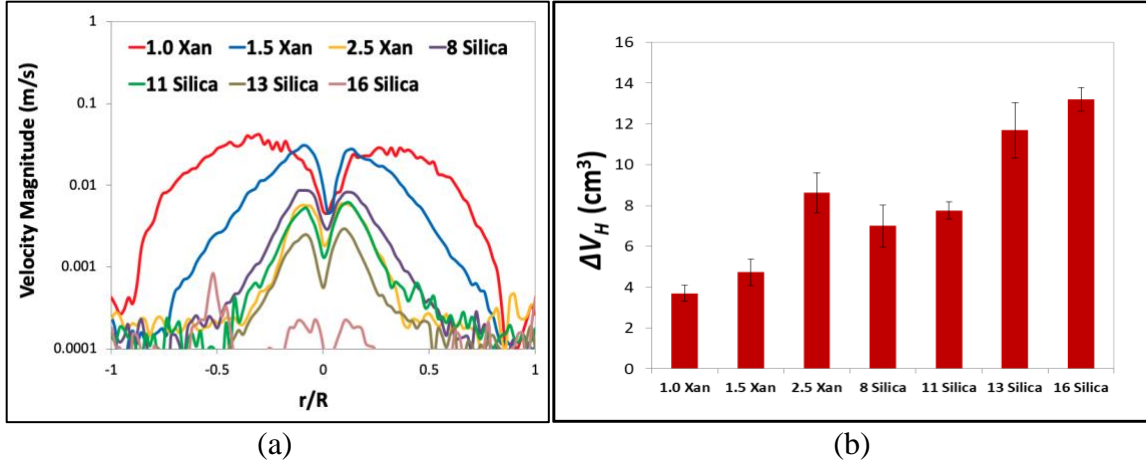


Figure 4.7 (a) Velocity magnitudes on the horizontal plane where the ROI was calculated as a function of the non-dimensional radial position (r/R) for all complex fluids studied in this work ($\Delta P = -0.14$ bar, $C = 1.75$ mm, $d/D = 0.119$). Horizontal dotted line shows the velocity value at which the ROI was calculated ($\bar{v} = 0.001$ m/s); (b) Dependence of the reduced heel, ΔV_H , on fluid rheology for all the complex fluids studied in this work.

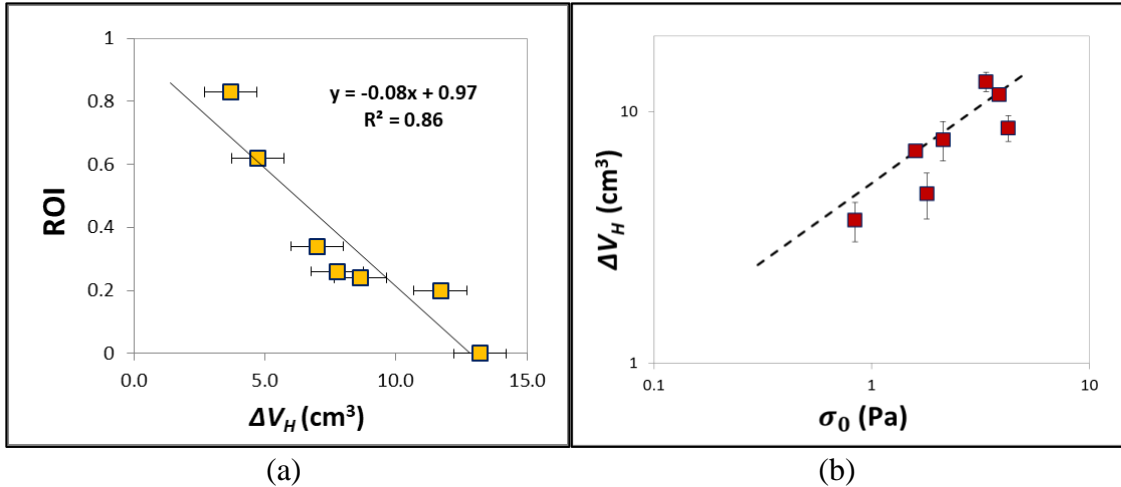


Figure 4.8 Dependence of ROI on the reduced heel, ΔV_H , on the fluid rheology: (a) reduced heel results for all the complex fluids; (b) dependence of ΔV_H on the effective yield stress, σ_0 , of the same fluids. The dashed line shows Equation (3.6), which was derived in our previous work (see Chapter 3) based on a much wider range of fluids using CFD results.

4.4.2 Effect of Tube Diameter Ratio (d/D) at Constant Suction Pressure (ΔP) on the Discharge and Heel Volume

In addition to the fluid rheology, the other important parameters that may alter the discharge hydrodynamics from the same bottle are the tube diameter ratio (d/D), and the suction pressure (ΔP). Figure 4.9 shows the effect of the d/D ratio velocity on the contour maps for three Xanthan fluids (1.0 Xan, 1.5 Xan, and 2.5 Xan), all discharged at a constant suction pressure ΔP of -0.14 bar. While the effect of fluid rheology is still significant, confirming the trend previously presented in Figure 4.8, the tube diameter also plays a critical role: even a 1 mm difference in diameter ($d/D=0.095$ vs. $d/D=0.119$) results in dramatic changes in the velocity flow field, as more material is being discharged out through the larger dip tube at the same suction pressure.

The corresponding profiles of the velocity magnitude on the horizontal plane where the ROI was obtained (0.5 mm off the bottle bump) are presented in Figure 4.10a, Figure 4.10b, Figure 4.10c for the 1.0 Xan, 1.5 Xan, and 2.5 Xan fluids, respectively. Irrespective of the fluid rheology, increasing d/D while keeping the suction pressure constant resulted in higher ROIs. This effect was caused by the larger flow rate in the dip tube requiring that a larger portion of the fluid volume in the bottle be set in motion in order to accommodate the increased discharge rate.

In order to further analyze these results, the ROI was plotted against d/D for all the fluids, as shown in Figure 4.10d. A linear relationship was obtained for each fluid ($R^2=0.99$). It is interesting to notice that at higher d/D ratios the trendline for the 1.5 Xan fluid approached that for the 1.0 Xan fluid, whereas it becomes closer to the trendline for the 2.5 Xan case at lower d/D values. This behavior can be rationalized with the help of rheological curves in Figure 4.3. The higher flow rates generated by the larger dip tube

can be expected to result in higher shear rates throughout the fluid. Figure 4.3 shows that in such a case the high-shear viscosities of the 1.5 Xan fluid and the 1.0 Xan fluid would be very similar, thus resulting in similar ROIs. However, when the shear rate decreases the 1.5 Xan fluid becomes significantly more viscous (Figure 4.3) and the ROI values become intermediate between the 1.0 Xan and 2.5 Xan cases.

Finally, Figure 4.11 shows the dependence of the reduced heel volume, ΔV_H , on d/D for selected rheologically different fluids. As can be seen, increasing d/D decreases the heel volume, as expected. It can also be noticed that the behavior of the data follows a similar pattern to the one in Figure 4.10d.

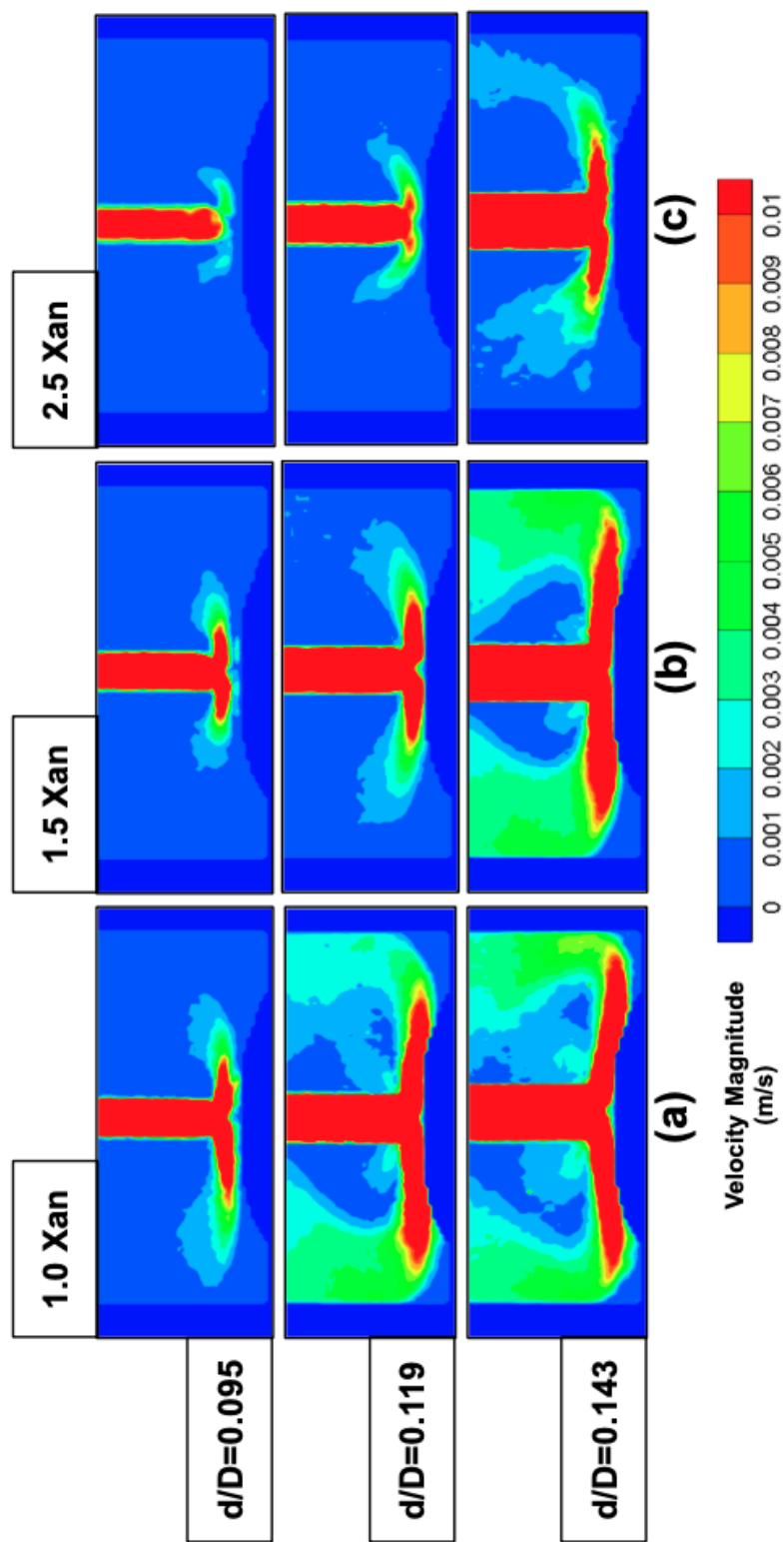


Figure 4.9 Velocity magnitude contour maps for selected complex fluids discharged with different d/D ratios ($\Delta P = -0.14$ bar, $C = 1.75$ mm): (a) 1.0 Xan fluid; (b) 1.5 Xan fluid; (c) 2.5 Xan fluid.

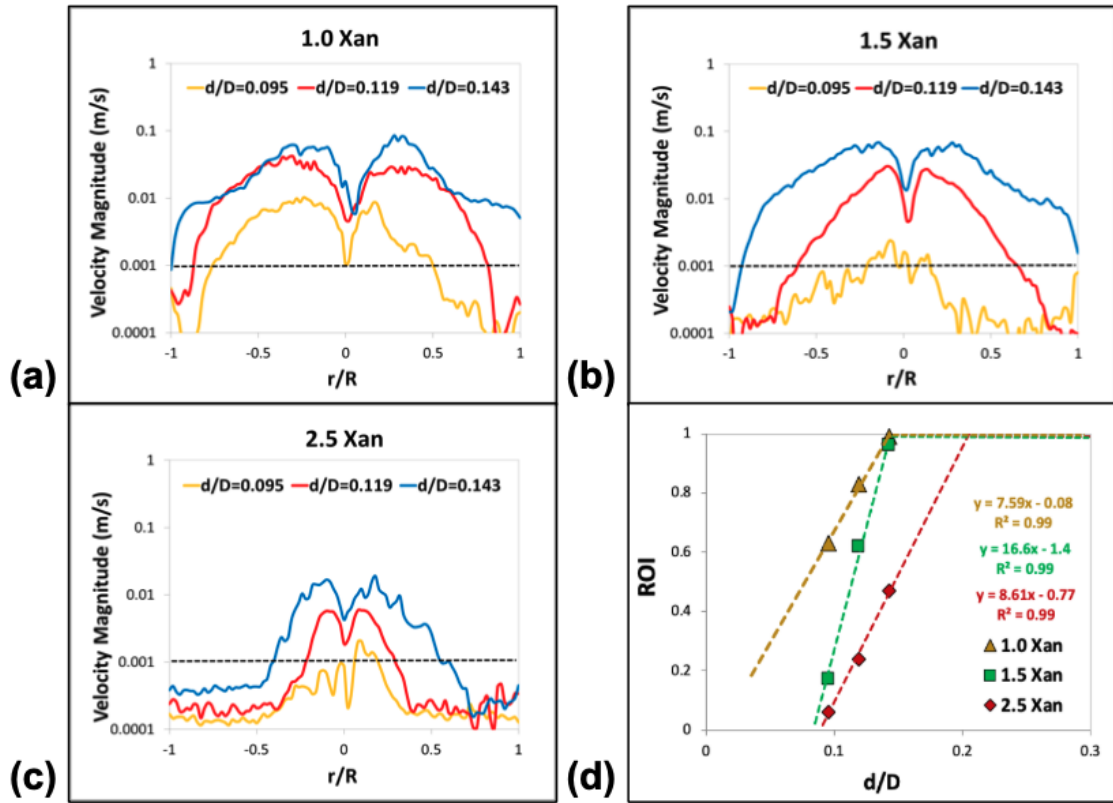


Figure 4.10 Velocity magnitudes on the plane where the ROI was calculated using different d/D ratios but constant ΔP (-0.14 bar) for (a) 1.0 Xan fluid; (b) 1.5 Xan fluid; (c) 2.5 Xan fluid; and (d) dependence of ROI on d/D for the same fluids. Horizontal dotted lines show the velocity value at which the ROI was calculated ($\bar{v}=0.001$ m/s).

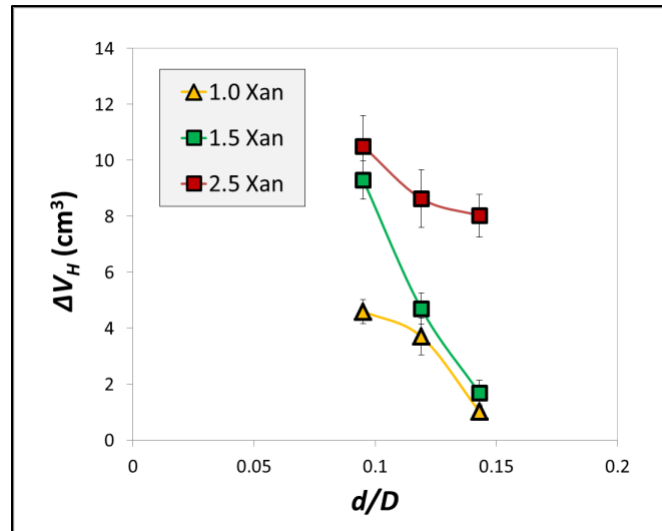


Figure 4.11 Dependence of the reduced heel volume, ΔV_H , on d/D for selected rheologically different fluids ($\Delta P=-0.14$ bar, $C=1.75$ mm).

4.4.3 Effect of Suction Pressure (ΔP) at Constant Tube Diameter Ratio (d/D) on the Discharge and Heel Volume

Figure 4.12 shows the velocity magnitude contour maps for the same complex fluids as in Figure 4.9 but discharged under different suction pressures, ΔP , with the same dip tube ($d/D=0.119$). In each case, increasing the suction pressure significantly increased the ROI. It is interesting to notice that lower pressures created a concave velocity distribution region around the dip tube orifice, which became flatter and more spread near the bottle bottom as the suction pressure increased. In the same figure, it can be seen that for the 2.5 Xan fluid the lowest suction pressure tested here ($\Delta P=-0.07$ bar) was not sufficient to create enough shear to generate measurable velocities near the bottom of the bottle (blue region, where $v < 0.001$ m/s), resulting in $ROI=0$. On the other hand, full fluid motion across the bottle bottom ($ROI \cong 1$) was achieved with fluids with lower viscosities when applying a larger pressure (e.g., 1.0 Xan fluid with ($\Delta P < -0.2$ bar)).

The velocity magnitude on the horizontal plane where the ROI was obtained is presented in Figure 4.13a, 4.13b, and 4.13c for the 1.0 Xan, 1.5 Xan, and 2.5 Xan fluids, respectively. The velocity values on this plane increased as the pressure increased but decreased as the fluid rheology became more complex and the viscosity higher. Note that in Figure 4.13a an additional curve for $\Delta P=-0.045$ bar was added. Figure 4.13d shows a plot of the ROI as a function of ΔP . As one can see, a linear trend was obtained for each fluid ($R^2 > 0.98$). Finally, Figure 4.14 shows the dependence of the reduced heel volume, ΔV_H , on ΔP at constant d/D for selected rheologically different fluids. Unsurprisingly, increasing ΔP decreases the heel volume, and increasing fluid complexity increases the heel volume at a specific ΔP .

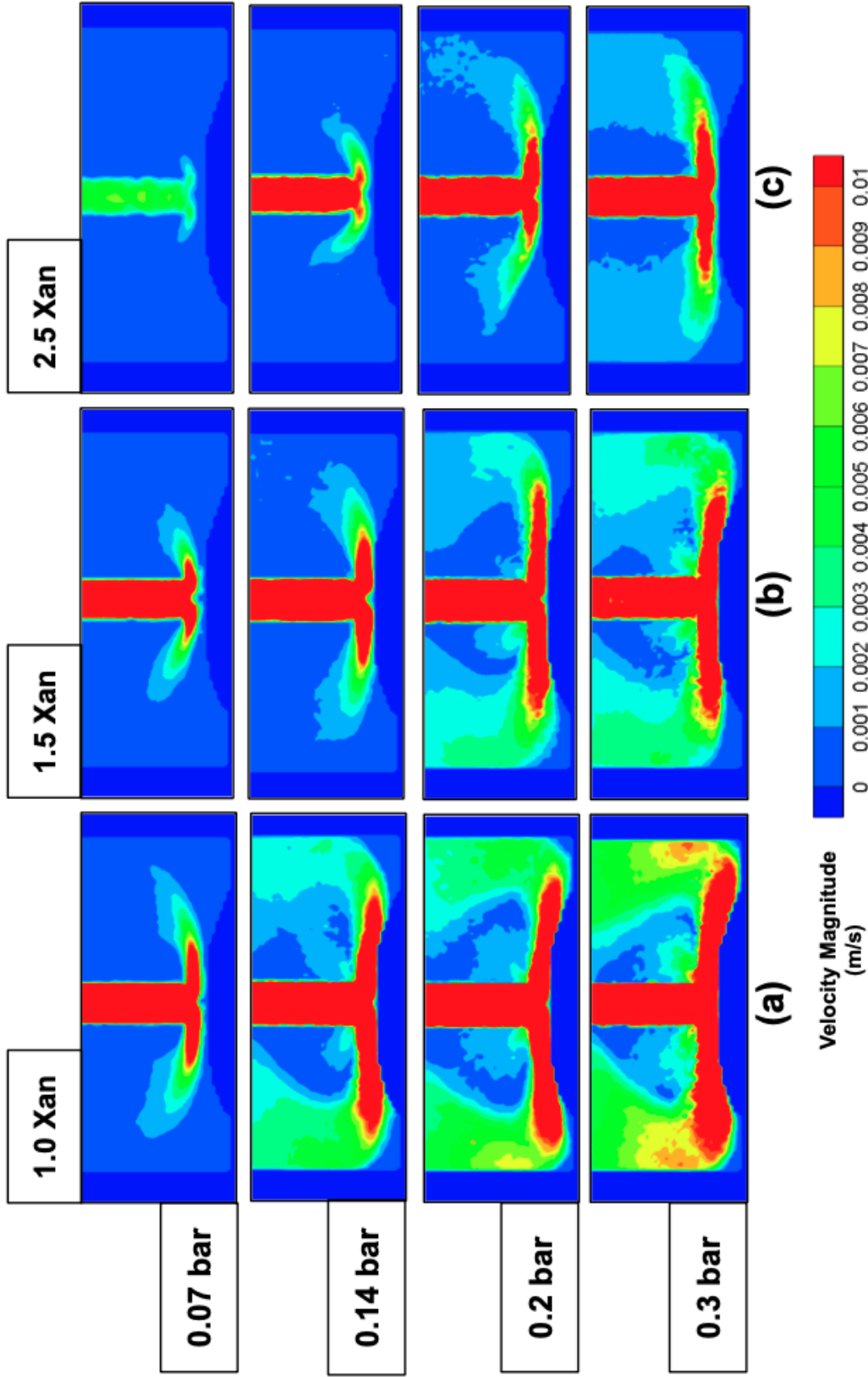


Figure 4.12 Velocity magnitude contour maps for selected complex fluids discharged at different suction pressures, ΔP ($d/D = 0.119$, $C=1.75$ mm): (a) 1.0 Xan; (b) 1.5 Xan; (c) 2.5 Xan.

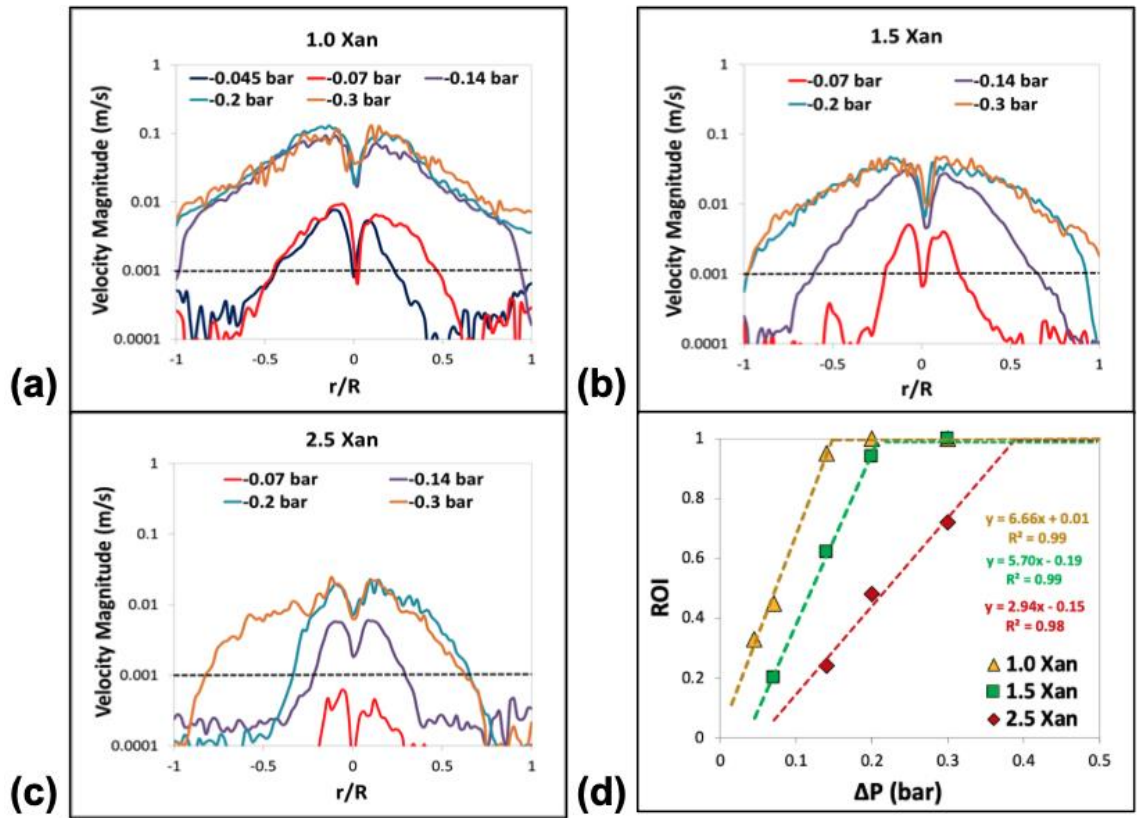


Figure 4.13 Velocity magnitudes on the plane where the ROI was calculated using different ΔP ratios but constant d/D ($=0.119$) for (a) 1.0 Xan fluid; (b) 1.5 Xan fluid; (c) 2.5 Xan fluid; and (d) dependence of ROI on ΔP for the same fluids. Horizontal dotted lines show the velocity value at which the ROI was calculated ($\bar{v}=0.001$ m/s). Note that in Panel (a) an additional profile was added (for $\Delta P=-0.045$ bar).

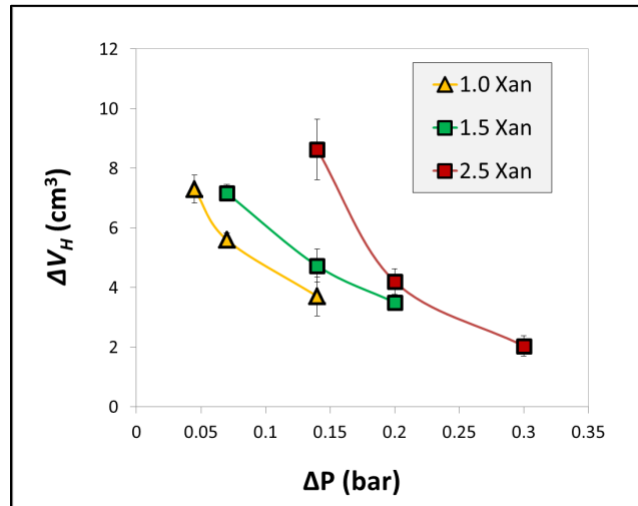


Figure 4.14 Dependence of the reduced heel volume, ΔV_H , on ΔP for selected rheologically different fluids ($d/D=0.119$, $C=1.75$ mm).

4.4 Overall Correlations for ROI and ΔV_H

The results presented here show that increasing fluid complexity, decreasing d/D , and/or decreasing ΔP result in a decrease in ROI and a simultaneous increase in the reduced heel volume. Therefore, an attempt was made to correlate ROI with ΔV_H for different combinations of d/D and ΔP . The results are presented in Figure 4.15. This figure incorporates the results for rheologically different fluids previously presented in Figure 4.8b (yellow symbols), now combined with the results of the experiments with different suction pressures and diameter ratios. Regressing all the data resulted in the following overall correlation ($R^2=0.85$):

$$\text{ROI} = 1 - 0.08 \cdot \Delta V_H \text{ (cm}^3\text{)} \quad (4.4)$$

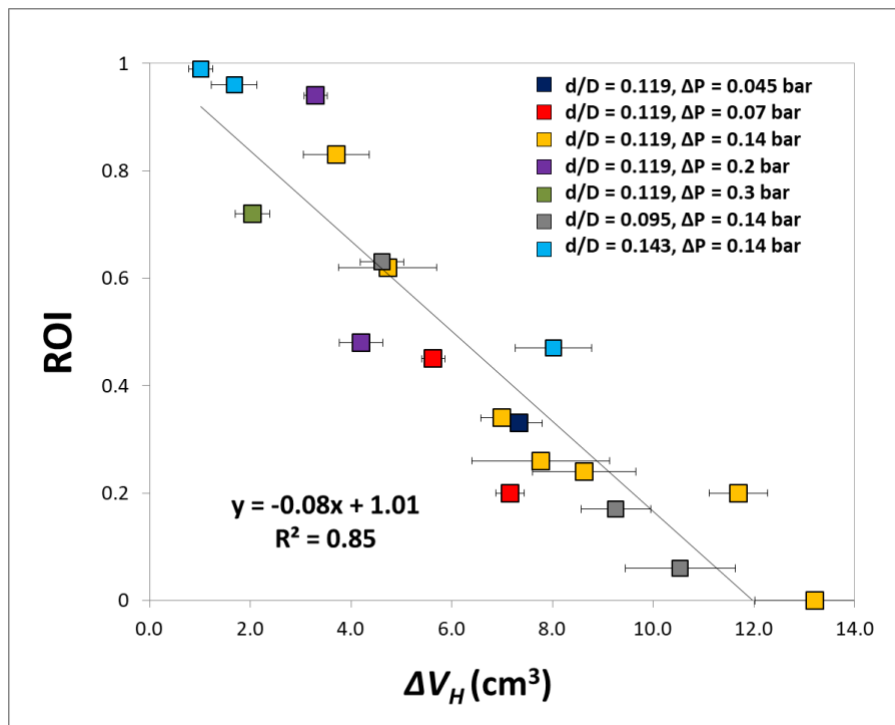


Figure 4.15 Dependence of ROI on the reduced heel, ΔV_H , for rheologically different fluids and with various operating parameters ($C=1.75$ mm). The yellow symbols represent the same results presented in Figure 4.8b.

4.5 Heel Prediction from PIV Experiments and Rheological Data

The relative goodness of the fit (Figure 4.15) over a wide range of fluids and operational parameters supports the claim that the overall motion of the fluid in the bottle (associated with ROI) correlates with the volume of the fluid left in the bottle at the end of the process, i.e., the heel (ΔV_H). This opens the possibility of using PIV results in combination with rheological data to predict the heel. Table 4.2 above has summarized the rheological parameters of the tested fluids while Table 4.3 presents operational parameters for the same fluids and also various test conditions. Recall that all tests were performed in the same bottle of 4.2 cm in diameter (D) but variable tube diameters (d) as well as variable suction pressure which, as one can see, both had a strong impact on the heel. To further characterize the pump operation, the volumetric flow rate, Q , was also measured using PIV data by averaging velocity over the cross-section of the tube. These values are also listed in Table 4.3.

Table 4.3 Operational Parameters

Fluid	ΔV_H (cm ³)	d/D	ΔP (bar)	Flow Rate, Q (cc/s)
1.0 Xan	3.70	0.12	0.14	2.35
1.5 Xan	4.73	0.12	0.14	1.14
2.5 Xan	8.63	0.12	0.14	0.28
8 Silica Paste	7.00	0.12	0.14	0.26
11 Silica Paste	7.76	0.12	0.14	0.13
13 Silica Paste	11.69	0.12	0.14	0.10
16 Silica Paste	13.20	0.12	0.14	0.02
1.0 Xan	7.33	0.12	0.045	0.40
1.0 Xan	5.63	0.12	0.07	0.89
1.5 Xan	7.16	0.12	0.07	0.47
1.5 Xan	3.30	0.12	0.2	1.49
2.5 Xan	4.20	0.12	0.2	0.62
2.5 Xan	2.04	0.12	0.3	1.07
1.0 Xan	4.62	0.10	0.14	0.62
1.5 Xan	9.26	0.10	0.14	0.45
2.5 Xan	10.54	0.10	0.14	0.14
1.0 Xan	1.02	0.14	0.14	5.14
1.5 Xan	1.68	0.14	0.14	3.57
2.5 Xan	8.02	0.14	0.14	0.62

The regression analysis of the data showed that η_∞ , σ_0 , d/D , and ΔP , all play a significant role in heel formation. The resulting correlation for the reduced heel was found by excluding less significant effects (i.e., those with higher p-value) using the backward selection method (using JMP 14 software by SAS Institute) which leaves the following regression equation ($R^2=0.91$):

$$\Delta V_H = 23.9 - 95.1 \cdot \frac{d}{D} - 41.7 \cdot \Delta P + 2.4 \cdot \log_{10}(\eta_\infty) + 6.9 \cdot \log_{10}(\sigma_0) \quad (4.5)$$

where ΔV_H must be expressed in cm^3 , ΔP in bars, η_∞ in Pa.s, and σ_0 in Pa.

One may immediately notice that the tube diameter, pressure drop, and high-shear viscosity have an impact on the heel which appears opposite, at least qualitatively, to what would have been predicted by the Hagen-Poiseuille equation for the volumetric flow rate: $Q \sim \Delta P d^4 / \eta_\infty$. This suggests that the flow rate has a strong negative impact on the heel. Indeed simple single-variable linear regression based on the data in Table 4.3 gives the heel volume as:

$$\Delta V_H = 5.4 - 4.9 \cdot \log_{10}(Q) \quad (4.6)$$

with $R^2=0.84$. In other words, in a situation when one deals with multiple tubes and pressure drops, the flow rate turns out to have by far the most statistically significant impact on the heel: the faster one pumps, the less will be the residual heel. P-values for both models are listed in Table 4.4 and the parity plots are shown in Figure 4.16.

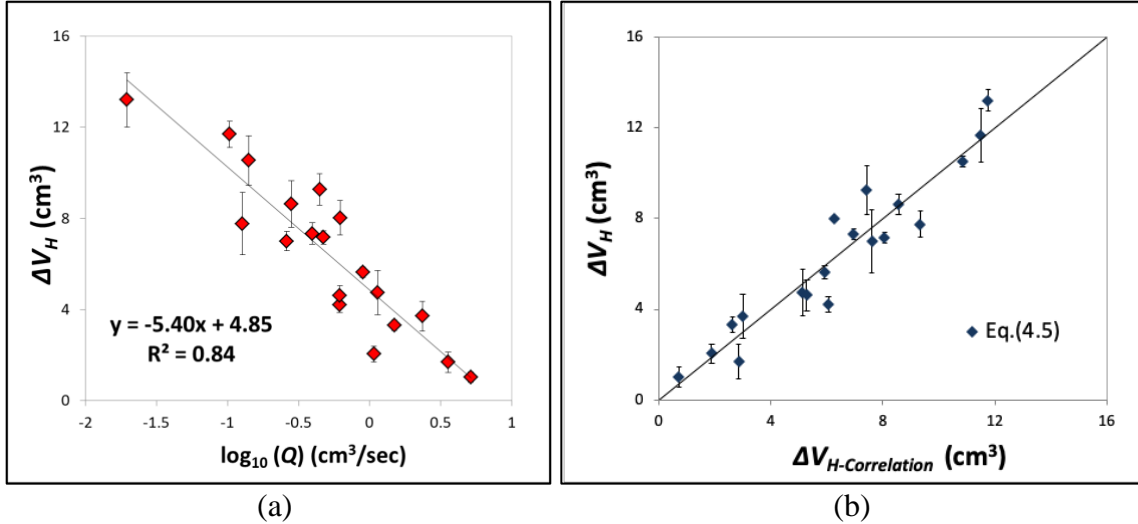


Figure 4.16 Results of statistical analysis: (a) dependence of ΔV_H on the volumetric flow rate according to Eq. 4.6; (b) parity plot for ΔV_H vs. $\Delta V_{H-Correlation}$ obtained using the statistical model represented by Eq. 4.5.

Table 4.4 Prob-t Values for the Effects in Equations (4.5) – (4.6)

	Eq.(4.5)	Eq.(4.6)
$\log(Q)$	N/A	<0.0001
ΔP	<0.0001	N/A
σ_0	<0.0001	N/A
η_∞	<0.0001	N/A
d/D	0.0002	N/A
R^2	0.91	0.84

4.6 Computational Results and Comparison with PIV

Figure 4.17 shows a comparison between the experimental velocity contour plots obtained by PIV and the corresponding predictions of the CFD simulations. For the Newtonian fluids, i.e., sorbitol and glycerin, the visual agreement can be observed to be appropriate, indicating high accuracy of the CFD approach can reliably be used to determine the flow.

However, for Xanthan gum gels, the agreement was poor. While PIV measurements show a flow more spread towards the bottle walls, especially for the fluids with low Xanthan concentration (as for the 1.0 Xan case), the simulation prediction showed a higher velocity region around the dip tube.

The agreement was slightly better for 2.5 Xan and significantly better for silica pastes. Since the velocity values for 16 Silica Paste were all below 0.001 m/s, which is the threshold for ROI (therefore ROI=0 in this case), the contour maps are presented using a different scale (0 to 0.001 m/s). As a result, they possibly included significant experimental errors. However, the results were still somewhat comparable to CFD simulations considering the level of complexity of this fluid.

The results of Figure 4.17 are also confirmed more quantitatively in Figure 4.18, where a comparison between the computationally predicted ROI and the corresponding experimental values is presented (the results for the 16 Silica Paste are not included since the ROI was equal to 0 for both PIV and CFD). One can see that the CFD predictions of the ROI were in close agreement with the experimental results for all yield stress fluids, such as highly polymer concentrated gels and silica pastes, whereas the agreement between the simulations and experiments worsens as the fluid complexity decreased.

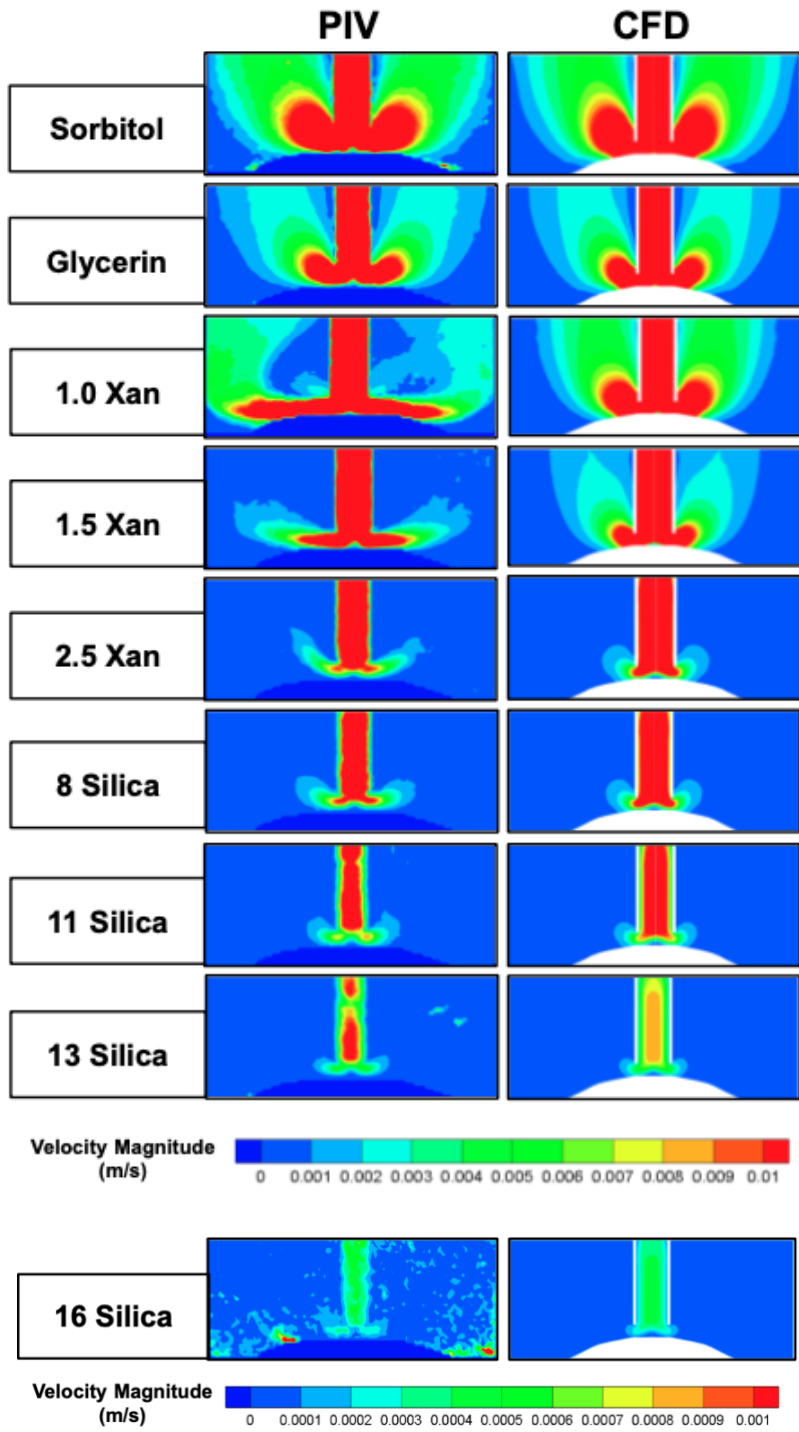


Figure 4.17 Comparison of computationally predicted (CFD) and experimentally determined (PIV) velocity magnitude contour maps.

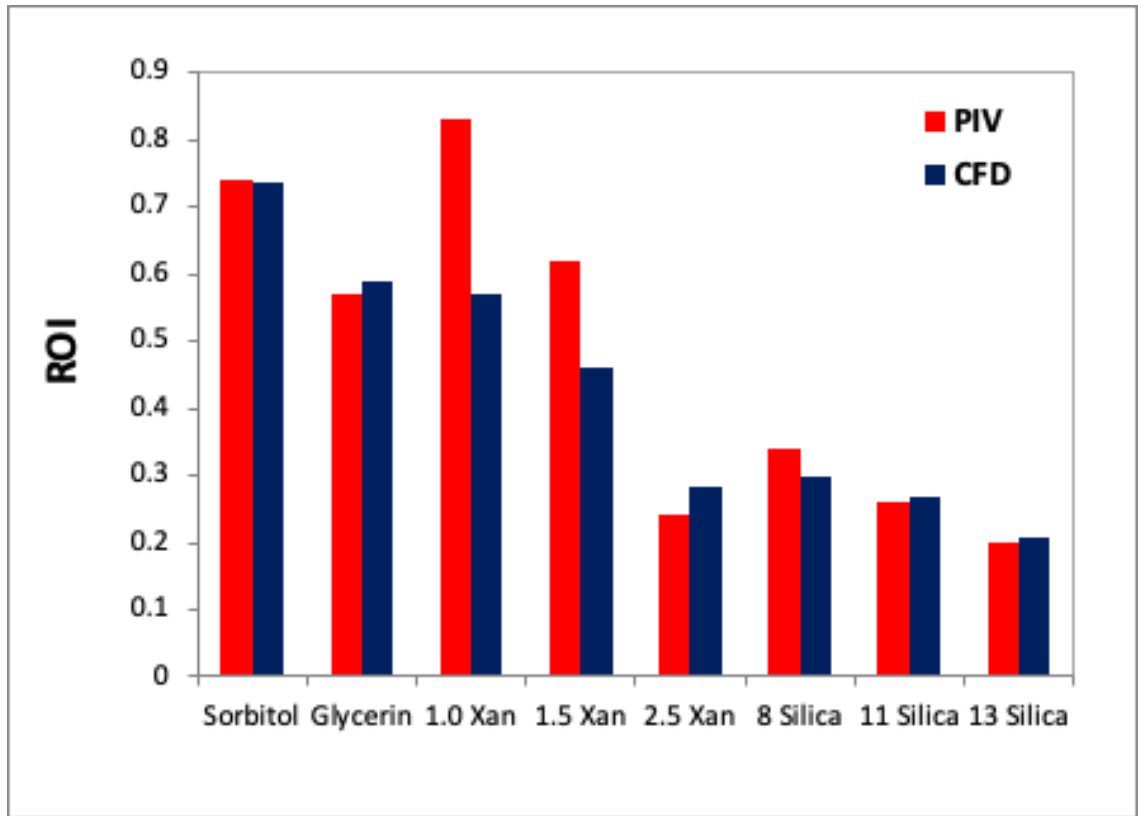


Figure 4.18 Comparison of computationally predicted (CFD) and experimentally determined (PIV) ROI. Note that the ROI results of 16 Silica are not shown since they were both 0.

4.7 Discussion

The results presented above show that the discharge hydrodynamics of complex fluids from consumer dispensing bottles can be effectively determined by using PIV. Overall, it was found that the flow characteristics *during* the discharge determine the heel volume *at the end* of the discharge. The former aspect of the process, i.e., flow during the discharge, was quantified using the *Region of Interest (ROI)*, which captures the relative size of the high-velocity region during the discharge and therefore represents a *dynamic* state. Conversely, the latter aspect of the process, i.e., the reduced heel volume at the end of the discharge (ΔV_H) corresponds to a *static* state. Despite the contradicting nature of both phenomena, it

was found that the complex rheology of the fluid, the suction pressure (ΔP), and the tube-to-bottle diameter ratio (d/D) all impact both aspects of the discharge process, while ROI and ΔV_H appear to correlate well with each other for a wide range of suction pressures, diameter ratios, and fluid rheology ($R^2=0.85$). Thus, if one wants to minimize the heel in the dispensing bottles, the ROI has to be maximized by fine-tuning ΔP , dip tube diameter, and the rheological properties of the fluid.

In general, as the fluid became more rheologically complex (e.g., by increasing the solids concentration in pastes), lower ROI values and higher ΔV_H were obtained, whereas the ROI increased and ΔV_H decreased with increasing d/D (at constant ΔP) and ΔP (at constant d/D) irrespective of the fluid rheology. These observations lead to the speculation that any rheological, geometric or operating parameter that results in the strongest velocities across the largest possible cross-section of the container near the suction point (thus resulting in higher ROI values) will reduce the heel volume. In this work, we only examine the role of a few of these parameters, but the possibility of using other ways to accomplish a similar objective (such as modifying the location of the dip tube orifice, changing the shape and size of the bottle, or introducing any fluid slippage on the bottle walls, e.g., by using LiquiGlide (www.liquiglide.com), remains open and worth pursuing in future investigations.

Essentially, one can investigate the discharge of fluids from a dispensing bottle by using *any* flow monitoring technique, measure ROI, and optimize the shape of the bottle (e.g., reducing the internal diameter or the curvatures) so as to alleviate all the regions in which the flow is not impactful, and that contribute to the heel formation. The PIV technique used for this purpose in this work is one of the methods with the highest velocity

resolution among those used to quantify fluid hydrodynamics. However, PIV requires the use of transparent fluids, and this can be a limiting factor for many complex fluids. Here we were able to circumvent this problem using the refractive index matching method [8], which we successfully applied even to highly silica-concentrated pastes. Alternatively, however, one could formulate a transparent fluid with similar rheological parameters to the ones of the opaque fluid of interest, and do the analysis described above. Although this approach is somewhat time-consuming and would require extensive experimentation, it may still be used especially if other flow monitoring techniques for opaque systems (e.g., MRI) are not present.

CFD has become a powerful and ubiquitous tool to study the hydrodynamics of many different systems [37, 90, 103, 109, 113, 151]. In this work, we found that CFD adequately predicted the velocity distribution and the ROI for some systems but not others. Specifically, CFD appropriately predicted the ROI for the Newtonian fluids and the silica pastes studied here but only fairly for the Xanthan fluids. In other terms, the agreement between the simulations and the experiments worsened as the fluid complexity decreased, as shown in Figure 4.18. We can only speculate why this happened: the effective yield stress might be the rheological parameter that primarily controls the flow of highly concentrated gels and pastes. However, for fluids having a low or no yield stress, such as some of the Xanthan fluids studied here, the viscoelastic forces may become the dominating ones. On the other hand, the CFD model that we employed here was based on the use of the Carreau model, a generalized Newtonian model that does not account for the viscoelastic forces. Therefore, it seems reasonable to conclude that the CFD simulations with a steady solver might have failed to accurately describe the hydrodynamics of those

fluids in which the viscoelastic forces became dominant. This hypothesis is further supported by the velocity contour maps shown in Figure 4.17. The experimentally obtained contours show that the higher shear region (shown in red) was typically “choked” below the tube orifice level, presumably by the local elastic forces, creating a pseudo-wall blocking the fluid entrance from the closer sides of the orifice and primarily enabling the suction action to occur from the direction of the bottle walls. By contrast, in the CFD simulations, this behavior was not predicted, and the flow appeared to be less restricted, as for the case of 1.0 Xan, for which significant fluid motion was predicted to occur closer to the dip tube.

Since the correlation between the experimental ROI and heel is significant (Figure 4.15), one may think that CFD simulations would overestimate not only the ROI but also the heel volume for Xanthan fluids with lower Xanthan concentrations. However, this was not the case, as reported in our previous study [150]. It is therefore apparent that while the determination of the heel volume using the transient simulations based on the Carreau model works fine for a wide range of fluids, the prediction of ROI using the steady-state solver did not work well for low-complexity fluids. Since the effective yield stress is the dominating parameter in the heel formation, which is a *static* process, it is reasonable that the Carreau equation itself (i.e., without an additional model describing viscoelasticity) sufficed to accurately predict it [150]. Conversely, the steady-state simulations and the ROI analysis correspond to the *dynamic* (continuous) state, in which case the viscoelastic properties may not be negligible. This observation seems to suggest that in order to increase the accuracy of ROI prediction for the fluids having low or no yield stress, more complex CFD models should be used, possibly including the viscoelastic and extensional

properties of those gels. This is clearly a topic for future investigations.

Finally, the three operational parameters, d/D , ΔP , and Q , and the rheological parameters, η_∞ and σ_0 , were all found to be statistically significant as far as heel formation is concerned. This enabled us to build a statistical correlation (Equations 4.5) that adequately predicts the heel for the systems studied here.

Clearly, this correlation, or similar types of correlations, will still need to be confirmed and/or refined by more experiments with other systems. Among these two rheological parameters, σ_0 was previously found to be the dominating parameter for the heel formation [150], although in that work only the fluid rheology effects were investigated while all other operational and geometric parameters were kept constant. Therefore, it is not surprising that here we found that η_∞ also played a role when parameters such as suction pressure and diameter ratio were varied, as both parameters would directly impact the flow in higher shear regions, i.e., the dip tube region and the region close to it.

Overall, Equation (4.5) might be useful, especially for product packaging developers and formulation scientists as it enables the quantification of the heel by fine-tuning the operational parameters as well as the formulation of the liquid product of interest. Therefore, we expect that this work will be of interest to those who work with systems similar to those studied here.

4.8 Conclusions

From this work, the following conclusions can be made:

- The rheology of the fluid, and operational and geometric parameters such as the suction pressure generated by the pump (ΔP), tube-to-bottle diameter ratio (d/D), and volumetric flow rate (Q), all significantly affect the discharge hydrodynamics of complex fluids from dispensing bottles;
- PIV can be used to monitor the discharge hydrodynamics in highly concentrated gels and pastes, provided that the fluid and the container are both transparent;
- The Region of Influence (ROI) defined in this work is a useful parameter to quantify the size of the region of the fluid in the bottle that is set in motion during the fluid discharge, which, in turn, is inversely correlated to the heel;
- CFD simulations based on the Carreau model are another approach that can be used to predict the discharge behavior of complex fluids for fluids whose rheology is adequately described by this model. More comprehensive models including extensional and other viscoelastic forces will be needed to accurately predict the hydrodynamics in the fluids having low or no yield stress.

CHAPTER 5

EFFECT OF DIP TUBE ORIFICE SHAPE AND CLEARANCE ON DISCHARGE HYDRODYNAMICS AND RESIDUAL HEEL VOLUME IN DISPENSING BOTTLES USING PIV

5.1 Abstract

In this work, the role of the dip tube shape and clearance on the hydrodynamics during the complex fluid discharge from dispensing bottles, and on the resulting residual “heel” volume was investigated. To monitor the flow and the heel, Particle Image Velocimetry (PIV) was used. Accordingly, the dip tube clearance and the orifice shape both affect the formation of the heel. As will be shown, having a flat cut dip tube orifice not only leaves less heel compared to angled cut orifices but also results in a higher flow rate at constant suction pressure. In addition, lowering the dip tube clearance reduces the heel irrespective of the dip tube orifice shape. The results of this work were qualitatively validated using the velocity contour maps obtained by PIV, and, separately, with the heel profiles obtained based on the PIV raw images.

5.2 Introduction

The discharge of non-Newtonian, complex fluids is a ubiquitous but often problematic process due to the complex rheology of such fluids that can partially or totally prevent their flow and also result in residual fluid (*heel*) left in the container at the end of the discharge process [4, 5, 40, 132, 150]. The formation of the heel is undesired and important not only in industrial vessels [30, 40] but also in consumer packaging, albeit the latter issue has not received much attention, as discussed elsewhere [132, 150].

Among consumer packaging systems, dispensing bottles operating with a hand pump are highly relevant and commonly used as containers for a variety of personal and oral care products, such as lotions, gels, shampoos, soaps, and many other complex fluids [1]. In such systems, the fluid is discharged through a dip tube inserted in the bottle. As the hand pump head is depressed, the fluid in the pump housing is discharged. When the pump head is released, the pump starts to recover to its initial position and sucks up fluid up into its housing, thus preparing the hand pump for the next pumping action. It is clearly highly desirable to understand the hydrodynamics in these systems in order to provide better designs of dispensing systems that result in improving the discharge by increasing the pump recovery rate while minimizing the amount of residual heel.

There are several parameters that may impact the hydrodynamics in dispensing bottles, such as bottle geometry, suction pressure, dip tube shape, diameter, and the off-bottom clearance. Although critical for the functionality of the dispensing system, the effect of these geometric and operational parameters on the discharge of complex fluids from such systems has not yet been investigated. In fact, a literature review shows that only a few attempts have been made to investigate the orifice geometry and fluid rheology

on the discharge of complex fluids through orifices of vessels and pipes [17, 19, 29, 31, 33, 35]. Nevertheless, there has been a lack of insightful information for more complex systems such as dispensing bottles, from which the fluid is discharged through the dip tube under a differential suction pressure. Recently, our research group has reported results obtained both experimentally, via Particle Image Velocimetry (PIV), and computationally, via Computational Fluid Dynamics (CFD), to quantify and predict the heel volume [150]. Accordingly, we showed that the rheological properties of the fluids significantly affect the heel profile and the volume. However, how other parameters such as dip tube orifice geometry that would impact the discharge hydrodynamics and the residual heel volume remained uninvestigated.

Therefore, in this work, we investigate the effect of the dip tube orifice shape and clearance on the hydrodynamic characteristics of the dispensing systems, and, consequently, on the formation of the heel. To do so, we used a gel consisting of a mixture of xanthan gum, glycerin, and water, which forms the basis of most commercial liquid products for consumer products [7]. Here, Particle Image Velocimetry (PIV) was used as the primary tool to monitor the flow during the discharge process and to determine the shape of the residual heel thereafter while a weighing method was employed to quantify the heel mass and volume. We found that larger dip tube orifice clearances resulted in larger heel volumes, and, more importantly, that using a flat cut orifice significantly reduces the heel while providing the highest volumetric flow rate during the discharge, as opposed to the more commonly used angled cut alternatives.

5.3 Experimental Equipment, Materials, and Method

5.3.1 Experimental Equipment

Mixer. The fluid was prepared using a Whip Mix WPM2 mixer (Whip Mix Corp., Louisville, KY). This mixer provides a vacuum during the mixing, which minimizes the number of air bubbles in the fluid that results in reflections of light, as discussed earlier in this work (Chapter 2).

Centrifuge. The test fluid studied here was centrifuged at 3000 RPM for 3 minutes using an Eppendorf Centrifuge 5804 (Thermo Fisher Scientific, Waltham, MA) before the experiments.

Vacuum Pump. A GAST DOA-P704-AA vacuum pump (GAST, Benton Harbor, MI, USA) was used to generate the desired suction pressure to allow the fluid in the bottle to be discharged from it.

Manometer. A Traceable® digital manometer (VWR International, Pennsylvania, USA) was used to set the suction pressure to the desired value. All the pressure measurements were taken at the orifice of the dip tube with the dip tube removed from the bottle.

Test Bottle and Tubing. The test bottle used here was identical to the one used throughout this work, therefore the geometric details will not be repeated here. The suction pressure was set at -0.135 bar. The dip tube had an inner diameter, d , of 4 mm, and an outer diameter, d_o , of 6 mm. The off-bottom clearance of the tube, C , was varied in each experiment. The dip tube orifice clearances studied here were 0.5 mm, 1 mm, and 2 mm, which correspond to the vertical distance from the peak of the dimple of the bottle to the lowest point of the dip tube orifice curvature.

Particle Image Velocimetry System. The PIV laser unit used in this work was identical to the one presented in detail in Chapter 3.

5.3.2 Materials

Fluid. A 0.5 wt. % xanthan gum gel was used in this work. The preparation procedure of this gel was as follows: First, with a help of an overhead mixer, xanthan gum was dispersed in glycerin. Then, the balance water, also containing the stock tracer solution (10 mL) described below, was added. The exact composition of the fluid was as follows: 0.5 wt.% xanthan gum, 49.75 wt. % glycerin, and 49.75 wt. % water. This mixture was then transferred to the WhipMixer in which it was further mixed for 4 minutes under vacuum.

Tracer Particles. Red fluorescent polyethylene particles (Cospheric, CA, USA) with a particle size of 10-45 μm and a density of 0.995 g/cm^3 were used in this work, as before. The preparation of the tracer particle solution was also identical to the procedure described in detail in Chapter 3.

5.3.3 Methods

Method 1: Experimental Determination of the Velocity Distributions Using PIV. Obtaining the velocity distributions during the continuous pumping consisted of three steps: (1) the bottle was completely filled with the gel; (2) the vacuum pump was turned on; (3) the PIV system started to collect pairs of images at 8 Hz as the bottle was being drained. The time interval between images for each image pair was as low as 400 μs to capture the flow by preventing the particles to escape their interrogation windows. The size of the interrogation windows was 16 \times 16 pixels.

The fluid was discharged from the test bottle to another empty container until the

discharge ends, i.e., no more fluid was being sucked up into the tube. Only the region corresponding up to 20 mm height of the bottom portion of the bottle (the region marked in yellow in Figure 5.1) was optically monitored. Hence, the image pairs having a liquid level below 20 mm height (towards the end of the discharge) were discarded. The PIV analysis was conducted in the region marked with dashed black lines in Figure 5.1. Outside this region, there was either no fluid present or significant light reflection was observed due to the curvatures of the bottle. Hence, outer regions were masked.

After the images are collected, the noise was determined using the “*Image Min/Max*” technique of the Dynamic Studio software (Dantec Dynamics, Denmark), which determines the intensity of the image by calculating the power mean pixels in all the collected image pairs (see Dantec manuals). The noise was removed from the original images using the “*Image Arithmetic*” option, and the “*Adaptive PIV*” function was applied to obtain the spatial displacement of the particles hence the velocity of the fluid at each location, as described previously in detail [84]. After the PIV analysis was completed, the data was exported to Tecplot® software (360 EX 2018 R2), where the velocity magnitude contour maps were obtained.

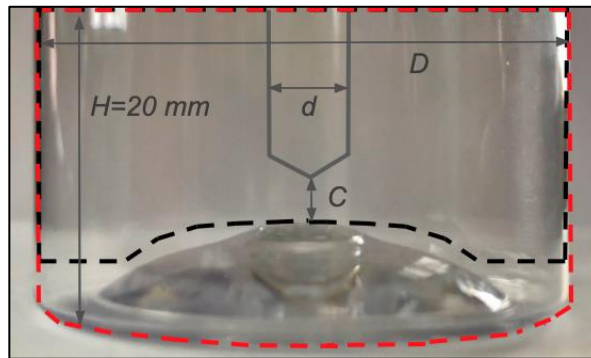


Figure 5.1 Portion of the bottle that is optically monitored. Note that the black dashed lines represent the region analyzed by using *Method 1*, whereas the red dashed lines represent the region analyzed by using *Method 3*.

Method 2: Determination of Volumetric Flow Rate of the Discharged Fluid in the Dip Tube Using PIV. The volumetric flow rate was calculated using PIV for various orifice shapes at the lowest clearance studied here ($C=0.5$ mm). To do so, a similar procedure presented in a previous study was used here [152]. More specifically, the velocity values on the upper circular area of the dip tube, i.e., the inner radial plane at the top of the tube in the investigated region (Figure 5.1) were integrated along the inner diameter of the tube using well-known equations (see Equation 1 in [152] and the detailed explanation therein).

Method 3: Determination of the Shape of the Heel Using PIV Imaging Method. This method is based on capturing the image of the instantaneous heel, i.e., the heel profile in the bottle at the moment air enters the tube, and concluding the discharge process. Accordingly, the bottle was filled up to 20 mm in height from the bottom, the vacuum pump was turned on, and the PIV system started to take images. The heel profile on the image taken when the discharge ends were treated as the instantaneous heel profile. This raw PIV image was then processed using the ImageJ software [138], in which the background noise was subtracted (with the “light background” option on) based on the rolling ball algorithm, which estimates the background intensity of a grayscale image in case of an uneven exposure and subtracts it from the original image [139, 140]. This method was used here for better visualization of the heel profiles by creating a bigger contrast between the fluid and the remainder of the image.

Method 4: Determination of the Heel Volume Using Weighing Method. Separate experiments were conducted to quantify the heel volume. The bottle with the modified hand pump dip tube inside was filled up with the fluid, and the vacuum pump was turned

on. The vacuum pump was shut off once the discharge was finished and the air began to enter the dip tube. The bottle was taken off the modified hand pump and weighed. Knowing the mass of the empty bottle allowed for the calculation of the heel mass. Finally, the heel mass was transformed into its volume using the fluid density as a reference.

5.4 Results and Discussion

Figure 5.2 shows the results of the velocity magnitude contour maps and the heel profiles. It is apparent that the velocity contours are quite different depending on the orifice shape. While the flow around the orifice is approximately symmetrical, the one angled cut orifice generates an asymmetric flow, with the fluid being primarily sucked into the dip tube only from the side where the orifice is cut at an angle. Conversely, symmetric flow distribution around the orifice was observed for the two angled cut orifice. These results show that the shape of the orifice strongly affects the velocity profiles.

Furthermore, one may notice that while the flow does not “spread” onto the entire bottom of the bottle for both angled orifices, a flat cut orifice with the same clearance results in a flow distribution that fully sweeps the bottle bottom. Figure 5.2 also presents the heel images obtained with the PIV imaging method. These clearly show that the heel shape profiles, and therefore the heel volume, are also affected by the shape of the orifice, the smallest heel being qualitatively associated with the flat cut orifice. It is also interesting to notice that the shape of the flow *during* the discharge process determines the heel profile *after* it. This is especially significant for the one angled cut orifice at low clearances since the fluid flows into the dip tube primarily from one side of the bottle while the heel tends to form mainly in the region opposite to it because of the lower end of the orifice on this

side, obstructing the flow into the tube.

Not only the orifice shape but also the dip tube clearance plays a role in the discharge hydrodynamics. Figure 5.2 shows that as the clearance increases, the asymmetry in the velocity contour maps decreases together with the asymmetry in the heel profile. This is partially true even for the one angled orifice since higher clearances allow at least some portion of the fluid to enter the tube also from the side opposite to the slanted cut opening of the orifice.

Increasing the clearance also results in an increase in the heel for all orifice types. This occurs not only because a higher location of the orifice results in the fluid being able to be sucked into the tube only until the (now higher) tube end is submerged (even a Newtonian fluid would result in a higher heel in this case), but also because the flow distribution during the discharge process is less capable of sweeping the bottom of the bottle (Figure 5.2), thus contributing the formation of a larger heel once air begins to be entrained in the dip tube and the discharge process stops, “freezing” the fluid at the bottom at that location.

Further reducing the clearance of the flat cut orifice will eventually choke completely the dip tube when $C=0$ mm. However, one should consider the possibility that placing a flat cut orifice at a very low clearance could, possibly, result in a partial fluid blockage of the orifice especially for yield-stress and/or highly viscoelastic fluids, as the fluid may not have enough clearance to enter the tube. To study this hypothetical phenomenon was beyond the scope of this work, but even in this study a partial blockage could actually be detected by carefully observing the first contour map in Figure 5.2 ($C=0.5$ mm, flat cut orifice), in which a less smooth velocity profile was obtained since the fluid

became “choked” between the tube orifice and the bottle dimple. Nevertheless, as far as the fluid studied here is concerned (0.5 Xan), this did not prevent the discharge, and actually resulted in a smaller heel compared to all other cases studied here.

In order to better understand these effects and minimize the clearance to the lowest possible value, we looked at the one angled orifice for $C=0$ mm since this orifice can operate even under this condition. The velocity results and the heel profile are shown in Figure 5.3a. In this case, the flow is essentially limited to one side of the orifice and nearly the entire right-hand portion of the bottom of the bottle is swept by it. Figure 5.3b shows that the flow is particularly strong in the neighborhood of the slanted opening of the orifice. This figure additionally shows that the flow intercepts the upper corner of the orifice prior to entering the tube, generating a circulation loop that results in significant momentum loss, as the velocity map in Figure 5.3b clearly indicates. As for the heel formation for this case, the high velocity on the right-hand side of the bottle, effectively sweeps the bottom surface of the bottle, minimizing the heel on that side, and leaving a significant heel volume on the unswept on the left-hand side.

The results presented so far indicate qualitatively that in all cases the flat cut orifice appears to be superior to both angled orifices as far as flow maximization and heel minimization are concerned. In order to *quantitatively* confirm this conclusion, the heel volume was determined using the weighing method (*Method 4*) and plotted as shown in Figure 5.4. The heel volume increased with increasing clearance irrespective of which orifice shape was used, as one would expect. More interestingly, the heel volume for the flat cut orifice was found to be always smaller than for the angled orifices. This can also be partially expected, given that even for the same clearance C (measured from the top of

the bump to the lowest point of the orifice) the actual distance from the bump at which air would start to be entrained at the end of the discharge process would be equal (at least for a Newtonian fluid) to C for the flat orifice, $C + \sqrt{2} \cdot d_o - \sqrt{2}(d_o - d)/2$ for the one angled orifice, and $C + \sqrt{2} \cdot d_o/2 - \sqrt{2}(d_o - d)/4$ for the two angled orifice. In addition, since the flow profile during the discharge process was shown here to also affect the final shape of the heel, orifices such as the one angled orifice that are not capable of generating a stronger flow near the bottom of the bottle would produce a larger heel irrespective of the level at which air starts being entrained. In summary, the flat cut orifice always results in a minimal heel compared to angled cut orifices.

A relevant question is whether minimizing the heel by modifying the orifice shape and clearance may have a detrimental impact on the flow rate during the discharge process. Higher volumetric flow rates are often desired to rapidly fill the upper housing of the hand pump and prepare the dispensing system for the next pumping action, as mentioned earlier. To address this question, the flow rates for each case were calculated by using *Method 2*. Figure 5.5 presents the volumetric flow rate for each orifice shape at $C=0.5$ mm and shows that the volumetric flow rate in the tube with flat cut orifices was 110% higher than that for the one angled cut orifice and much higher (240%) than that for the two angled cut orifices.

It is also noteworthy to briefly discuss the industrial applicability of the orifices studied here. In industrial practice, in fact, angled cut orifices are more commonly used than flat cut orifices. The advantage of the angled cut orifices over a flat cut orifice is their ability to pick up the fluid from very low clearance, i.e. $C=0$ mm or slightly higher, while preventing any flow blockage.

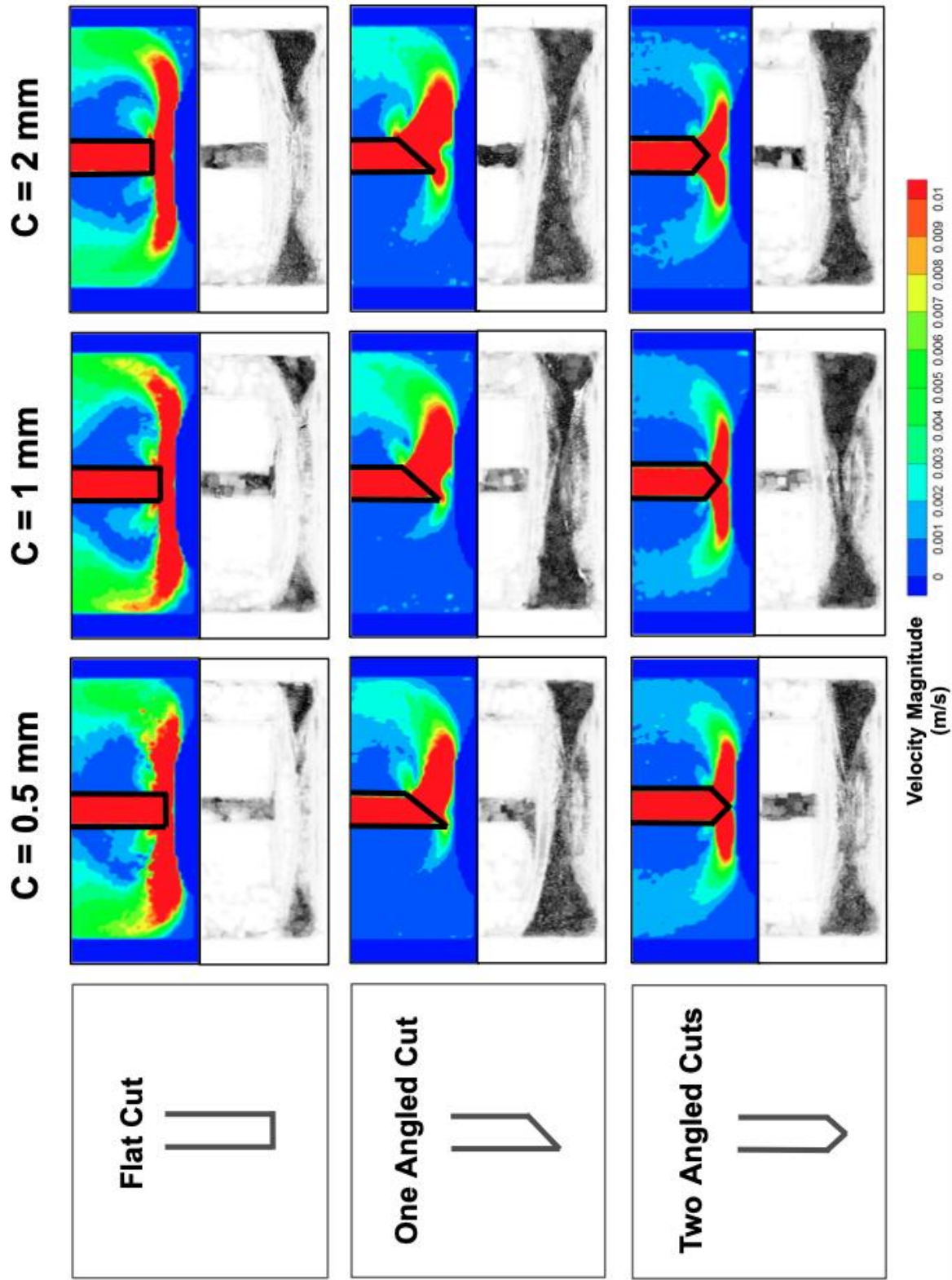


Figure 5.2 Velocity magnitude contour maps and the corresponding heel profiles for three different orifice shapes obtained by Method 1 and 3, respectively.

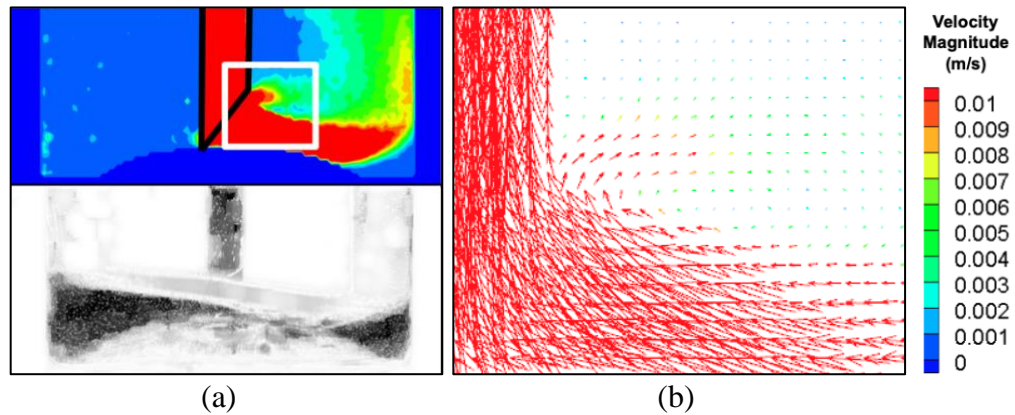


Figure 5.3 PIV output for one angled cut orifice at zero clearance ($C=0$ mm): (a) Velocity magnitude contour map and the corresponding heel profile obtained by *Method 1* and *3*, respectively; (b) velocity magnitude distribution map corresponding to a close look on the right half of the bottle obtained by *Method 1*. The velocity vectors in Panel (b) are in the region delimited by the white box in Panel (a).

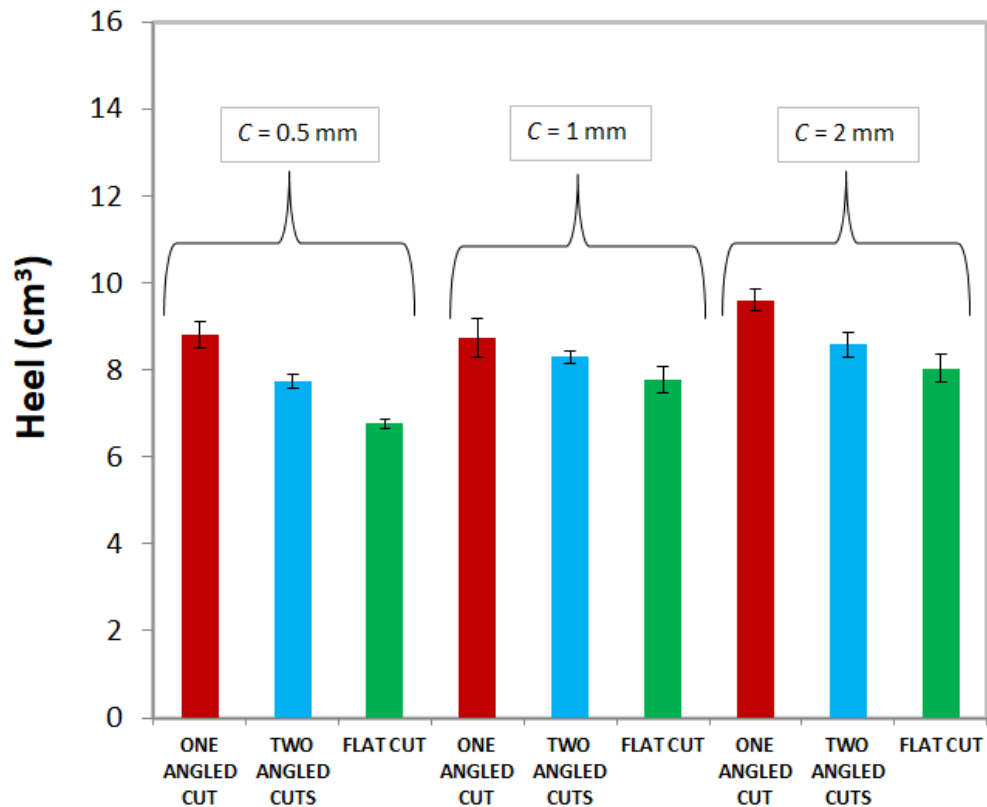


Figure 5.4 Comparison of heel obtained by *Method 4* at various clearances and orifice shapes. Error bars represent 95% confidence intervals, obtained by five repetitions of each experiment.

This, of course, is because of their slanted opening through which the fluid will penetrate even at $C=0$ mm, which is in line with the results shown in Figure 5.3.

In summary, despite the common use of angle cut orifices in consumer products, the results of this work clearly show that using flat cut dip tube orifices at low clearances not only minimizes the heel volume left in the dispensing bottle but also yields the highest volumetric flow rate during the discharge process. However, it should be clearly noted that the lowest threshold for the flat cut dip tube clearance would depend on geometric limitations such as 1) the deformation limit of the bottle as the consumer presses it (may result in contact between the orifice and the bottle bump, preventing the fluid penetration), and 2) fluid blockage at the orifice due to complex fluid rheology. Both these aspects require more experimental and computational studies.

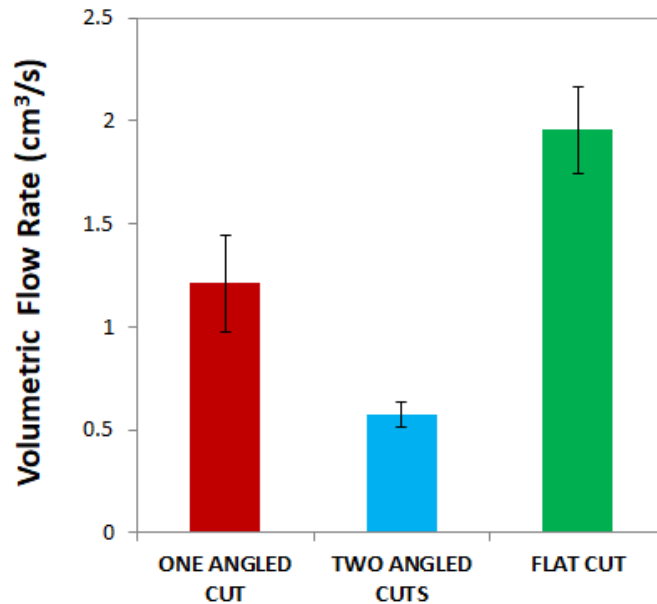


Figure 5.5 Comparison of volumetric flow rate at $C=0.5$ mm for all types of orifices studied in this work. Error bars represent 95% confidence intervals, obtained by four repetitions of each experiment.

5.5 Conclusions

In this work, we have shown that the dip tube orifice clearance and shape strongly affect the discharge hydrodynamics of complex, non-Newtonian fluids from dispensing bottles, and consequently the formation of the residual heel material. It was found that while lowering the clearance of the dip tube orifice decreases the residual heel volume, having an angled cut orifice at any clearance increases it compared to a flat cut orifice. Moreover, a flat cut orifice results in a higher volumetric flow rate for a given discharge pressure. Hence, flat-cut dip tube shapes at lower clearances should be preferred to minimize the heel volume and maximize the flow rate to fill the hand-pump housing of dispensing bottles quickly, resulting in the proper operation of the hand pump. Our expectation is that this work will help guide consumer packaging designers to design better-dispensing systems in which the discharge is improved and the heel volume is minimized.

CHAPTER 6

OVERALL CONCLUSIONS

In this work, the discharge process of rheologically complex fluids from dispensing “hand-pump” bottles was investigated. This topic, despite its industrial relevance, had not received sufficient attention, and the research in this field was only limited to discharge investigations of complex fluids through orifices of pipes and vessels. Hence, no research was present on more complicated systems such as dispensing bottles where the discharge takes place in the vertical direction. Such processes, described in Chapter 1 and investigated in other chapters in detail, typically result in the residual “heel”, which can be either determined or predicted by the methods and the correlations presented in this work.

To optically investigate the heel formation, the PIV technique was effectively used. The optical investigations of highly complex fluids, such as silica pastes that incorporate finely divided and dispersed silica particles, are quite problematic as one cannot probe the tracer particles due to the partial opacity of the fluid. However, as presented in Chapter 2, the optical transparency of the pastes can be optimized by using the refractive index matching method. This not only has important consequences for the industrial applicability of this approach to optimize future formulations but also allows academic investigations of fluids with pronounced non-Newtonian behavior such as yield-stress fluids.

In fact, as presented in Chapters 3 and 4, the PIV technique not only provided the velocity distributions in such fluids but also enabled visualizing the vertical cross-section of the heel profile of fluids with a wide range of rheology, including humectants, viscous polymer solutions, and pastes. This was only possible when optical obstacles such as the presence of air bubbles and reflective surfaces are almost completely eliminated by using

the proper equipment, and the pastes were formulated by taking into account the proper humectant concentration yielding the highest transparency. The results showed that one can use the PIV tool to visualize and quantify the heel in dispensing bottles (provided that they are transparent) by using the procedure described here.

It was also discovered that the CFD is an effective tool that can be used to predict the discharge hydrodynamics irrespective of the fluid rheology. Accordingly, it was found that transient CFD simulations based on the generalized Newtonian model (such as Carreau) predict the heel volume in the dispensing bottles with less than 10% error. In order to use such a model, first, one has to utilize the correct geometries to correctly measure the rheological parameters of the fluids. It was clearly stated in this work as well as in the literature that different shear ranges require the utilization of proper rheological geometries, i.e., vane-in-cup geometries are suitable for the low- and moderate- shear rates as it is a “non-disturbing” tool, while the narrow gap concentric (DIN) geometries are best suited for high- shear rates as it best represents the “pumping” conditions. Furthermore, to characterize the low-shear flow, creep tests with step-wise increasing stresses, whereas at high shear, shear rate sweep tests were used. The former best imitate the shear history of the fluid element during fluid discharge from the bottle, whereas the latter mimics its subsequent fast movement around and into the dip tube orifice. A Carreau equation was then fitted to all available experimental data, which yielded the Carreau parameters to be used in CFD simulations. The CFD results were validated using the PIV experiments, which agreed quite well even for highly viscous pastes. Upon the analysis of the results, it was found that the heel volume correlates well with the effective yield stress of the fluid, i.e., the stress at which viscosity starts to drop significantly.

Here it is worthwhile to outline the underlying assumptions and simplifications behind using the Carreau equation (or other similar generalized Newtonian constitutive equation with a low-shear viscosity limit) to describe thixotropic yield-stress fluids (e.g., pastes studied here). Recall that in this work, fast dispensing processes were considered (where the fluid is being discharged in not more than just a couple of minutes). During this time each element of the fluid experiences gradually increasing shear stress as it travels down the bottle wall toward the orifice of the dip tube. This is what the aforementioned creep tests imitate. Of course, a more accurate model could have been used to account for the thixotropic behavior of the fluid during such a flow (see, e.g., [75]) but that would have been an extremely computationally expensive approach, especially in frames of the multiphase model which is needed to describe the dispensing process. However, good agreement of this simplified approach with the experimental data when describing discharge from industrial tanks (see [40]) as well as in this work justifies this approach.

Furthermore, it was discovered that not only the fluid rheology but also operational and geometric parameters such as the suction pressure generated by the pump (ΔP), and tube-to-bottle diameter ratio (d/D) - both being best quantified in terms of volumetric flow rate - significantly affect the discharge hydrodynamics, and the heel volume. It was found that the resulting flow characteristics associated with these parameters *during* the discharge determine the heel volume *at the end* of the discharge. The flow during the discharge was quantified using the region of influence (ROI), which captures the relative size of the high-velocity region during the discharge, thus representing a *dynamic* state, whereas the heel after the discharge corresponds to a *static* state. Both aspects of the discharge are affected by the complex rheology of the fluid, and the flow rate (which is a function of the suction

pressure generated by the hand pump (ΔP), and the tube-to-bottle diameter ratio (d/D), while ROI and ΔV_H appear to correlate well irrespective of aforementioned effects. Hence, to minimize the heel in the dispensing bottles, the ROI has to be maximized by fine-tuning ΔP , d/D , and the rheological properties of the fluid.

Additionally, one can use the flow monitoring techniques to monitor the flow in any dispensing bottle, and optimize the pump and the bottle geometry (e.g., curvatures, diameter ratio) based on the magnitude of the ROI, which will enable the flow to effectively sweep the bottle, and minimize the heel. Alternatively, and perhaps more practically, steady-state CFD simulations based on the Carreau model quickly predict the hydrodynamics and the ROI, as shown in Chapter 4. Accordingly, provided that the Carreau parameters of the fluid are known, one can use steady-state CFD simulations to obtain the ROI, and modify the shape of the bottle to minimize the heel. This would not only save time for product developers and packaging engineers but also help visualize the flow inside the dispensing system that they are interested in, along with many useful information such as axial and radial velocity distributions, local shear stresses, pressure distributions, and many others.

However, it should be clearly reiterated that while the steady-state CFD approach worked quite well for most of the complex fluids studied here, it only fairly worked as the disperse phase in the fluids decreased. In order to accurately predict the hydrodynamics in such fluids, more comprehensive models including extensional and other viscoelastic forces will be needed.

Finally, it was found that the dip tube orifice clearance and shape strongly affect the discharge behavior, which, in turn, impacts the heel profile and volume. While

lowering the dip tube off-bottom clearance decreases the amount of heel, having an angled cut orifice irrespective of clearance increases it compared to a flat cut orifice. Moreover, for the majority of the hand-pump operations including complex fluids, the hand-pump recovery rate is highly important as slow recoveries would prevent the hand-pump housing to be filled with the liquid quickly, which would affect the pumping performance. In this work, we found that a flat cut orifice results in a higher volumetric flow rate for a given discharge pressure. This was somewhat surprising, given the fact that the majority of the commercially available dispensing bottles have an angled cut dip tube orifice. As shown in this work, flat-cut dip tube shapes at lower clearances should be preferred to minimize the heel volume and maximize the flow rate to fill the hand-pump housing of dispensing bottles quickly, resulting in the proper operation of the hand pump.

Overall, it is expected that the results obtained in this work will help guide researchers, product designers, and packaging engineers in designing optimized dispensing bottles for many applications, with an improved discharge and minimized amount of heel.

REFERENCES

- [1] P.E. Arratia, Complex fluids at work, *Physics*, 4 (2011) 9.
- [2] Y. Ma, S. Wu, J. Tong, X. Zhang, J. Peng, X. Liu, Rheological properties of corn starch dispersions in pregelatinized starch solution, in: *IEEE International Conference on Manipulation, Manufacturing and Measurement on the Nanoscale (3M-NANO)*, 2018, pp. 146-150.
- [3] S.E. Taylor, Rheology and structure of cornstarch suspensions in water-poly(propylene glycol) mixtures, *Journal of Dispersion Science and Technology*, 34 (2013) 887-897.
- [4] H.A. Barnes, J.F. Hutton, K. Walters, *An Introduction to Rheology*, 3rd ed., Elsevier, Amsterdam, Netherlands, 1989.
- [5] R.G. Larson, *The Structure and Rheology of Complex Fluids*, Oxford University Press, Oxford, NY, 1999.
- [6] C. Liu, Interfacial dynamics in complex fluids, *Journal of Fluid Science and Technology*, 11 (2016) JFST0021.
- [7] M. Pader, Dental Products, in: *Cosmetics and Toiletries Industry*, Springer science+business media, New York, 1992, pp. 210-257.
- [8] B. Teoman, A. Potanin, P.M. Armenante, Optimization of optical transparency of personal care products using the refractive index matching method, *Colloids and Surfaces A: Physicochemical and Engineering Aspects*, 610 (2021) 125595.
- [9] A. Ahuja, A. Potanin, Rheological and sensory properties of toothpastes, *Rheologica Acta*, 57 (2018) 459-471.
- [10] P. Coussot, Yield stress fluid flows: A review of experimental data, *Journal of Non-Newtonian Fluid Mechanics*, 211 (2014) 31-49.
- [11] F.W. Medaugh, G.D. Johnson, Investigation of the discharge and coefficients of small circular orifices, *Civil Engineering*, 10 (1940) 422-424.
- [12] J. Lienhard, Velocity coefficients for free jets from sharp-edged orifices, *Journal of Fluids Engineering*, 106 (1984) 13-17.
- [13] A. Hicks, W. Slaton, Determining the coefficient of discharge for a draining container, *The Physics Teacher*, 52 (2014) 43-47.
- [14] F.C. Lea, *Hydraulics*, 6th ed., Longmans, Green & Co, New York, NY, 1942.

- [15] D.D. Joye, B.C. Barrett, The tank drainage problem revisited: Do these equations actually work?, *The Canadian Journal of Chemical Engineering*, 81 (2003) 1052-1057.
- [16] T. Kiljanski, Discharge coefficient for free jets from orifices at low Reynolds number, *Journal of Fluids Engineering*, 115 (1993) 778-781.
- [17] M. Dziubinski, A. Marcinkowski, Discharge of Newtonian and non-Newtonian liquids from tanks, *Chemical Engineering Research and Design*, 84 (2006) 1194-1198.
- [18] W.F. Salas-Valerio, J.F. Steffe, Orifice discharge coefficients for power-law fluids, *Journal of Food Process Engineering* 12 (1990) 89-98.
- [19] B.M. Ntamba, Non-Newtonian pressure loss and discharge coefficients for short square-edged orifices plates, in, Cape Peninsula University of Technology, Cape Town, South Africa, 2011.
- [20] H. Judd, R.S. King, Some experiments on the frictionless orifice, *Engineering News*, 57 (1908) 326.
- [21] G.L. Tuve, R.E. Sprenkle, Orifice discharge coefficients for viscous liquids, *Instruments*, 6 (1933) 201-206.
- [22] J. Kayser, R.L. Shambaugh, Discharge coefficients for compressible flow through small-diameter orifices and convergent nozzles, *Chemical Engineering Science*, 46 (1991) 1697-1711.
- [23] F.C. Lea, *Hydraulics for Engineers and Engineering Students*, 6th ed., Edward Arnold & Co, London, UK., 1938.
- [24] A. Ostadfar, Chapter 1 - Fluid Mechanics and Biofluids Principles, in: A. Ostadfar (Ed.) *Biofluid Mechanics*, Academic Press, 2016, pp. 1-60.
- [25] A. Ahuja, G. Luisi, A. Potanin, Rheological measurements for prediction of pumping and squeezing pressures of toothpaste, *Journal of Non-Newtonian Fluid Mechanics*, 258 (2018) 1-9.
- [26] M. Dziubinski, A. Marcinkowski, Comments on Reynolds number definition for the discharge of non-Newtonian liquids from tanks, *Journal of Fluids Engineering*, 127 (2005) 1043-1046.
- [27] M. Dziubinski, A. Marcinkowski, The discharge of non-Newtonian liquids from tanks, in: 4th European Congress of Chemical Engineering, Grenada, 2003.

- [28] M. Khahledi, R. Haldenwang, R. Chhabra, Flow rate measurement of non-Newtonian fluids through sharp crested notches, *Journal of Hydraulic Engineering*, 141 (2014) 1-9.
- [29] M. Khahledi, R. Haldenwang, R. Chhabra, V. Fester, Non-Newtonian fluid flow from bottom of tank using orifices of different shapes, *Chemical Engineering Research and Design*, 157 (2020) 34-45.
- [30] T. Toplak, H. Tabuteau, J.R. de Bruyn, P. Coussot, Gravity draining of a yield-stress fluid through an orifice, *Chemical Engineering Science*, 62 (2007) 6908-6913.
- [31] Rituraj, A. Vacca, Modelling the flow of non-Newtonian fluids through sharp orifices, *Journal of Fluids Engineering, American Society of Mechanical Engineers (ASME)* 140 (2018) 1-6.
- [32] A.K. Samanta, T.K. Banerjee, S.K. Das, Pressure losses in orifices for the flow of gas-non-newtonian liquids, *The Canadian Journal of Chemical Engineering*, 77 (1999) 579-583.
- [33] L.K. Bohra, Flow and pressure drop of highly viscous fluids in small aperture orifices, in, Georgia Institute of Technology, Master's Thesis, 2004.
- [34] B.M. Ntamba, V. Fester, Pressure losses and limiting reynolds numbers for non-Newtonian fluids in short square-edged orifice plates, *Journal of Fluids Engineering*, 134 (2012) 091204.
- [35] M.R. Chowdhury, V.G. Fester, Modeling pressure losses for Newtonian and non-Newtonian laminar and turbulent flow in long square edged orifices, *Chemical Engineering Research and Design*, 90 (2012) 863-869.
- [36] R. Pal, Flow of oil-in-water emulsions through orifice and venturi meters, *Industrial & Engineering Chemistry Research*, 32 (1993) 1212-1217.
- [37] B. Teoman, G. Marron, A. Potanin, Rheological characterization of flow inception of thixotropic yield stress fluids using vane and T-bar geometries, *Rheologica Acta*, 60 (2021) 531-542.
- [38] K. Almdal, J. Dyre, S. Hvidt, O. Kramer, Towards a phenomenological definition of the term 'gel', *Polymer Gels and Networks*, 1 (1993) 5-17.
- [39] L. Kang, S. Majd, *Gels Handbook*, World Scientific, Hackensack, New Jersey, 2016.
- [40] A. Potanin, N.C. Shapley, Heel estimate during pressure-driven drainage of gels from tanks, *Chemical Engineering Science*, 230 (2021) 116158.

- [41] J. Yang, R.K. Bhagat, R.R. Fernandes, M. Nordkvist, K.V. Gernaey, U. Krühne, D.I. Wilson, Cleaning of toothpaste from vessel walls by impinging liquid jets and their falling films: Quantitative modelling of soaking effects, *Chemical Engineering Science*, 208 (2019) 115148.
- [42] V. Fester, B. Mbiya, P. Slatter, Energy losses of non-Newtonian fluids in sudden pipe contractions, *Chemical Engineering Journal*, 145 (2008) 57-63.
- [43] D.A. McNeil, J. Addlesee, A. Stuart, An experimental study of viscous flows in contractions, *Journal of Loss Prevention in the Process Industries*, 12 (1999) 249-258.
- [44] O. Novak, V. Koza, Measuring a discharge coefficient of an orifice for an unsteady compressible flow, *Paliva*, 5 (2013) 21-25.
- [45] F. Wang, T. Fang, Liquid jet breakup for non-circular orifices under low pressures, *International Journal of Multiphase Flow*, 72 (2015) 248-262.
- [46] D. Prohaska, Investigation of the discharge coefficient for circular orifices in riser pipes, in, *Clemson University*, 2008.
- [47] K. Swamee, N. Swamee, Discharge equation of a circular sharp-crested orifice, *Journal of Hydraulic Research*, 48 (2010) 106-107.
- [48] D. Della Valle, P.A. Tanguy, P.J. Carreau, Characterization of the extensional properties of complex fluids using an orifice flowmeter, *Journal of Non-Newtonian Fluid Mechanics*, 94 (2000) 1-13.
- [49] A. Elsaey, A. Abou El-Azm Aly, M. Fouad, CFD simulation of fractal-shaped orifices for flow measurement improvement, *Flow Measurement and Instrumentation*, 36 (2014) 14-23.
- [50] G.D. Eisenbrand, J.D. Goddard, Birefringence and pressure drop for the orifice flow of a polymer solution, *Journal of Non-Newtonian Fluid Mechanics*, 11 (1982) 37-52.
- [51] K. Madlener, B. Frey, H.K. Ciezki, Generalized Reynolds number for non-Newtonian fluids, *Progress in Propulsion Physics*, 1 (2009) 237-250.
- [52] D. Crespi-Llorens, P. Vicente, A. Viedma, Generalized Reynolds number and viscosity definitions for non-Newtonian fluid flow in ducts of non-uniform cross-section, *Experimental Thermal and Fluid Science*, 64 (2015) 125-133.
- [53] P. Slatter, Pipe flow of highly concentrated sludge, *Journal of Environmental Science and Health Part A*, 43 (2008) 1516-1520.

- [54] B. Dlugogorski, T. Schaefer, E. Kennedy, Pressure-loss correlations for designing foam proportioning systems, *Fire Technology*, 43 (2007) 123-144.
- [55] M. Mooney, Explicit formulas for slip and fluidity, *Journal of Rheology*, 2 (1931) 210-222.
- [56] A.B. Metzner, J.C. Reed, Flow of non-Newtonian fluids-correlation of the laminar, transition, and turbulent-flow regions, *American Institute of Chemical Engineers (AIChE) Journal*, 1 (1955) 434-440.
- [57] J.O. Wilkes, *Fluid Mechanics for Chemical Engineers*, Prentice-Hall, Upper Saddle River, New Jersey, 1999.
- [58] J.N. Israelachvili, Y. Chen, H. Yoshizawa, Relationship between adhesion and friction forces, *Journal of Adhesion Science and Technology*, 8 (1994) 1231-1249.
- [59] M. Khahledi, H. Rainer, V. Fester, R. Chhabra, Non-Newtonian fluids discharge through circular and square orifices from a tank, in: *Transport and Sedimentation of Solid Particles*, Cape Town, South Africa, 2019.
- [60] V.B. Randive, V.K. Gadkari, Non-stringy toothpaste, US Patent, US6162418 (2000).
- [61] J.P. Rothstein, G.H. McKinley, The axisymmetric contraction-expansion: the role of extensional rheology on vortex growth dynamics and the enhanced pressure drop, *Journal of Non-Newtonian Fluid Mechanics*, 98 (2001) 33-63.
- [62] T. Sridhar, An overview of the project M1, *Journal of Non-Newtonian Fluid Mechanics*, 35 (1990) 85-92.
- [63] B. Crawford, J.K. Watterson, P.L. Spedding, S. Raghunathan, W. Herron, M. Proctor, Wall slippage with siloxane gum and silicon rubbers, *Journal of Non-Newtonian Fluid Mechanics*, 129 (2005) 38-45.
- [64] H.J. Walls, S.B. Caines, A.M. Sanchez, S.A. Khan, Yield stress and wall slip phenomena in colloidal silica gels, *Journal of Rheology*, 47 (2003) 847-868.
- [65] R.P. Chhabra, J.F. Richardson, *Non-Newtonian Fluids in the Process Industries: Fundamentals and Engineering Applications*, Butterworth-Heinemann, Oxford, UK, 1999.
- [66] P.T. Slatter, The effect of the yield stress on the laminar/turbulent transition, in: *9th International Conference on Transport and Sedimentation of Solid Particles*, Cracow, Poland, 1997, pp. 547-561.

- [67] C.W. Macosko, *Rheology Concepts, Principles and Applications*, Wiley-VCH, New York, New York, 1992.
- [68] H.A. Barnes, K. Walters, The yield stress myth?, *Rheologica Acta*, 24 (1985) 323-326.
- [69] H.A. Barnes, The yield stress—a review or ‘παντα ρει’—everything flows?, *Journal of Non-Newtonian Fluid Mechanics*, 81 (1999) 133-178.
- [70] P.V. Liddell, D.V. Boger, Yield stress measurements with the vane, *Journal of Non-Newtonian Fluid Mechanics*, 63 (1996) 235-261.
- [71] H.A. Barnes, J.O. Carnali, The vane-in-cup as a novel rheometer geometry for shear thinning and thixotropic materials, *Journal of Rheology*, 34 (1990) 841-866.
- [72] N.J. Alderman, G.H. Meeten, J.D. Sherwood, Vane rheometry of bentonite gels, *Journal of Non-Newtonian Fluid Mechanics*, 39 (1991) 291-310.
- [73] P. Estellé, C. Lanos, A. Perrot, S. Amziane, Processing the vane shear flow data from Couette analogy, *Applied Rheology*, 18 (2008) 34037.
- [74] G.H. Meeten, Comparison of squeeze flow and vane rheometry for yield stress and viscous fluids, *Rheologica Acta*, 49 (2009) 45.
- [75] A. Potanin, 3D simulations of the flow of thixotropic fluids, in large-gap Couette and vane-cup geometries, *Journal of Non-Newtonian Fluid Mechanics*, 165 (2010) 299-312.
- [76] H.A. Ardakani, E. Mitsoulis, S.G. Hatzikiriakos, Thixotropic flow of toothpaste through extrusion dies, *Journal of Non-Newtonian Fluid Mechanics*, 166 (2011) 1262-1271.
- [77] C.-S. Wu, Y.T. Kwak, Characterization of microgels by Brookfield viscometry with cylindrical, T-bar, and flags impeller spindles, *Journal of Applied Polymer Science*, 71 (1999) 67-74.
- [78] J. Evans, J. Beddow, Characterization of Particle Morphology and Rheological Behavior in Solder Paste, *IEEE Transactions on Components, Hybrids, and Manufacturing Technology*, 10 (1987) 224-231.
- [79] B.J.R. Mayes, Synthetic Hectorite - a new toothpaste binder, *International Journal of Cosmetic Science*, 1 (1979) 329-340.
- [80] H.A. Barnes, Thixotropy-a review, *Journal of Non-Newtonian Fluid Mechanics*, 70 (1997) 1-33.

- [81] D.L. Tokpavi, A. Magnin, P. Jay, Very slow flow of Bingham viscoplastic fluid around a circular cylinder, *Journal of Non-Newtonian Fluid Mechanics*, 154 (2008) 65-76.
- [82] R.B. Bird, R.C. Armstrong, O. Hassager, *Dynamics of polymeric liquids, Volume 1: Fluid mechanics*, 2nd ed., Wiley, New York, New York, 1987.
- [83] F.H. Post, T. van Walsum, *Fluid Flow Visualization*, in: *Focus on Scientific Visualization*, Dagstuhl, Germany, 1991.
- [84] C. Sirasitthichoke, S. Perivilli, M.R. Liddell, P.M. Armenante, Experimental determination of the velocity distribution in USP Apparatus 1 (basket apparatus) using Particle Image Velocimetry (PIV), *International Journal of Pharmaceutics*: X, 3 (2021) 100078.
- [85] F. Ricard, C. Brechtelsbauer, X.Y. Xu, C.J. Lawrence, Monitoring of multiphase pharmaceutical processes using electrical resistance tomography, *Chemical Engineering Research and Design*, 83 (2005) 794-805.
- [86] A. Kazemzadeh, F. Ein-Mozaffari, A. Lohi, Hydrodynamics of solid and liquid phases in a mixing tank containing high solid loading slurry of large particles via tomography and computational fluid dynamics, *Powder Technology*, 360 (2020) 635-648.
- [87] R.M. West, X. Jia, R.A. Williams, Quantification of solid-liquid mixing using electrical resistance and positron emission tomography, *Chemical Engineering Communications*, 175 (1999) 71-97.
- [88] S. Kim, A.N. Nkaya, T. Dyakowski, Measurement of mixing of two miscible liquids in a stirred vessel with electrical resistance tomography, *International Communications in Heat and Mass Transfer*, 33 (2006) 1088-1095.
- [89] L. Pakzad, F. Ein-Mozaffari, P. Chan, Measuring mixing time in the agitation of non-Newtonian fluids through electrical resistance tomography, *Chemical Engineering Technology*, 31 (2008a) 1838-1845.
- [90] L. Pakzad, F. Ein-Mozaffari, S.R. Upreti, A. Lohi, Characterization of the mixing of non-newtonian fluids with a scaba 6SRGT impeller through ERT and CFD, *The Canadian Journal of Chemical Engineering*, 91 (2012) 90-100.
- [91] A. Bawadi, C. Dave, T. Nguyen, C. Cooper, A.A. Adesina, Electrical resistance tomography-assisted analysis of dispersed phase hold-up in a gas-inducing mechanically stirred vessel, *Chemical Engineering Science*, 66 (2011) 5648-5662.

- [92] T.L. Rodgers, L. Gangolf, C. Vannier, M. Parriaud, M. Cooke, Mixing times for process vessels with aspect ratios greater than one, *Chemical Engineering Science*, 66 (2011 a) 2935-2944.
- [93] P. Tahvildarian, H. Ng, M. D'Amato, S. Drappel, F. Ein-Mozaffari, S.R. Upreti, Using electrical resistance tomography images to characterize the mixing of micron-sized polymeric particles in a slurry reactor, *Chemical Engineering Journal*, 172 (2011) 517-525.
- [94] B. Teoman, C. Sirasitthichoke, A. Potanin, P.M. Armenante, Determination of the just-suspended speed, N_{js} , in stirred tanks using electrical resistance tomography (ERT), *American Institute of Chemical Engineers (AIChE) Journal*, (2021) e17354.
- [95] B. Teoman, Z.P. Muneeswaran, G. Verma, D. Chen, T.V. Brinzari, A. Almeda-Ahmadi, J. Norambuena, S. Xu, S. Ma, J.M. Boyd, P.M. Armenante, A. Potanin, L. Pan, T. Asefa, V. Dubovoy, Cetylpyridinium Trichlorostannate: Synthesis, antimicrobial properties, and controlled-release properties via electrical resistance tomography, *American Chemical Society (ACS) Omega*, 6 (2021) 35433-35441.
- [96] R. Hou, P.J. Martin, H.J. Uppal, A.J. Kowalski, An investigation on using electrical resistance tomography (ERT) to monitor the removal of a non-Newtonian soil by water from a cleaning-in-place (CIP) circuit containing different pipe geometries, *Chemical Engineering Research and Design*, 111 (2016) 332-341.
- [97] S.J. Stanley, R. Mann, K. Primrose, Interrogation of a precipitation reaction by electrical resistance tomography (ERT), *American Institute of Chemical Engineers (AIChE) Journal*, 51 (2005b) 607-614.
- [98] C. Tan, F. Dong, M. Wu, Identification of gas/liquid two-phase flow regime through ERT-based measurement and feature extraction, *Flow Measurement and Instrumentation*, 18 (2007) 255-261.
- [99] M.S. Takriff, A. Ahmad, M.I. Rosli, S. Jantan, ERT visualization of gas dispersion performance of aerofoil and radial impellers in an agitated vessel, *Jurnal Teknologi*, 64 (2013) 75-78.
- [100] R. Mann, ERT imaging and linkage to CFD for stirred vessels in the chemical process industry, in, Hong Kong, 2009.
- [101] M. Sharifi, Young, B, Electrical resistance tomography (ERT) applications to chemical engineering, *Chemical Engineering Research and Design*, 91 (2013) 1625-1645.

- [102] I. Edwards, S.A. Axon, M. Barigou, E.H. Stitt, Combined use of PEPT and ERT in the study of aluminum hydroxide precipitation, *Industrial Engineering and Chemistry Research*, 48 (2009) 1019-1028.
- [103] A. Parvareh, M. Rahimi, A. Alizadehdakhel, A.A. Alsairafi, CFD and ERT investigations on two-phase flow regimes in vertical and horizontal tubes, *International Communications in Heat and Mass Transfer*, 37 (2010) 304-311.
- [104] S.A. Razzak, S. Barghi, J.X. Zhu, Application of electrical resistance tomography on liquid–solid two-phase flow characterization in an LSCFB riser, *Chemical Engineering Science*, 64 (2009) 2851-2858.
- [105] F. Dong, Y.B. Xu, L.J. Xu, L. Hua, X.T. Qiao, Application of dual-plane ERT system and cross-correlation technique to measure gas–liquid flows in vertical upward pipe, *Flow Measurement and Instrumentation*, 16 (2005) 191-197.
- [106] Z. Meng, Z. Huang, B. Wang, H. Ji, H. Li, Y. Yan, Air-water two-phase flow measurement using a Venturi meter and an electrical resistance tomography sensor, *Flow Measurement and Instrumentation*, 21 (2010) 268-276.
- [107] D. Wadnerkar, M.O. Tade, V.K. Pareek, R.P. Utikar, CFD simulation of solid–liquid stirred tanks for low to dense solid loading systems, *Particuology*, 29 (2016) 16-33.
- [108] L. Oshinowo, A. Bakker, CFD modeling of solids suspensions in stirred tanks, in: *Symposium on Computational Modeling of Metals, Minerals and Materials (TMS Annual Meeting)*, Seattle, Washington, 2002.
- [109] C. Sirasitthichoke, B. Teoman, J. Thomas, P.M. Armenante, Computational prediction of the just-suspended speed, N_{js} , in stirred vessels using the lattice Boltzmann method (LBM) coupled with a novel mathematical approach, *Chemical Engineering Science*, (2022) 117411.
- [110] N.C.S. Kee, R.B.H. Tan, CFD Simulation of Solids Suspension in Mixing Vessels, *The Canadian Journal of Chemical Engineering*, 80 (2002) 1-6.
- [111] A. Tamburini, G. Gagliano, F. Scargiali, G. Micale, A. Brucato, M. Ciofalo, CFD Simulation of Radially Stirred Baffled and Unbaffled Stirred Tanks, *Chemical Engineering Transactions*, 74 (2019) 1033-1038.
- [112] A. Tamburini, A. Brucato, A. Cipollina, G. Micale, M. Ciofalo, CFD predictions of sufficient suspension conditions in solid-liquid agitated tanks, *International Journal of Nonlinear Sciences and Numerical Simulation*, 13 (2012) 427-443.

- [113] L.W. Adams, M. Barigou, CFD analysis of caverns and pseudo-caverns developed during mixing of non-Newtonian fluids *Chemical Engineering Research and Design*, 85 (2007) 598-604.
- [114] N. Arun, M. Sankarasubramanian, M. Kaushik, CFD analysis on discharge coefficient during Non-Newtonian flows through orifice meter, *International Journal of Engineering Science and Technology*, 2 (2010).
- [115] V. Mamaeva, C.M. Sahlgren, M. Linden, Mesoporous silica nanoparticles in medicine-recent advances, *Advanced Drug Delivery Reviews*, 65 (2013) 689-702.
- [116] Y. Ahn, J.-Y. Yoon, C.-W. Baek, Y.-K. Kim, Chemical mechanical polishing by colloidal silica-based slurry for micro-scratch reduction, *Wear*, 257 (2004) 785-789.
- [117] I. Niskanen, M. Härkönen, K. Hibino, T. Suoranta, A. Popov, Refractive index retrieval from transmittance measurements, *Optik - International Journal for Light and Electron Optics*, 127 (2016) 5562-5567.
- [118] G.J. Ojeda-Mendoza, H. Contreras-Tello, L.F. Rojas-Ochoa, Refractive index matching of large polydisperse silica spheres in aqueous suspensions, *Colloids and Surfaces A*, 538 (2018) 320-326.
- [119] S. Wiederseiner, N. Andreini, G. Epely-Chauvin, C. Ancey, Refractive-index and density matching in concentrated particle suspensions: a review, *Exp Fluids*, 50 (2016) 1183-1206.
- [120] R. Budwig, Refractive index matching methods for liquid flow investigations, *Experiments in Fluids*, 17 (1994) 350-355.
- [121] C.J. Koh, P. Hookham, L.G. Leal, An experimental investigation of concentrated suspension flows in a rectangular channel, *Journal of Fluid Mechanics*, 266 (1994) 1-32.
- [122] A.P. Philipse, C. Smits, A. Vrij, A light scattering contrast variation study on nonaqueous suspensions of coated silica spheres, *Journal of Colloid and Interface Science*, 129 (1989) 335-352.
- [123] R.C. Chen, L.S. Fan, Particle image velocimetry for characterizing the flow structure in three-dimensional gas-liquid-solid fluidized beds, *Chemical Engineering Science*, 47 (1992) 3615-3622.
- [124] Y.A. Hassan, E.E. Dominguez-Ontiveros, Flow visualization in a pebble bed reactor experiment using PIV and refractive index matching techniques, *Nuclear Engineering and Design*, 238 (2008) 3080-3085.

- [125] G.J. Daviero, P.J.W. Roberts, K. Maile, Refractive index matching in large-scale stratified experiments, *Experiments in Fluids*, 31 (2001) 119-126.
- [126] A. Zachos, M. Kaiser, W. Merzkirch, PIV measurements in multiphase flow with nominally high concentration of the solid phase, *Experiments in Fluids*, 20 (1996) 229-231.
- [127] Ó. Sampedro, J.R. Salgueiro, Turbidimeter and RGB sensor for remote measurements in an aquatic medium, *Measurement Science and Technology*, 68 (2015) 128-134.
- [128] A. Bin Omar, M. Bin MatJafri, Turbidimeter Design and Analysis: A Review on Optical Fiber Sensors for the Measurement of Water Turbidity, *Sensors*, 9 (2009).
- [129] C. Celia, E. Trapasso, D. Cosco, D. Paolino, M. Fresta, Turbiscan lab expert analysis of the stability of ethosomes and ultradeformable liposomes containing a bilayer fluidizing agent, *Colloids Surf B Biointerfaces*, 72 (2009) 155-160.
- [130] C. Lemarchand, P. Couvreur, C. Vauthier, D. Costantini, R. Gref, Study of emulsion stabilization by graft copolymers using the optical analyzer Turbiscan, *Int J Pharm*, 254 (2003) 77-82.
- [131] A. Potanin, Rheology of silica dispersions stabilized by polymers, *Colloids and Surfaces A: Physicochemical and Engineering Aspects*, 562 (2019) 54-60.
- [132] B. Teoman, A. Potanin, P.M. Armenante, The discharge of complex fluids through an orifice: A review, *Chemical Engineering Research and Design*, 179 (2022) 346-364.
- [133] N.Q. Dzuy, D.V. Boger, Yield stress measurement for concentrated suspensions, *Journal of Rheology*, 27 (1983) 321-349.
- [134] P. Estellé, C. Lanos, High torque vane rheometer for concrete: principle and validation from rheological measurements, *Applied Rheology*, 22 (2012) 12881.
- [135] B. Piqueras-Fiszman, C. Spence, The weight of the bottle as a possible extrinsic cue with which to estimate the price (and quality) of the wine? Observed correlations, *Food Quality and Preference*, 25 (2012) 41-45.
- [136] P.C.F. Møller, A. Fall, D. Bonn, Origin of apparent viscosity in yield stress fluids below yielding, *EPL (Europhysics Letters)*, 87 (2009) 38004.
- [137] F.R. Menter, Two-equation eddy-viscosity turbulence models for engineering applications, *AIAA journal*, 32 (1994) 1598-1605.

- [138] B. Teoman, S. Shastry, S. Abdelhamid, P.M. Armenante, Imaging method for the determination of the minimum agitation speed, N_{js} , for solids suspension in stirred vessels and reactors, *Chemical Engineering Science*, 231 (2021) 116263.
- [139] S. Sternberg, Biomedical image processing, *Computer*, 16 (1983) 22-34.
- [140] M. Slaker, J. Harkness, B. Sorg, A standardized and automated method of perineuronal net analysis using *Wisteria floribunda* agglutinin staining intensity, *IBRO Reports*, 1 (2016).
- [141] D. Bonn, M.M. Denn, L. Berthier, T. Divoux, S. Manneville, Yield stress materials in soft condensed matter, *Reviews of Modern Physics*, 89 (2017) 035005.
- [142] M. Zlokarnik, *Stirring*, Wiley-VCH, Somerset, New Jersey, 2001.
- [143] M.J.H. Simmons, I. Edwards, J.F. Hall, X. Fan, D.J. Parker, E.H. Stitt, Techniques for visualization of cavern boundaries in opaque industrial mixing systems, *American Institute of Chemical Engineers (AIChE) Journal*, 55 (2009) 2765-2772.
- [144] L. Pakzad, F. Ein-Mozaffari, P. Chan, Using electrical resistance tomography and computational fluid dynamics modeling to study the formation of cavern in the mixing of pseudoplastic fluids possessing yield stress, *Chemical Engineering Science*, 63 (2008b) 2508-2522.
- [145] A. Amanullah, S.A. Hjorth, A.W. Nienow, Cavern sizes generated in highly shear thinning viscous fluids by SCABA 3SHP1 impellers, *Food and Bioproducts Processing*, 75 (1997) 232-238.
- [146] J. Solomon, T.P. Elson, A.W. Nienow, G.W. Pace, Cavern sizes in agitated fluids with a yield stress, *Chemical Engineering Communications*, 11 (1981) 143-164.
- [147] T.P. Elson, The growth of caverns formed around rotating impellers during the mixing of a yield stress fluid, *Chemical Engineering Communications*, 96 (1990) 303-319.
- [148] J.S. Ayala, H.L. de Moura, R.d.L. Amaral, F.d.A. Oliveira Júnior, J.R. Nunhez, G.J. de Castilho, Two-dimensional shear rate field and flow structures of a pseudoplastic fluid in a stirred tank using particle image velocimetry, *Chemical Engineering Science*, 248 (2022) 117198.
- [149] F.H. Post, T. van Walsum, *Fluid Flow Visualization*, in: H. Hagen, Müller, H., Nielson, G.M. (Ed.) *Focus on Scientific Visualization. Computer Graphics: Systems and Applications*, Springer, Berlin, Heidelberg, 1993, pp. 1-40.

- [150] B. Teoman, A. Potanin, P.M. Armenante, Residual heel volume during the pressure-driven discharge of complex fluids from consumer dispensing bottles, *Journal of Non-Newtonian Fluid Mechanics*, 309 (2022) 104917.
- [151] N. Arun, M. Sankarasubramanian, M. Kaushik, CFD analysis on discharge coefficient during Non-Newtonian flows through orifice meter, *International Journal of Engineering Science and Technology*, 2 (2010) 3151-3164.
- [152] C. Sirasitthichoke, S. Patel, K.G. Reuter, A. Hermans, G. Bredael, P.M. Armenante, Influence of basket mesh size on the hydrodynamics in the USP rotating basket dissolution testing Apparatus 1, *International Journal of Pharmaceutics*, 607 (2021) 120976.